Elucidation of Mechanism and Energetics of Wetting of Model Surfaces and Characterization of Structural and Dynamical Properties of Biologically Inspired Systems by Molecular Simulations

Thesis Submitted to AcSIR for the Award of the Degree of DOCTOR OF PHILOSOPHY In Chemical Sciences

By
Prithvi Raj Pandey
Registration Number: 10CC11J26041

Under the Guidance of
Dr. Sudip Roy

CSIR-National Chemical Laboratory,
Pune-411008, India.

DECLARATION

I, hereby declare that all the computational studies embodied in this thesis entitled, **Elucidation of Mechanism and Energetics of Wetting of Model Surfaces and Characterization of Structural and Dynamical Properties of Biologically Inspired Systems by Molecular Simulations** submitted for the degree of Doctor of Philosophy in Chemical Sciences, to the AcSIR-NCL have been carried out by me at the Physical and Materials Chemistry Division, CSIR-National Chemical Laboratory, Pune-411008, India, under the supervision of **Dr. Sudip Roy**. This work is original and has not been submitted in part or full by me, for any degree or diploma to this or to any other University.

Date: Prithvi Raj Pandey

Physical and Materials Chemistry Division,
CSIR-National Chemical Laboratory,
Pune-411008, India.

Dedicated to

my teachers and my parents

Acknowledgment

The research outlined in the thesis would not have been possible without the inspiration and motivation provided by people too numerous to mention. It is a pleasant moment now that I have the opportunity to express my gratitude to all of them.

First and foremost, I take the esteemed opportunity to acknowledge my thesis supervisor Dr. Sudip Roy for constantly supporting and motivating me throughout my Ph. D. I would like to thank him for giving me great freedom for this research, and also giving me opportunity to work on projects which are not part of this thesis. His advice on both research as well as on my career have been priceless.

I am also grateful to Dr. B. L. V. Prasad, CSIR-National Chemical Laboratory, Pune for his collaboration on a project described in this thesis.

I express my gratitude to Dr. Sayam Sen Gupta, CSIR-National Chemical Laboratory, Pune for insightful discussions.

I thank members of my doctoral advisory committee Dr. Amol Kulkarni, Dr. Nayana Vaval (CSIR-NCL, Pune), and Dr. Arnab Mukherjee (Indian Institute of Science Education and Research, Pune) for their constructive comments during the process of evaluation. It helped me develop approach towards presenting my research work.

I thank Dr. Rajnish Kumar (CSIR-NCL, Pune) for discussions. I thank Dr. Sarika Maitra Bhattacharyya for her classes on statistical mechanics.

I also thank Dr. Sourav Pal, Director, CSIR-NCL, Pune for facilities, and his

classes on quantum mechanics.

I am thankful to the colleagues of my working group for a nice working environment. I thank Mr. Chandan Kumar Choudhury for sharing his outstanding technical knowledge. I had the opportunity to work with Ms. Swagata Pahari, Mr. Sujit Sarkar, Mr. Santu Biswas, and Mr. Anil Mhashal. Working with them has been a learning experience for me. I thank Mr. Subhadip Das for his thoughts on several things. I thank Mr. Nilesh Choudhary, Mr. Bappa Ghosh, and Ms. Pragati Sharma for their encouragement. A special thanks to Mr. Souvik Chakraborty for many scientific and non-scientific discussions.

I have been blessed to be taught by many fine teachers during my formative years. I would like to specially mention Dr. Chandan Saha and Dr. Dilip Khamrui for teaching me to think. A special thanks to Dr. Abhijit Kar Gupta (*kaku*) and Ms. Madhuri Katti (*kakima*) for guiding me through hard times and motivating me to pursue research.

Besides this I would like to thank all my friends in NCL Golden Jubilee Hostel. I thank Sujit da, Debasis da, Pati da, Subhadeep da, Anupam da, Anal da, Partha da, Sumantra da, Garai da, Krishanu da, Shyam da, Chandan da, Tamas da, Saikat da, Arijit, Kanak, Chini, Manna, Aryya, Achintya, Anjan, Himadri, Prabhat, Santi, Santanu, Atanu, Hridesh, Suman, Anup for making my stay unforgettable. Among them Sujit da, Debasis da, Pati da and Subhadeep da are very special. Thanks to Ankush bhaiya, my roommate in hostel, for many things impossible to mention. Thanks to Aniruddha, Saikat, Ujjwal, Manoj, Abhik, Anirban for unforgettable memories.

I would like to thank my parents for their encouragement and support. Finally, a very special thanks to my wife Deblina for her unconditional encouragement over the years before and after our marriage. She has always given me confidence to take

up many challenges. I am thankful to Deblina for proof reading this thesis.

Contents

List of Figures

List of Tables

Abstract

In this thesis we have carried out research on model surfaces and biologically inspired systems using molecular dynamics (MD) simulations, which is a widely used method to understand the properties of systems at their structural level. The primary objective of the present thesis is to understand the mechanism and energetics of wetting of model surfaces, and structure and dynamics of biologically inspired systems in water.

To accommodate both model surfaces and biological systems, the thesis has been divided into two parts, first, model surfaces and interfaces and second, biologically inspired systems. In the first part (Part A), wetting and dewetting of model rough hydrophilic surfaces, and structure and dynamics of water near model atomistic protrusions are discussed. In the second part (Part B) of this thesis unwinding mechanism of α-helical homopolymeric peptides in water, mechanism of water insertion into phospholipid bilayer-water interface, and self-assembly of sophorolipids in water are discussed. The work on self-assembly of sophorolipids in water discussed in chapter 9 has been carried out in collaboration with Dr. B.L.V. Prasad at CSIR-National Chemical Laboratory, Pune. The experimental part was performed by Dr. Prasad's group, and we performed the simulations to understand the self-assembly of sophorolipids in water. The chapters are arranged starting from model systems we move closer to real systems. But all the systems investigated here, interface with

water and elucidation of properties related to water are common.

The thesis starts with an introduction to the systems under cosideration and review of literature (chapter 1). This is followed by computational methods (chapter 2) used to carry out the simulations discussed in this thesis. These chapters are common to both parts A and B. Separate introductions and computational details specific to the work are further discussed in all the chapters.

Part A starts with an introduction (chapter 3) to various factors guiding the wettability of surfaces. Among many factors surface-water non-bonded interactions and surface topology are fundamental to address. Effects of structuring of water in the confinements are also discussed. Also, choice and the construction of the model systems discussed in chapters 4 and 5 are also discussed.

Chapter 4 of part A is devoted to the wetting and dewetting of rough hydrophilic surfaces. Series of hydrophilic surfaces varying in roughness and Lennard-Jones interaction parameter with water are constructed and the mechanism and energetics of their wetting/dewetting are studied. The hydrophilicity of the surfaces are defined depending upon the surface-water Lennard-Jones interaction parameter. Correlation between energetics of wetting/dewetting and roughness has been established.

Chapter 5 in part A is focussed on structure and dynamics of water near model atomistic protrusions. The atomistic protrusions consist of hydrophobic and hydrophilic blocks. They are structurally motivated from lipid bilayer-water system. Hydrophilicity/hydrophobicity of the particles constituting the protrusions are defined with respect to their van der Waals interaction with water. Structure and dynamics of water near these atomistic protrusions are studied in a range of temperatures and pressures. Water molecules near the surface of hydrophilic blocks are observed to undergo higher ordering than the rest of the system.

Strarting from model systems in part A we have moved close to real systems in part B, and have studied the structure and dynamics of biologically inspired systems in water. Part B starts with an introduction (chapter 6) to the role of hydrophobicity/hydrophilicity in various biological systems. Introduction to model α-helical peptides (discussed in chapter 7) are provided. Also, structural distinctions of phospholipids and sophorolipids (discussed in chapters 8 and 9 respectively) are explored.

Chapter 7 of part B is devoted to the early stage unwinding mechanisms of zwitterionic, capped, and neutral forms of different model α-helical homopolymeric peptides in water. The different α-helical homopolymeric peptides studied differ in their side chain hydrophobicity and helix forming propensity. Structural changes in the different helices during unwinding and role of water in the unwinding are explored. Energetics due to intra-helix and helix-water interactions are also elucidated.

Chapter 8 of part B if focussed on the mechanism of water insertion into phospholipid bilayer. At the lipid bilayer-water interface, water penetrates upto the starting of hydrophobic region of the bilayer as shown in chapter 5 of part A for model atomistic protrusions constructed of hydrophobic and hydrophilic blocks. We have envisaged the mechanism of water insertion so deep into the lipid bilayer which is not rigid as the model system discussed in chapter 5, and have elucidated that penetration of water is mediated by hydrophilic head group of phospholipid. Correlated motion of the dihedrals at the head group mediate the water insertion.

Chapter 9 of part B deals with the self-assembly simulations of sophorolipid in water. Self-assembly simulations of oleic acid and linolenic acid sophorolipids are discussed. These molecules differ in the number of double bonds present in the hydrophobic tail. Structural characteristics of the self-assembled structures from the two sophorolipids are elucidated.

Chapter 1

Introduction

The field of soft matter, a subfield of condensed matter physics, comprises of rich variety of materials. Ranging from polymers to biological materials soft matters incorporate systems for which properties are sensitive to mechanical stress and thermal fluctuations. These materials are capable to self-organise in a wide variety of phases, and structures. Hence it is crucial to envisage the structural details of the different soft matter systems. Extent of hydrophobic and hydrophilic groups present in the chemical structure is capable to influence the self-organised structure in soft matter systems.

Correlation between atomistic chemical structure and molecular achitecture with bulk properties of the system is a major attraction for soft matter research [1]. Therefore, objective of the present thesis is to investigate and understand the structural level interactions of water with various systems with varying extent of hydrophobicity and hydrophilicity, and also the outcome of these interactions. Starting from model systems, research is carried out with systems which are close to real systems. To accommodate both model systems and real systems, the thesis is divided into two parts.

In part A, research on wetting and dewetting of model rough hydrophilic surfaces, and structure and dynamics of water near model atomistic protrusions are discussed. In part B, research on biologically inspired systems (model α-helical homopolymeric peptides, phospholipids, and sophorolipids) are elucidated. The different systems discussed in the present thesis vary in the extent of hydrophilicity/hydrophobicity, and interface with water is common to all the systems under consideration.

Water is ubiquitous in nature. Being the medium for all life on Earth, water is present in bulk as well as in confinements. The extent of complex behaviour exhibited by a seemingly simple molecule can be speculated from the fact, that research on water has gathered attention of scientists from many different backgrounds. Physicists, chemists, biologists, and engineers study different aspects of water's behaviour and its interaction with other materials. Various facets of water's properties and behaviour have been organized in a popular website [2]. Among many aspects of behaviour and properties of water, it is important to mention the facets covered in the present thesis: to elucidate the mechanism and energetics of interaction of water with model surfaces, and structural and dynamical properties of biologically inspired systems in water.

Hydrophobicity and hydrophilicity of a material is defined depending upon its interaction with water. A particle is called hydrophilic (water-loving) if its interactions with water are favourable, and hydrophobic (water-fearing) if unfavourable. Hydrophobicity and/or hydrophilicity is crucial in several phenomenon. In the macroscopic scale, contact angle measurement of water droplet on the surface gives reasonable quantification of hydrophobicity/hydrophilicity. But, in the microscopic scale structural details and environment needs to be taken into account. Wetting and dewetting of materials depend primarily upon hydrophobicity and hydrophilicity of the constituent particles [3]. Self-assembly in water is guided by the presence of hy-

drophobic and hydrophilic groups, and also on the amount of water present in the system [4]. It also depends upon the shape, size, and orientation of the chemical moieties undergoing self-assembly [4]. Lipids and sufactants self-assemble in water with their hydrophilic groups pointing towards water and hydrophobic groups clustered near each other. But in a hydrophobic solvent reverse happens, i.e., hydrophobic groups point towards the solvent [5]. Amino acids, building blocks of proteins, have also been classified depending upon the hydrophobicity/hydrophilicty of the group present in their side-chains. A hydrophobic amino acid (e.g. Leucine) contain hydrophobic group (isopropyl) in its side-chain. Side chain polarity is a critical factor in interaction of amino acids with water as it affects the three dimensional structure of proteins and their function. In organisms, proteins self-assemble into variety of functional structures pointing the hydrophobic groups away from water [6–8]. Water present in the grooves of certain proteins guide the function of the entire protein [9, 10].

Molecular dynamics (MD) simulation is a useful tool to predict and understand experimentally observable properties at the molecular level. It provides microscopic molecular level predictions with accuracy. MD simulations have been used to understand complex problems like protein folding, polymer dynamics, enzyme-substrate binding etc. at their structural details and mechanistic pathways. In last two decades computer hardware and simulation algorithms have improved significantly, which enable us with more accurate predictions. For exmple, in our group, MD simulations are routinely used to explain structure and dynamics of polyethylenimine in water and its interaction with phospholipid bilayer at different protonation states [11, 12]. Structural and bulk properties of polybenzimidazole doped with phosphoric acid have been predicted [13], and existance of dynamic heterogeneity in binary mixtures of

phosphoric acid and benzimidazole has been proved [14]. Structure, and thermodynamics carbon nanotube polycarbonate composites have been elucidated [15]. Also, morphology of carbon nanotube in polycarbonate composites have been investigated using dissipative particle dynamics [16]. Heat transfer calculations are performed for structure I methane hydrate decomposition [17].

In the present thesis, we have used MD simulations to uderstand the outcome of the interaction of water with model surfaces and biologically inspired systems. The primary focus of the present thesis is to understand the interaction of water with different systems with varying hydrophobicity and hydrophilicily, and to elucidate the outcome of these interactions. It is well known that nanostructuring on the surface enhances the hydrophobicity of a hydrophobic surface. Lotus effect is a classical example [18].In the present thesis, wetting behaviour of nanostructured hydrophilic surfaces is studied with the motivation to investigate its mechanism and energetics with varying roughness. Also, structure and dynamics of water molecules near model atomistic protrusions containing both hydrophilic and hydrophobic components are studied at different temperatures and pressures. The model atomistic protrusions are structurally motivated from lipid bilayer-water interface. This model system has been further extended to close to real systems, and phospholipid bilayer-water interface has been studied. Biologically inspired systems are studied with the motivation to understand the importance of hydrophobicity and hydrophilicity in different biological systems. Different class of systems with varying hydrophobic and hydrophilic moieties are taken up. Unwinding mechanisms of α-helical homopolymeric peptides are studied. The different amino acids to construct the homopolymeric peptides are chosen such that they differ in degree of side chain hydrophobicity. Phospholipid bilayer water interface is studied to elucidate the mechanism of water insertion into the

lipid bilayer. Also, self-assembly of sophorolipids in water is studied. Phospholipids and sophorolipids differ in the degree of hydrophobicity and hydrophilicity present in their chemical structure.

The layout of the thesis is as follows. In part A interaction of water with model surfaces and interfaces is presented. Chapters 3 and 4 are discussed under part A. In part B interaction of biologically inspired systems with water are studied. Chapters 5, 6, and 7 are discussed under part B.

In chapter 2, computational procedures are discussed in brief.

In chapter 4, wetting and dewetting behaviour of model rough hydrophilic surfaces is discussed.

In chapter 5, structure and dynamics of water near model atomistic protrusions containing both hydrophobic and hydrophilic components is discussed.

In chapter 7, unwinding mechanism of different α-helical homopolymeric peptides is discussed.

In chapter 8, mechanism of water insertion into DPPC bilayer is discussed.

In chapter 9, self-assembly of sophorolipids in water is discussed.

In chapter 10, conclusions from above studies are discussed.

Chapter 2

Computational Method

The primary objective of computational modelling and simulations is to predict and understand the properties of macroscopic systems. In atomistic scale simulations, complex chemical structures are modelled at the level of individual atoms. Knowledge gained at the atomistic level is used to understand macroscopic properties [13, 15]. For example, density of a liquid can be explained from the knowledge of interactions and packing at the atomistic level. Modelling at the level of individual atoms make atomistic scale simulations computationally expensive with limitation is size of system and time of simulations. However, with improvements in computer hardwares in last two decades, microsecond scale simulations are being achieved at the atomistic level [19, 20]. Further, to achieve higher length and time scales in simulations, degrees of freedom for groups of atoms are frozen and considered into one bead. This modelling technique is termed as coarse-graining [21]. Coarse-grained models allow a simplified picture and interpretation of complex molecular phenomena by averaging over unessential atomic details. Even higher length and timescale simulations are performed at the continuum scale, where details of atomistic details are completely

ignored and the inputs are bulk properties like viscosity, thermal conductivity etc.

In the present thesis, energetics and mechanism of interaction of water with model surfaces and interfaces is studied using all atomistic classical MD simulations. The word *classical* is used to put emphasis on the fact that, Newton's equations of motion for N interacting particles is solved in MD simulations. That is

$$m_i \frac{\partial^2 r_i}{\partial t^2} = F_i, i = 1..N \tag{2.1}$$

where m_i and r_i are the mass and position of particle i respectively, and t is the time. Force (F_i) on particle i is calculated as the negative gradient of the potential energy due to all the other particles present in the system, that is,

$$F_i = -\frac{\partial V(r_1, r_2, ..., r_N)}{\partial r_i} \tag{2.2}$$

The potential function V is a function of the position of particles present in the system. Components of this potential function are explained below. In each timestep of MD simulations these equations are solved, with incorporation of thermostats and/or barostats to maintain the ensemble of simulation. Positions and velocities of each particle in the system are written in output file referred as trajectory. The trajectory is used further for visualizing motion of particles, calculating properties to compare with experimental results, and also to compute numbers which are not available experimentally.

Generally, to perform MD simulations, three inputs are necessary - coordinates, force field, and input parameters. The initial *coordinates*, that is initial structure for MD simulation can be obtained from experiments (x-ray or NMR) or from building

model. However, if the starting structure is far away from a minima in the potential energy surface, the potential and hence forces (equation 2.2) may become extreamly large. As a result, MD simulation might fail. Thus, before performing MD simulations energy minimization is performed using steepest descent or conjugate gradient method. Also, commonly quantum chemical geometry optimizations are performed on components of the system. For example, in the present thesis self-assembly simulation of sophorolipids are performed in water starting from random configuration (chapter 9). The initial random configuration of the sophorolipids in water is generated from the geometry optimized structure of sophorolipid using quantum chemical calculations.

Force fields are parameters for sets of equations representing potential energy functions that define the interparticle potentials with respect to molecular topology. That is, it contains information of all the atoms in a molecule and their connectivities and depending upon that interaction potentials among all the particles present in the system. The interparticle potential has two components - bonded and nonbonded. Bonded potentials are further subdivided into bonds, angles, and dihedrals and nonbonded potentials into Lennard-Jones (LJ), and coulomb.

$$\begin{aligned} V &= V_{bonded} + V_{nonbonded} \\ V_{bonded} &= \sum_{bonds} \frac{1}{2} K_b (b - b_0)^2 + \sum_{angles} \frac{1}{2} K_\theta (\theta - \theta_0)^2 + \sum_{dihedrals} K_\phi (1 + cos(n\phi - \lambda)) \\ V_{nonbonded} &= \sum_{LJ} 4\epsilon_{ij} \left[\left(\frac{\sigma_{ij}}{r_{ij}} \right)^{12} - \left(\frac{\sigma_{ij}}{r_{ij}} \right)^{6} \right] + \sum_{coulomb} \frac{q_i q_j}{4\pi\epsilon_\circ r_{ij}} \end{aligned} \tag{2.3}$$

Commonly harmonic potentials are used for bonds and angles, and a cosine periodic function is used for dihedrals. K_b, K_θ, and K_ϕ are the bond, angle and dihedral constants. Values at time t is denoted by b, θ, and ϕ. Corresponding equilibrium values are denoted by subscript 0. Periodic dihedral function is defined with multiplicity n and phase λ. To keep planar groups in plane, and to prevent flipping at the chiral centres in a molecule improper dihedrals can be used. The LJ potential between particles i and j consists of an attractive tail ($-1/r^6$), a negative well depth of ϵ_{ij}, and a steep repulsive wall at distance less than $r \sim \sigma_{ij}$ [22]. q_i and q_j are the charges on corresponding particles, and r_{ij} is the distance.

In terms of bonded interactions, values of bond, angle and dihedral constants, and the corresponding equilibrium values are available in a force field, and hence are input to MD simulation. Similarly, for nonbonded interactions σ_{ij}, ϵ_{ij}, and charges for all the particles are input to MD simulations. All the parameters available in a force field (also called force field parameters), are calculated empirically. The tedious process of force field development involves calculation of these empirical force field parameters. Commonly used force fields are OPLS [23, 24], AMBER [25], CHARMM [26–28], and GROMOS [29]. They include force field parameters for different class of complex chemical moities.

The *input parameters* include all the other parameters necessary to perform MD simulations. The fundamental steps to perform MD simulation are initiation, force calculation, and integration. For initiation, position and velocity of each particle constituting the system is needed. Positions are the initial coordinates provided as input, and velocities can be generated randomly following Maxwell's distribution at the temperature (an input parameter) at which simulation is performed. Forces on each particle are calculated from the interparticle potentials defined in the force field.

These forces are used to integrate Newton's equations of motion, and hence propogate the particles in the system. Among many integration algorithms available leaf-frog algorithm [30] is commonly used. It updates the positions and velocities using the forces at time t according to the following relations

$$\begin{aligned} v(t+\frac{1}{2}\Delta t) &= v(t-\frac{1}{2}\Delta t)+\frac{\Delta t}{m}F(t) \\ r(t+\Delta t) &= r(t)+\Delta t v(t+\frac{1}{2}\Delta t) \\ r(t+\Delta t) &= 2r(t)-r(t-\Delta t)+\frac{1}{m}F(t)\Delta t^2+O(\Delta t^4) \end{aligned} \tag{2.4}$$

Δt is the time step (an input parameter) used for integration. It is chosen depending upon the frequency of bond vibration. Commonly it is taken as 1 fs. However, in certain cases, to enhance performance of simulations bond vibrations are constrained. In such cases time step of 2 fs is used. Such bond constraints are incorporated in MD simulation using LINCS [31] or SHAKE [32] algorithms.

The nonbonded interactions are pair additive. They are computed explicitly over the particles (neighbours) falling within a cut-off radius (an input parameter). Cut-off radius is defined separately for LJ and coulomb interactions. For LJ interactions shift or switch functions are used to truncate the potential smoothly beyond cut-off ([33]. Long range (beyond cut-off radius) coulomb interactions are treated with reaction-field, Ewald sum, or particle mesh Ewald method. In reaction field method [22], a medium of constant permittivity is considered beyond cut-off radius. In Ewald sum [34] method the long-range part is summed up in the Fourier space. Because of the use of Fourier sum the method assumes that the system under study is infinitely

periodic and the periodicity is taken care of by the periodic boundary conditions. In PME [34], direct summation method of the Ewald summation method is replaced by summation over point particles (particle part of PME). Further the Fourier transform of potential and charge density are also taken into account in this method as in Ewald summation (Ewald part of PME). Finally, to evaluate the Fourier transform of the charge density eld efficiently, one can use the Fast Fourier transform, which requires the density field be evaluated on a discrete lattice in space (mesh part of PME).

All the particle in the system are considered in a simulation cell to perform MD simulations. This simulation cell is replicated throughout the space to consider infinite copies. This is called periodic boundary condition (an input parameter) and are implimented to remove any boundary effects. During Simulation particles in the simulation cell and in all the replicated cells move in exactly same way [22].

The information of which statistical ensemble (NVE, NVT or NPT) to use in a simulation is an input parameter to perform MD simutation. Both temperature and pressure are directly related to total kinetic energy of an N particle system. Temperature is kept constant by coupling the system to a thermostat. Most commonly used thermostats are V-rescale [35], Berendsen [22], and Nose-Hoover [36, 37]. Similarly pressure is kept constant by coupling the system to a barostat. Commonly used barostats are Berendsen [38], and Parrinello-Rahman [39, 40].

Taking these inputs, the system is sampled over the phase space and physical properties are calculated. This sampling is performed upto the total number of steps (provided as an input parameter), integrating at each timestep. As an output positions and velocities of each particle in the system are written as a function of time (calculated as $\Delta t \times number of steps$) at certain interval defined as an input parameter. Using these outputs different properties are computed.

In the present thesis, all the simulation are performed using Gromacs simulation suit [41–43]. Gromacs is a fast and flexible parallel code to perform MD simulations. Some results reported in the present thesis are obtained using the Gromacs analysis tools. All other results are computed using self written codes. Details of such analysis codes are provided as they appear in the different chapters.

PART-A: Model Surfaces and Interfaces

Chapter 3

Introduction to Model Surfaces and Interfaces

Wetting of a surface depends primarily on the van der waals and electrostatic interactions between surface and water [3]. In addition to this, wetting of a surface is largely influenced by surface topology [44, 45]. Hierarchical structures at the surface of lotus leaves gives rise to its unparallel hydrophobicity. Water droplets sit on top of these nanostructures, and while rolling off the surface they take away the dust particles. This gives rise to self cleaning of the surface of lotus leaves and is called the lotus effect [18, 46]. Such superhydrophobic surfaces with self cleaning properties have potential applications in paints and fabric industry. Further, hydrophilicity of a hydrophilic surface is also influenced by surface structuring (or roughness). Abdelsalam et al have observed that by controlling the surface nanostructuring, hydrophillic gold surface was changed to hydrophobic[47]. Yuan et al reported that the dynamics of water droplet on flexible hydrophilic pillars is affected by the flexibility of pillars [48, 49]. But, how surface roughness or nonbonded interactions between hydrophilic suface

and water affect the wettability of a hydrophilic surface? How much energy penalty needs to be paid for wetting/dewetting of rough hydrophillic surfaces? These issues remain unresolved. Wetting of a surface and spreding of liquid on it has potential applications in oil recovery, pestiside deposit on plant leaves, and drainage of water from highways [3]. The practical applications can be delt with more efficiently if we have a molecular level understanding of the interactions responsible for wetting/dewetting phenomenon.

In addition to wetting/dewetting of nanostructured surfaces, structuring of water near nanostructures is an important phenomena to be addressed. It has major industrial and biological applications. Lyophilization is a widely used technique in pharmaceutical industry [50]. In this process, the material undergoes freezing and drying stresses. Structuring of water during these stresses might damage the material under consideration. For organisms living in subzero temperature conditions, freezing of water near cells might rupture the cell membrane. Such freezing is hindered by some antifreeze proteins [51]. Also, freezing of water present in the protein grooves might disrupt the functioning of protein. In all these examples, structuring of water near various naostructures is the fundamental issue to be addressed. Structure, dynamics, and themodynamics of water near nanostructures need to be understood at the molecular level to deal with these issues. Also, molecular level investigations would enable us to tune the hydrophobicity/hydrophilicity of nanostructures to achieve desirable properties.

In this part of the thesis energetics and mechanism of interaction of water with model surfaces are discussed. Wettability of rough hydrophilic surfaces (Figure 3.1a) and structure and dynamics of water near atomistic protrusions containing hydrophobic and hydrophilic blocks (Figure 3.1b) are studied.

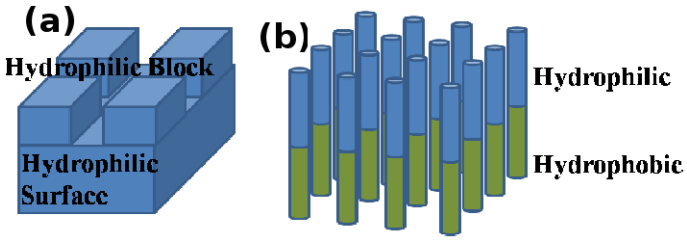

Figure 3.1: Schematic representation of (a) model rough hydrophilic surface, and (b) linear atomistic protrusions containing hydrophobic and hydrophilic blocks.

Chapter 4 deals with wetting and dewetting of rough hydrophilic surface. Roughness of a surface is defined as projected surface area divided by the actual surface area. The rough hydrophilic surfaces are constructed such that hydrophilic pillars are projected on the flat hydrophilic surface (Figure 3.1a). Water is added on top of the hydrophilic blocks (see chapter 4). Hydrophilicity is defined depending upon the Lennard-Jones interaction parameters between surface and water. Both roughness and hydrophilicity are varied to understand its effect on the energetics of wetting. The model and method to vary roughness and hydrophilicity are discussed in detail in chapter 4.

Chapter 5 deals with surfaces which are made of atomistic protrusions. The atomistic protrusions are constructed such that each protruded structure contains hydrophobic and hydrophilic blocks (Figure 3.1b). This way we have studied two different types surfaces in chapters 4 and 5. The protrusions are modelled with Lennard-Jones particles, and their hydrophobicities and hydrophilicities are defined depending upon Lennard-Jones interaction parameters with water. Water is added on top of the hydrophilic region (see chapter 5). Construction of the model system with atomistic protrusions containing hydrophobic and hydrophilic blocks, and water on top of the hydrophilic region is structurally motivated from lipid-bilayer water system

(refer chapter 6). Ordering, energetics, and residence time of water molecues near the atomistic protrusions are studied at different temperatures and pressures using classical MD simulations. The model and the range of temperature and pressure at which simulations are performed are discussed in detail in chapter 5.

Chapter 4

Wetting and Dewetting of Rough Hydrophilic Surfaces with Varying Roughness and Hydrophilicity

4.1 Introduction

A solid surface can be hydrophobic or hydrophilic dependent on the property of the material of surface. This is well known that surfaces made of hydrophobic materials repel water molecules. Surface structuring can also have significant effect on surface wetting [45, 52–54]. The hydrophobic surface can be converted into more hydrophobic (often referred as superhydrophobic) by changing it roughness [55]. A classical example is lotus effect [18, 56]. Complex surface structuring in micro and nano scale enhances the hydrophobicity of the surface of lotus leaves helping it remain dry and clean[18].

However it remains an unresolved proposition to see whether the introduction of

roughness on hydrophilic surface (i.e. the surface which has higher affinity towards water) can change its characteristics. Some experimental and theoretical evidences are present. For example, Abdelsalam et al reported, that by controlling the surface nanostructuring, hydrophillic gold surface was changed to hydrophobic[47]. It shows, favorable interaction between surface and water of hydrophilic surface can be overturned by changing the surface topology. Drelich et al. recently reviewed the superhydrophilic and superhydrophobic materials [57] based on surface topography. Yuan et al studied the dynamics of water droplet on flexible hydrophilic pillars [48, 49] in presence of external force and showed flexibility of pillars and driving force is needed to wet the surface. Spreading of a liquid on a surface i.e., wetting of the surface, is determined by the electrostatic, and van der Waals interactions between the surface and the liquid [3]. But it is still not clear that whether change in interaction between water and surface, or change in water-surface contact area (by changing the surface topology) can tune the wettability of a surface or not. Observing this, it is intuitive to ask - can structuring of any surface with affinity to attract water molecules change its wettability? If, so what are the factors, which balance the attractive and repulsive interaction and how roughness is contributing to it?

4.2 Computational Method

4.2.1 Model

In the present chapter, we have constructed model hydrophilic surfaces to understand their wetting transitions using all atom molecular dynamics (MD) simulations. The surfaces are designed with hydrophilic square pillars protruding out of the planar

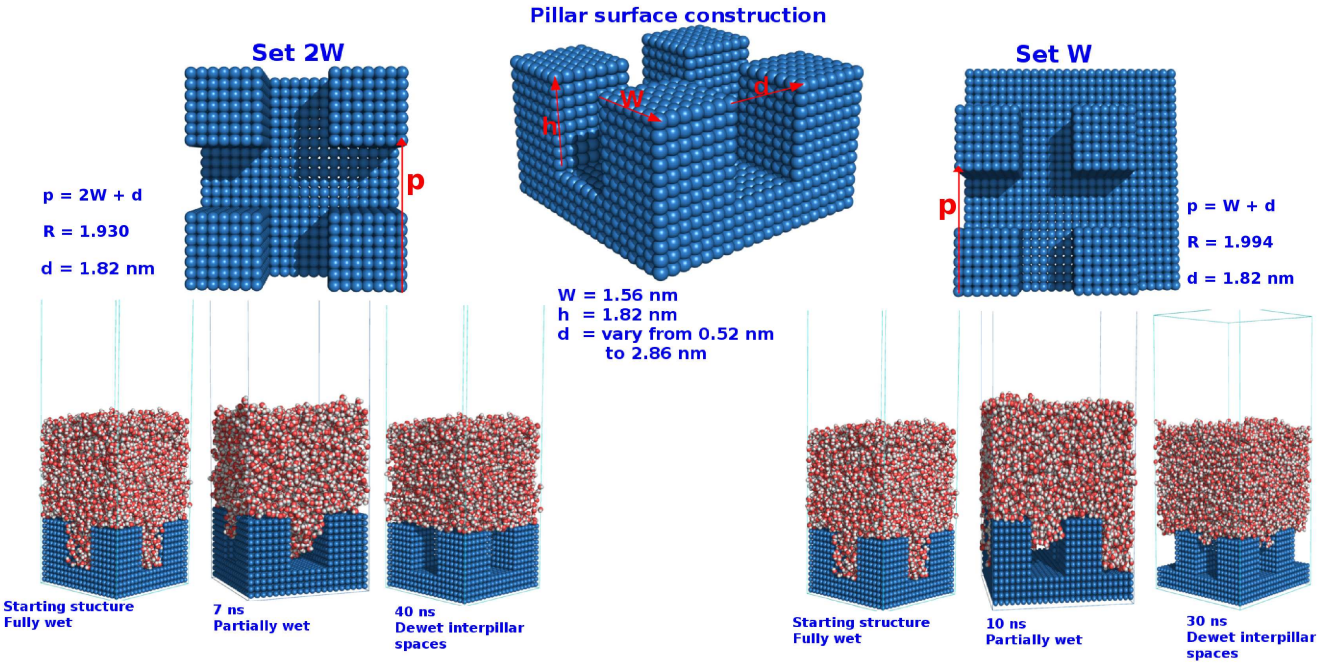

(a) **System constructions**

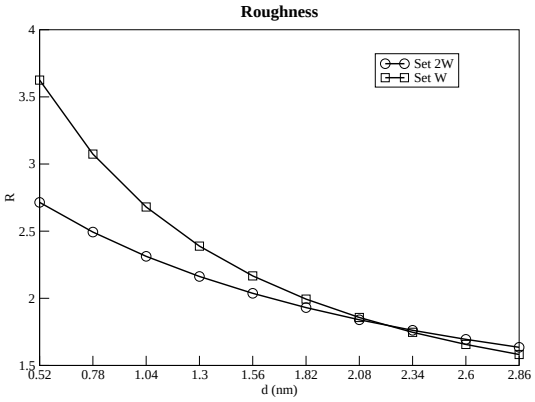

(b) **Roughness**

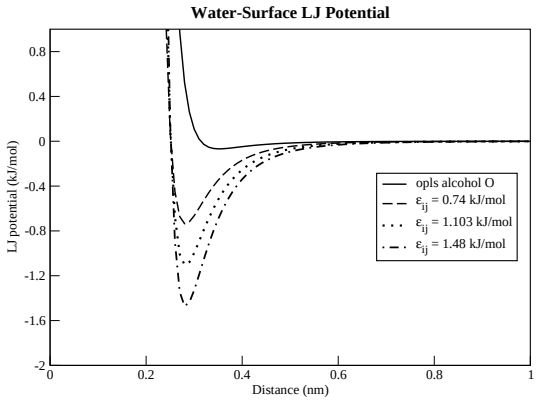

(c) **LJ plots**

Figure 4.1: (a) Construction of the surfaces, and snapshots at different time for R = 1.93 of set 2W and R = 1.994 for set W. (b) Plot of surface roughness (R) as a function of d. (c) Plot of LJ potential at different ϵ_{ij}s between particles of surface and TIP4P-water oxygen.

hydrophilic surfaces (Figure 4.1a). Square and cylindrical pillar arrayed hydrophobic surfaces have been studied in the past to vary surface morphology[45, 57, 58]. Here we have constructed two sets of square pillar surfaces differing in width (W) of the pillars. Set W with pillars width of 1.56 nm and set 2W with 3.12 nm (Figure 4.1a). In case of set 2W all the four pillars of width 1.56 nm are positioned at the corner of simulation box on the planar surface (Figure 4.1a). Due to periodic boundary condition (PBC) the effective width of the pillars of set 2W become twice (i.e., 3.12 nm) of set W. However, in case of set W, out of four pillars, two are placed at the corner, and other two are placed in the middle (Figure 4.1a) of the simulation box. Further, for sets W and 2W, series of surfaces are constructed by varying the inter-pillar spacing (d) from 0.52 nm (equivalent to one linear array particles of planar surface between the pillars) to 2.86 nm (ten array). All the surfaces are constructed by multiplying a cubic cell of side 0.26 nm. In the present chapter, height (h) of the pillars is kept constant at 1.82 nm for all the surfaces belonging to both sets.

Square surface topology, which is a function of different parameters (width, height, inter pillar spacing) can be translated to roughness[49]. Roughness (R) of the surface containing pillars considered here is defined as $R = 1 + 4wh/p^2$. Here w, h, and p are the width, height and period of the pillars respectively (Figure 4.1a). R = 1 signifies a smooth surface. R as a function of d shows continuous decrease in roughness with increasing d (Figure 4.1b). Because with increase in d we move closer to smooth surface, and hence roughness decreases. Beyond d = 2.08 nm, roughness for both sets of surfaces become similar (Figure 4.1b). Water (TIP4P[59]) is placed on top of these surfaces such that it completely wets the exposed planar surface, and the pillars in both the sets. Our objective is to recognize whether these wet hydrophilic surfaces remain completely wet, and if not how and when the transitions happen.

The interaction of water molecules with the surface is modeled via Lennard-Jones (LJ) 12-6 potential. The interaction parameters, $\sigma_{ij} = \sqrt{\sigma_{ii}\sigma_{jj}}$ and $\epsilon_{ij} = \sqrt{\epsilon_{ii}\epsilon_{jj}}$, are defined between TIP4P-water oxygen and surface atoms as σ and ϵ for TIP4P-water hydrogen are zero. For each surface belonging to sets W or 2W, the ϵ_{ij} is further varied to increase the hydrophilicity. For both sets (W and 2W) three different ϵ_{ij}s, 0.74, 1.103, and 1.48 kJ/mol were considered. The LJ-potentials between surface atom and TIP4P-water oxygen for the three ϵ_{ij}s are plotted in Figure 4.1c. As an estimate of the extent of hydrophilicity of the surfaces, LJ-potential between aliphatic alcohol in OPLS force field [23, 24] and TIP4P-water oxygen is plotted in the same figure. ϵ_{ij}s considered for the surfaces are higher than ϵ_{ij} for OPLS alcohol oxygen (Figure 4.1c). This indicates higher hydrophilicity of the particles constituting the surfaces with respect to OPLS alcohol oxygen. The particles constituting the surface are not charged.

4.2.2 Simulation Details

All the simulations are performed with GROMACS4.5.5[43]. NVT simulations were performed keeping vacuum on top of water layer in all the systems with a timestep of 1fs. Vacuum was considered on top of the water layer so that water molecules on top layer does not interact with the lower part of planer surface due to PBC. All the systems for both sets were energy minimized using steepest descent algorithm before generating the MD trajectories. The particles of surface were fixed. Temperature was kept constant at 300 K using V-rescale thermostat. Cut-off of 1 nm was used for both LJ and coulomb interactions. Long range electrostatic interactions were treated with particle mesh Ewald (PME) method.

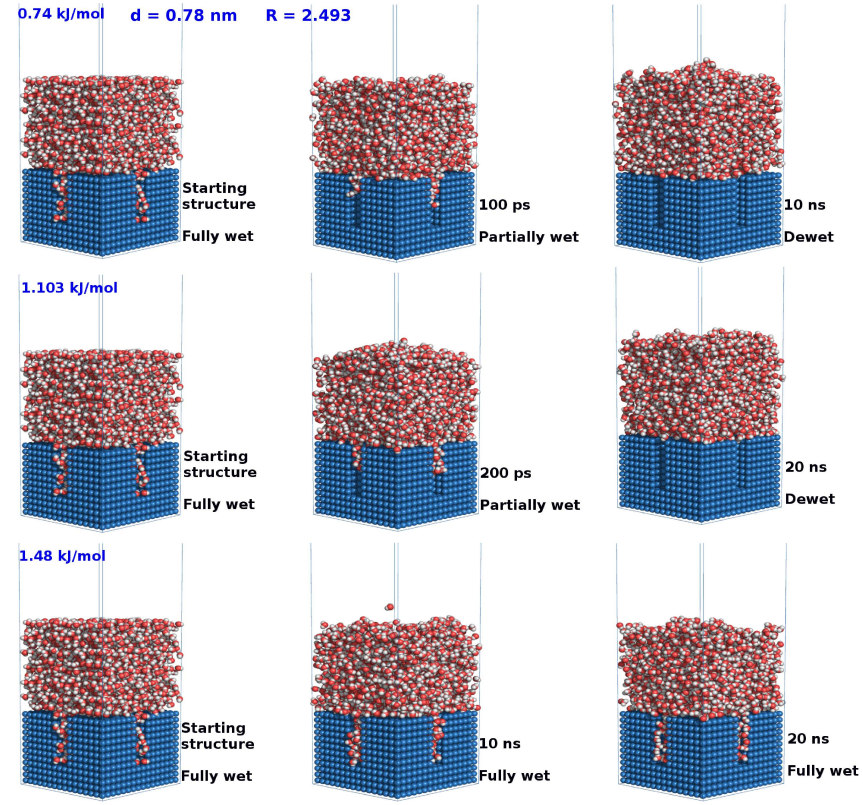

(a) **Snapshots at different ϵ_{ij} for d = 0.78 nm of set 2W**

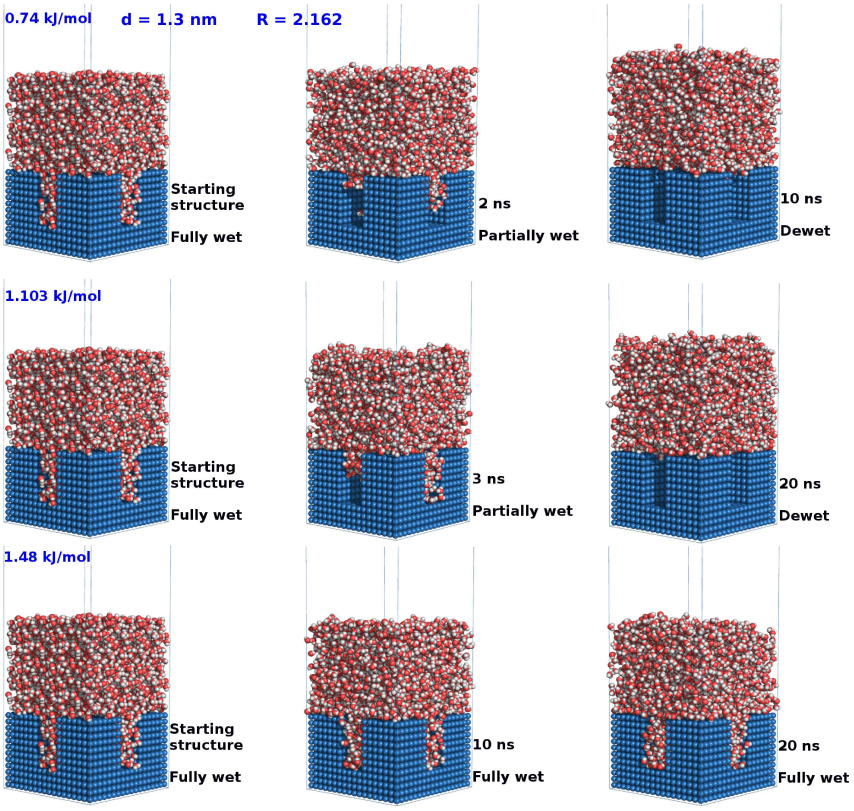

(b) **Snapshots at different ϵ_{ij} for d = 1.3 nm of set 2W**

Figure 4.2:

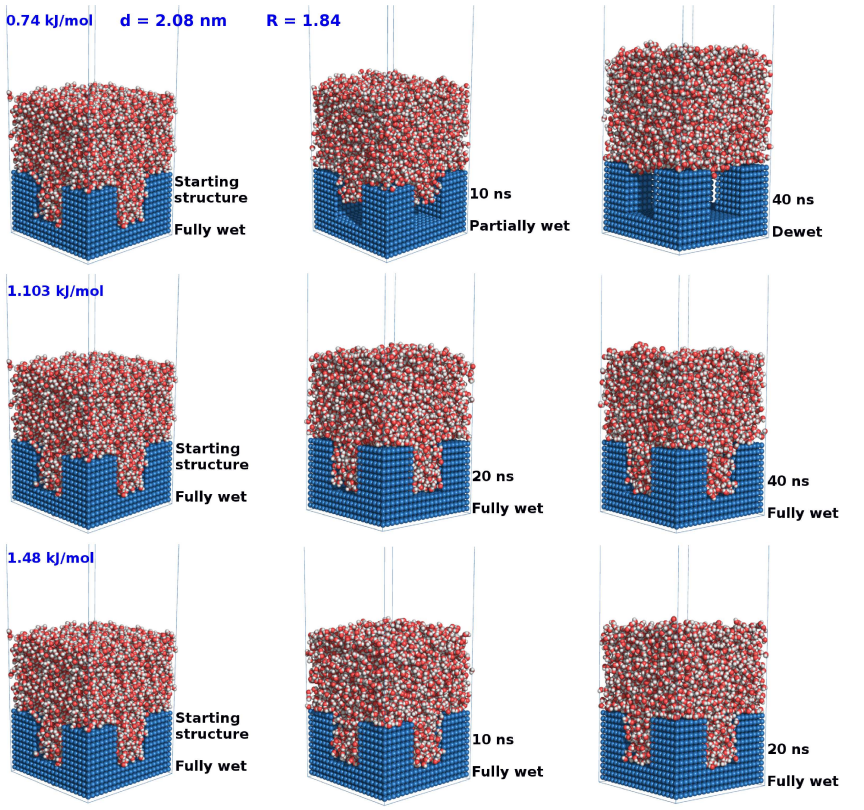

(c) **Snapshots at different ϵ_{ij} for d = 2.08 nm of set 2W**

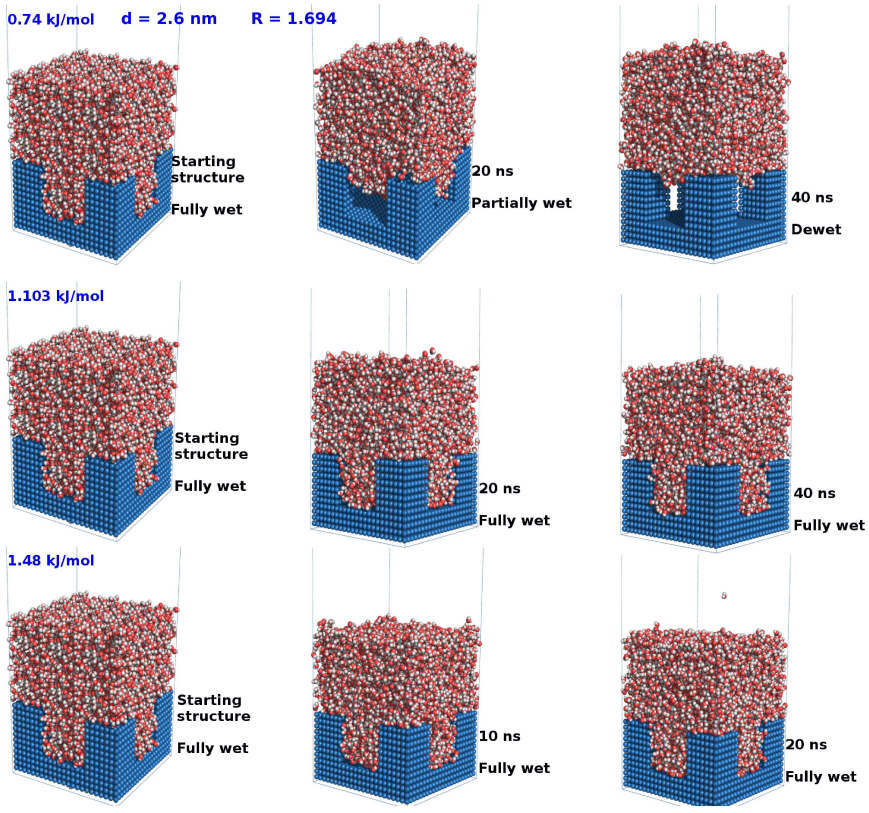

(d) **Snapshots at different ϵ_{ij} for d = 2.6 nm of set 2W**

Figure 4.2:

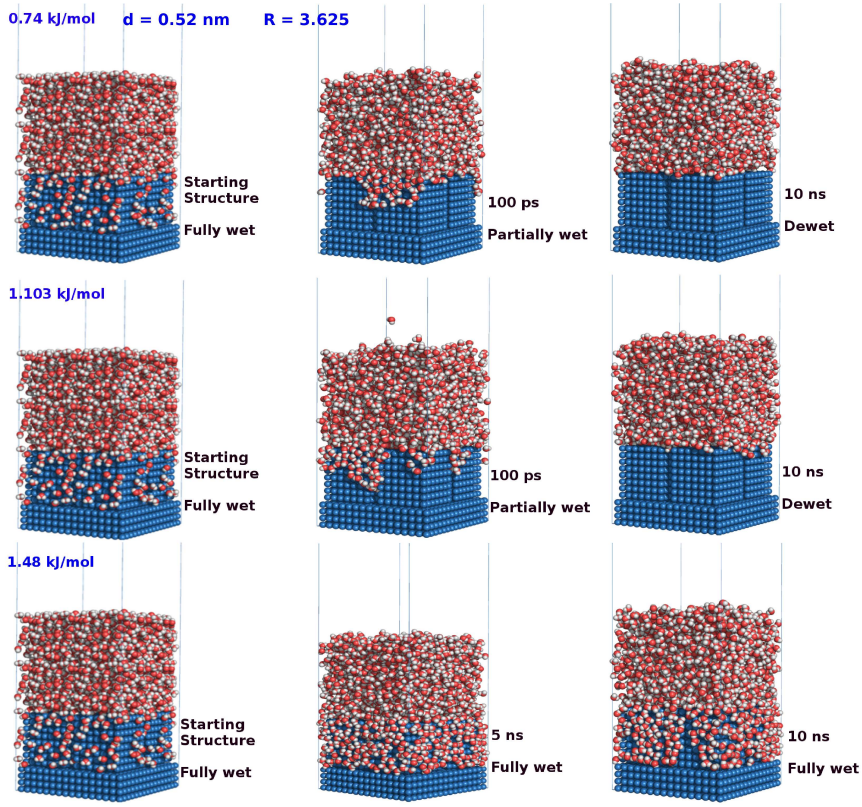

(e) **Snapshots at different ϵ_{ij} for d = 0.52 nm of set W**

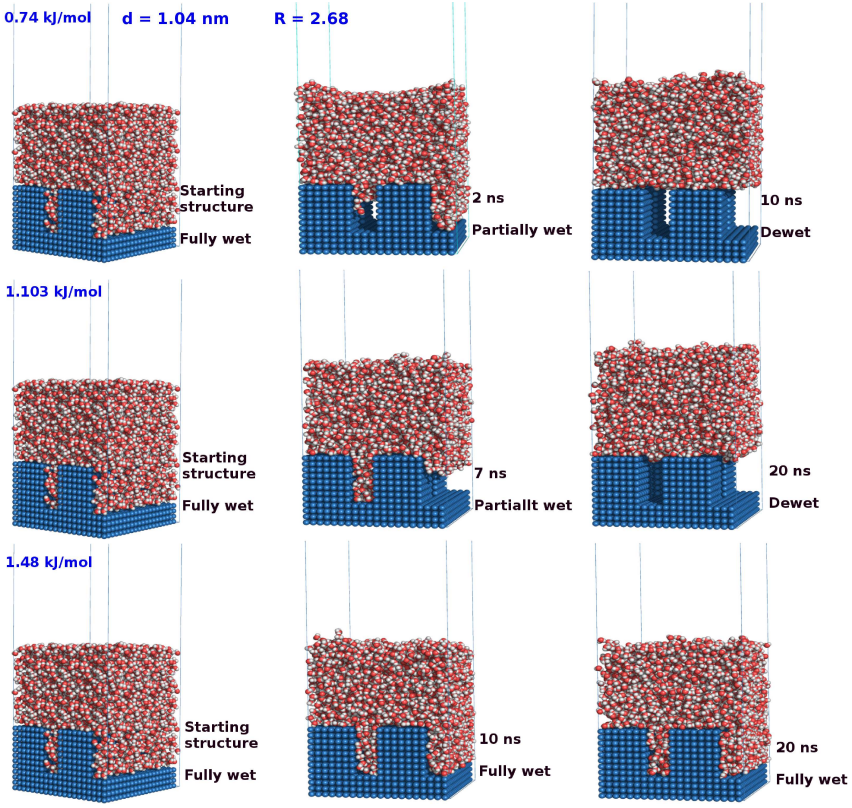

(f) **Snapshots at different ϵ_{ij} for d = 1.04 nm of set W**

Figure 4.2:

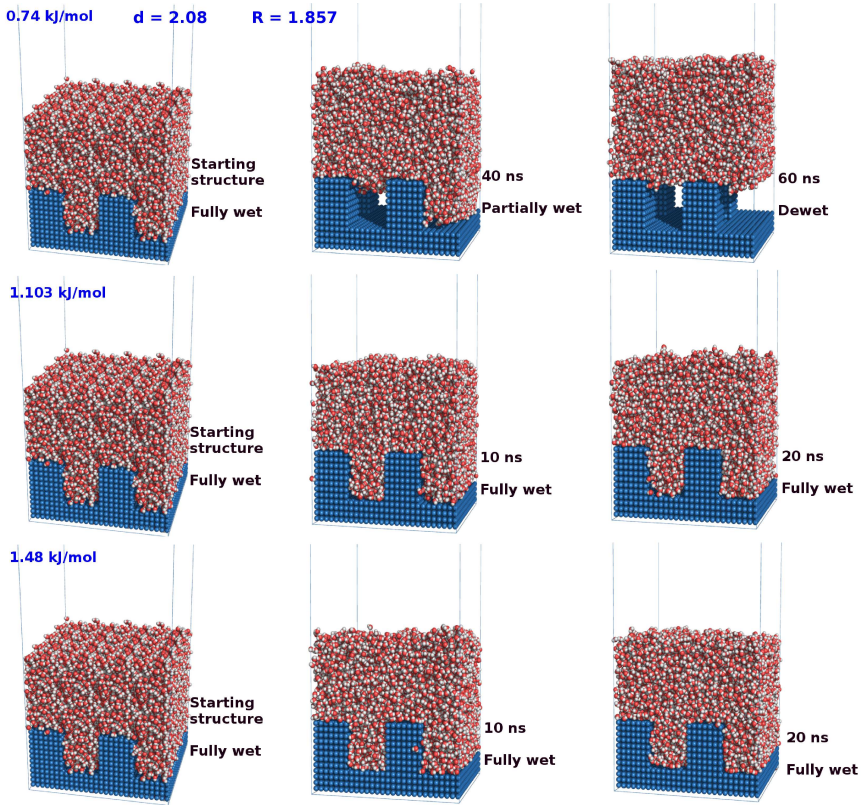

(g) **Snapshots at different ϵ_{ij} for d = 2.08 nm of set W**

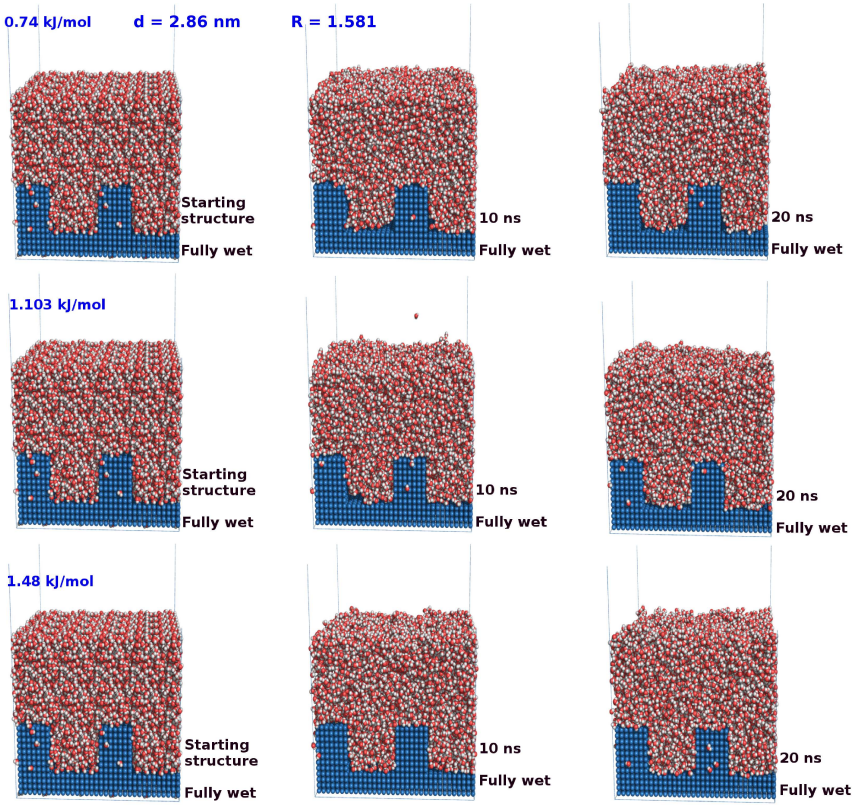

(h) **Snapshots at different ϵ_{ij} for d = 2.86 nm of set W**

Figure 4.2: Snapshots at different ϵ_{ij} for both sets of surfaces at different simulation times.

4.3 Results and Discussion

Table 4.1: Summary of final states of all the surfaces along with d and R. **Wet** indicates fully wet (planar surface and pillar walls) state, and **Dewet** indicates dewet interpillar spaces.

Set 2W

d (nm)	0.52	0.78	1.04	1.3	1.56	1.82	2.08	2.34	2.6	2.86
R	2.714	2.493	2.312	2.162	2.037	1.930	1.84	1.761	1.694	1.635
$\epsilon_{ij} = 0.74$ **kJ/mol**	Dewet	Dewet	Dewet	Dewet	Dewet	Dewet	Dewet	Dewet	Dewet	**Wet**
$\epsilon_{ij} = 1.103$ **kJ/mol**	Dewet	Dewet	Dewet	Dewet	**Wet**	**Wet**	**Wet**	**Wet**	**Wet**	
$\epsilon_{ij} = 1.48$ **kJ/mol**	**Wet**	**Wet**	**Wet**	**Wet**	**Wet**	**Wet**	**Wet**	**Wet**	**Wet**	

Set W

d (nm)	0.52	0.78	1.04	1.3	1.56	1.82	2.08	2.34	2.6	2.86
R	3.625	3.074	2.68	2.388	2.166	1.994	1.857	1.746	1.656	1.581
$\epsilon_{ij} = 0.74$ **kJ/mol**	Dewet	Dewet	Dewet	Dewet	Dewet	Dewet	Dewet	**Wet**	**Wet**	**Wet**
$\epsilon_{ij} = 1.103$ **kJ/mol**	Dewet	Dewet	Dewet	**Wet**	**Wet**	**Wet**	**Wet**	**Wet**	**Wet**	**Wet**
$\epsilon_{ij} = 1.48$ **kJ/mol**	**Wet**	**Wet**	**Wet**	**Wet**	**Wet**	**Wet**	**Wet**	**Wet**	**Wet**	**Wet**

In case of set 2W, water molecules are observed to be leaving the inter-pillar spaces as roughness decreases till R = 1.694 (where, d = 2.6 nm) at $\epsilon_{ij} = 0.74$ kJ/mol. That is, in the final state, only the top surface of the pillars is wet, and the inter-pillar spaces have undergone dewetting (Figure 4.1a). But, on increasing the ϵ_{ij} to 1.103 kJ/mol dewetting of inter-pillar spaces takes place only till R = 2.162 (d = 1.3 nm). And beyond R = 2.162, surface remains completely wet including the inter-pillar space in the final state. On further increasing ϵ_{ij} to 1.48 kJ/mol there is no dewetting observed even at R = 2.714 (d = 0.52 nm). All these observations for both the sets of surfaces are summarized in Table 4.1. In case of set W dewetting of inter-pillar spaces occur till R = 1.857 (d = 2.08 nm, whereas in set 2W water comes out till R = 1.694 (d = 2.6 nm)) at $\epsilon_{ij} = 0.74$ kJ/mol (Table 4.1). At $\epsilon_{ij} = 1.103$ kJ/mol dewetting occurs till R = 2.68 (upto R = 2.162 for set 2W). And akin to set 2W no

dewetting takes place at ϵ_{ij} = 1.48 kJ/mol for set W (Table 4.1). The dewetting of inter-pillar spaces occurs through a partially wet state (Figure 4.1a) for both set W and 2W. In the partially wet state, the planar hydrophilic surface and the pillar walls are partly wet as some water molecules already started to move out to the bulk. For d upto 1.56 nm and ϵ_{ij} = 0.74 kJ/mol, the systems are simulated upto 10 ns for set W. 20 ns simulation is performed for set 2W for d = 1.3 and 1.56 nm. For larger d, on an average 40 ns simulations (in some cases 50 ns and 60 ns) are performed. Choice of simulation times have been made depending upon appearance of partially wet states. Dewetting takes place only through the partially wet states. That is why at ϵ_{ij} = 1.48 kJ/mol for both sets, simulations were not extended beyond 20 ns as no patially wet states appear and all the surfaces remain fully wet similar to the starting structure. Snapshots for different roughnesses at different ϵ_{ij} are provided in Figure 4.2 at different simulation times. Studying two different sets of surfaces with varying ϵ_{ij}s gives us the chance to understand the wetting to dewetting transition as a function of water-surface contact area (different roughnesses), and surface hydrophilicity.

Further to quantify the time at which water molecules completely dewets the inter-pillar spaces, the z-component of center of mass (CMz) of all the water molecules is plotted as a function of time in Figure 4.3 for all the surfaces of set 2W and W at ϵ_{ij} = 0.74 kJ/mol. CMz increases initially and then fluctuates near a constant value for all the roughnesses for which water moves out of the interpillar spaces (Table 4.1) to the bulk. But for R = 1.635 of set 2W, and R = 1.746, 1.656, and 1.581 of set W, for which water molecules do not move out, CMz fluctuates near a constant value for whole simulation time. The initial increase in CMz is indicative of appearance of partially wet states where some water molecules have moved to the bulk. When the inter-pillar spaces are completely dewet, that is no water to move to the bulk, the CMz

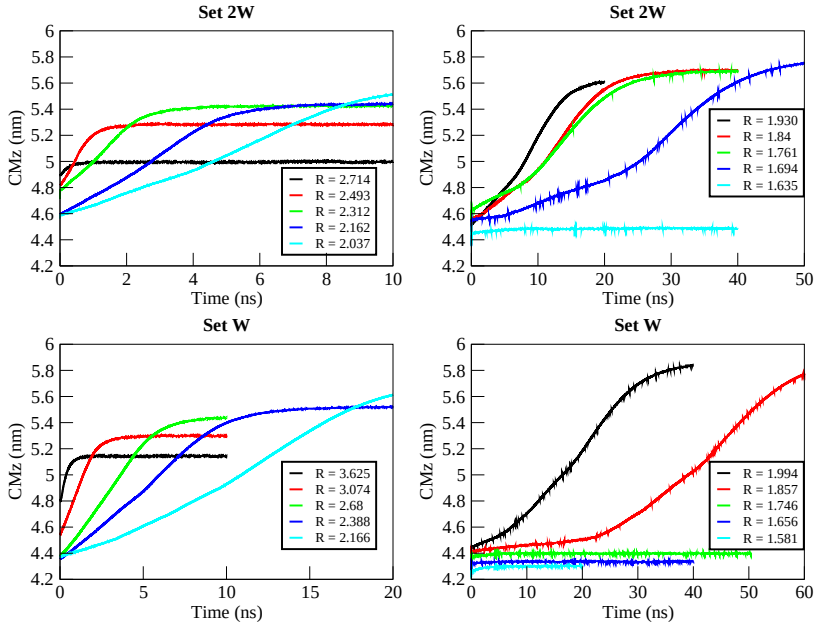

Figure 4.3: Z-component of centre of mass of water as a function of time at different roughness for both sets.

fluctuates near a constant value. This also justifies our choice of simulation times. If the initial slope was observed, we kept extending the simulation to achieve complete dewetting. Also, it indicated that for the wet cases (Table 4.1) longer simulations will not make difference. These observations and their explanations can also be translated to CMz plot for $\epsilon_{ij} = 1.103$ kJ/mol (where surface remains completely wet after certain R) and 1.48 kJ/mol (completely wet at all R) illustrated in Figure 4.4 for both 2W and W sets.

Now, it is necessary to understand why the water molecules leave the inter-pillar spaces of the hydrophilic surfaces and move to the bulk. The wetting or dewetting of the surfaces should, in principle, be guided by atomic level water-water and water-surface non-bonded interactions. The interplay of nonbonded interactions between water-surface, and water-water should play the decisive role in this observation. Thus,

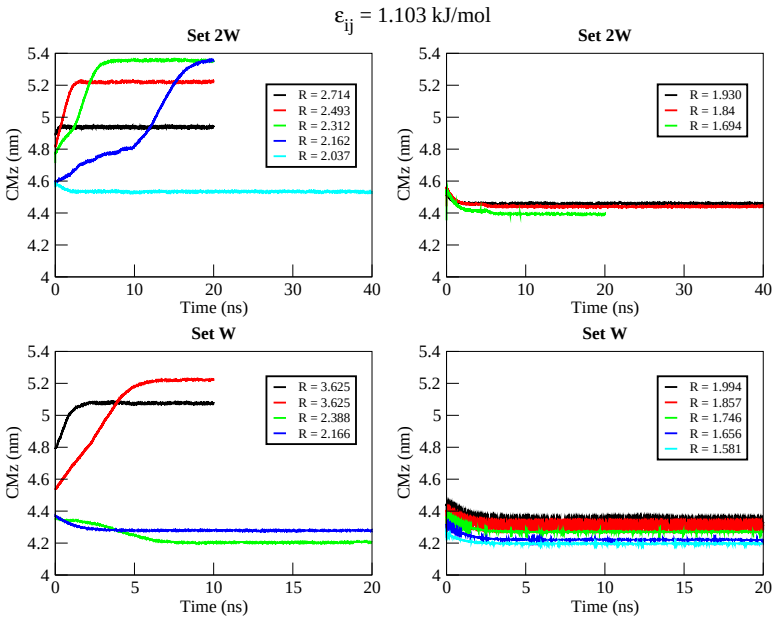

(a)

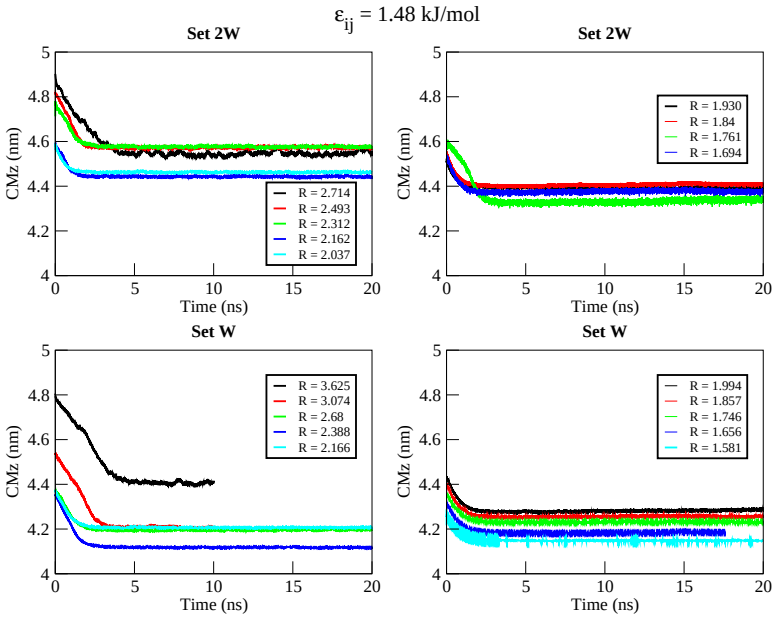

(b)

Figure 4.4: Z-component of centre of mass of water at $\epsilon_{ij} = 1.103$ kJ/mol, and $\epsilon_{ij} = 1.48$ kJ/mol for both sets and different roughness values.

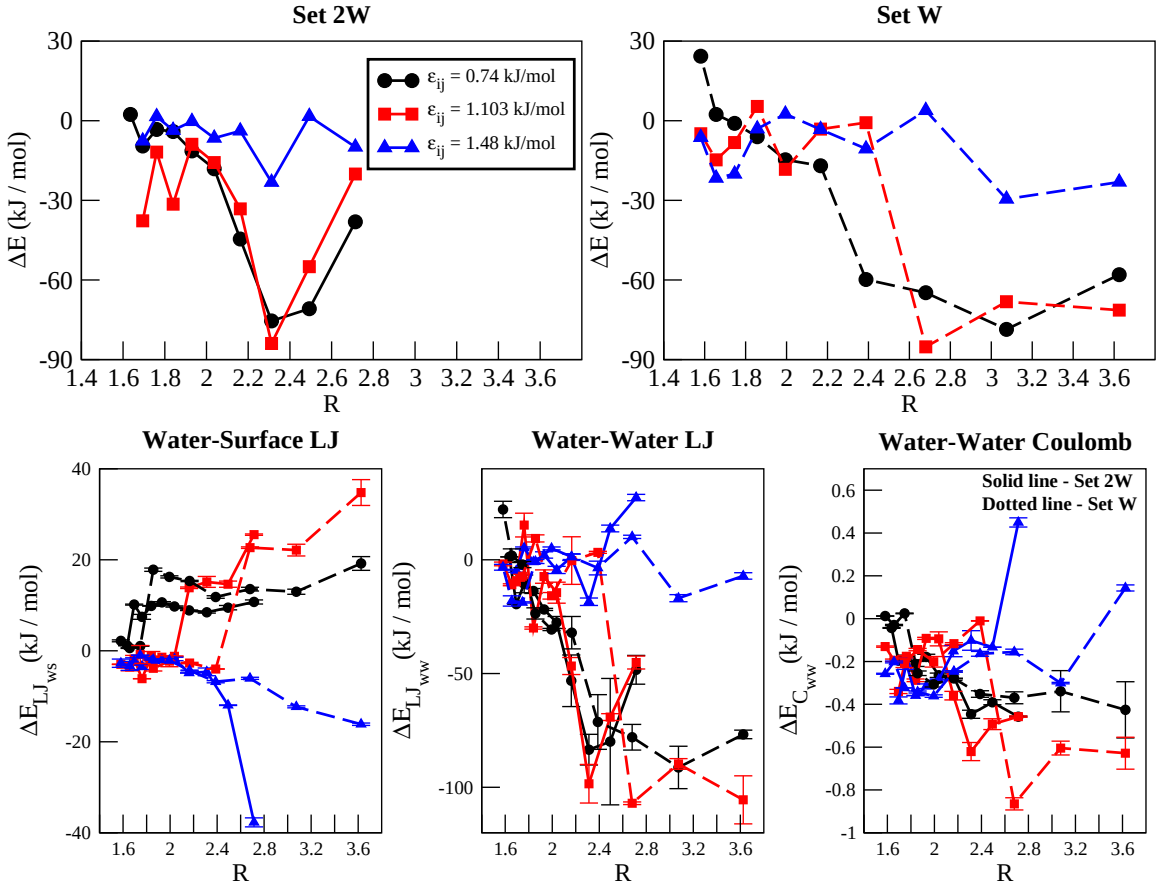

Figure 4.5: ΔE as a function of time for both sets along with individual components of ΔE as a function of R.

the change in nonbonded potential energy (PE) between final (wet or dewet), and initial (wet) states (ΔE) for all the surfaces belonging to sets W and 2W are calculated as,

$$\Delta E = \Delta E_{LJ_{ws}} + \Delta E_{LJ_{ww}} + \Delta E_{C_{ww}} \tag{4.1}$$

where $\Delta E_{LJ_{ws}}$ is the change in water-surface LJ potential energy, $\Delta E_{LJ_{ww}}$ is the change in water-water LJ potential energy, and $\Delta E_{C_{ww}}$ is the change in water-water electrostatic potential energy. The individual PE changes are calculated as the dif-

ference between average PE of last 100 frames, and average PE of initial 100 frames. Plots of ΔE as a function of R are depicted in Figure 4.5. More negative the value of ΔE, more favorable is the final state (wet or dewet). At ϵ_{ij} = 0.74 kJ/mol for both sets 2W and W, ΔE moves towards more negative value at higher roughness (low d), but moves towards zero at lower roughness (high d). It indicates, at R = 2.714 and 2.493 for set 2W, and R = 3.625 and 3.074 for set W (d = 0.52 and 0.78 nm) dewetting of the inter-pillar spaces is energetically favorable. But, as roughness decreases PE difference between final and initial states decreases and eventually it should go to zero. Similar trend can be observed at ϵ_{ij} = 1.103 kJ/mol for both the cases (Figure 4.5). PE difference increases with increase in roughness. The difference observed is due to the water molecules which leave the inter-pillar spaces. Further, at ϵ_{ij} = 1.48 kJ/mol, where there is no dewetting even at R = 2.714 for set 2W and R = 3.625 for set W (d = 0.52 nm), ΔE does not change much with decrease in roughness for both sets. The small change in energy is due to the rearrangement of the water molecules.

Table 4.2: ΔE values and its components for set 2W at different ϵ_{ij}

Set 2W $\epsilon_{ij} = 0.74$ kJ/mol

d	R	ΔE (kJ/mol)	$\Delta E_{LJ_{ws}}$ (kJ/mol)	$\Delta E_{LJ_{ww}}$ (kJ/mol)	$\Delta E_{C_{ww}}$ (kJ/mol)
0.52	2.714	-38.080894	10.731342 ± 0.443288	-48.354736 ± 6.326073	-0.4575 ± 0.002468
0.78	2.493	-70.83762	9.482819 ± 0.478596	-79.929993 ± 27.771911	-0.390446 ± 0.0116
1.04	2.312	-75.444309	8.462338 ± 0.188891	-83.460388 ± 6.748348	-0.446259 ± 0.01890
1.3	2.162	-44.556145	8.881897 ± 0.049449	-53.168884 ± 11.343274	-0.269158 ± 0.02001
1.56	2.037	-18.095124	9.736079 ± 0.132774	-27.566864 ± 2.64561	-0.264339 ± 0.0102
1.82	1.930	-11.374915	10.630094 ± 0.163261	-21.825928 ± 0.448662	-0.179081 ± 0.01308
2.08	1.84	-4.066328	9.867022 ± 0.076055	-13.721802 ± 1.067309	-0.211548 ± 0.01165
2.34	1.761	-3.287458	7.462638 ± 0.547181	-10.568116 ± 3.899197	-0.18198 ± 0.01154
2.6	1.694	-9.531394	10.152413 ± 0.105587	-19.487976 ± 0.068813	-0.195831 ± 0.00741
2.86	1.635	2.358015	1.132105 ± 0.037955	1.269165 ± 0.00156	-0.043255 ± 0.00175

Set 2W $\epsilon_{ij} = 1.103$ kJ/mol

d	R	ΔE (kJ/mol)	$\Delta E_{LJ_{ws}}$ (kJ/mol)	$\Delta E_{LJ_{ww}}$ (kJ/mol)	$\Delta E_{C_{ww}}$ (kJ/mol)
0.52	2.714	20.075717	25.534615 ± 0.15202	-45.152832 ± 2.841505	-0.4575 ± 0.003243
0.78	2.493	-54.993543	14.638473 ± 0.674016	-69.13913 ± 1.511941	-0.492886 ± 0.02536
1.04	2.312	-83.933246	15.139901 ± 1.20692	-98.452576 ± 8.485258	-0.620571 ± 0.04221
1.3	2.162	-33.208093	13.848505 ± 0.171377	-46.69693 ± 3.738744	-0.359668 ± 0.02000
1.56	2.037	-15.753966	-1.204043 ± 0.055493	-14.455658 ± 4.611302	-0.094265 ± 0.03272
1.82	1.930	-8.880536	-1.411298 ± 0.01086	-7.37738 ± 2.94418	-0.091858 ± 0.00487
2.08	1.84	-31.440489	-1.1877 ± 1.021993	-29.964966 ± 0.503731	-0.287823 ± 0.00620
2.34	1.761	8.918748	-6.127238 ± 0.016514	15.25116 ± 5.212396	-0.205174 ± 0.0033
2.6	1.694	-11.228718	-1.807194 ± 0.783406	-9.174927 ± 0.221459	-0.246597 ± 0.00974
2.86	1.635				

Set 2W $\epsilon_{ij} = 1.48$ kJ/mol

d	R	ΔE (kJ/mol)	$\Delta E_{LJ_{ws}}$ (kJ/mol)	$\Delta E_{LJ_{ww}}$ (kJ/mol)	$\Delta E_{C_{ww}}$ (kJ/mol)
0.52	2.714	-9.89991	-37.707569 ± 0.99333	27.358246 ± 1.389778	0.449413 ± 0.021614
0.78	2.493	1.661608	-11.962736 ± 0.062837	13.757538 ± 1.467129	-0.133194 ± 0.000089
1.04	2.312	-23.175373	-4.632553 ± 0.853058	-18.44097 ± 1.645416	-0.101841 ± 0.045748
1.3	2.162	-3.834587	-4.866821 ± 0.005226	1.183533 ± 1.462768	-0.151299 ± 0.026385
1.56	2.037	-6.543327	-1.792374 ± 0.382331	-4.466614 ± 1.570245	-0.284339 ± 0.00201
1.82	1.930	-0.256939	-2.049271 ± 0.22105	2.107849 ± 1.393315	-0.315517 ± 0.010951
2.08	1.84	-3.585407	-2.290394 ± 0.478352	-0.936035 ± 0.549262	-0.358978 ± 0.0004
2.34	1.761	1.572788	-3.441254 ± 0.674998	5.224304 ± 0.42398	-0.210262 ± 0.026282
2.6	1.694	-7.588452	-2.361065 ± 0.811555	-4.845459 ± 0.636573	-0.381928 ± 0.016303
2.86	1.635				

Table 4.3: ΔE values and its components for set W at different ϵ_{ij}

Set W $\epsilon_{ij} = 0.74$ kJ/mol

d	R	ΔE (kJ/mol)	$\Delta E_{LJ_{ws}}$ (kJ/mol)	$\Delta E_{LJ_{ww}}$ (kJ/mol)	$\Delta E_{C_{ww}}$ (kJ/mol)
0.52	3.625	-58.001318	19.195818 ± 1.506192	-76.771241 ± 1.887105	-0.425895 ± 0.131232
0.78	3.074	-78.628759	12.982218 ± 0.557615	-91.271972 ± 9.328928	-0.339005 ± 0.096216
1.04	2.68	-64.812972	13.555501 ± 0.411874	-77.998993 ± 5.621459	-0.36948 ± 0.027926
1.3	2.388	-59.821296	11.826859 ± 0.282078	-71.296325 ± 12.03055	-0.35183 ± 0.015395
1.56	2.166	-16.978319	15.336379 ± 0.137854	-32.03534 ± 7.125768	-0.279358 ± 0.00157
1.82	1.994	-14.69315	16.239532 ± 0.247053	-30.625916 ± 0.481833	-0.306766 ± 0.012375
2.08	1.857	-6.017164	17.820609 ± 0.353837	-23.582825 ± 2.458036	-0.254948 ± 0.010695
2.34	1.746	-1.007049	1.042427 ± 0.034009	-2.074218 ± 1.351775	0.024742 ± 0.001767
2.6	1.656	2.363716	0.590668 ± 0.068335	1.802734 ± 3.001137	-0.029686 ± 0.003098
2.86	1.581	24.309361	2.181515 ± 0.211279	22.115479 ± 3.610202	0.012367 ± 0.000932

Set W $\epsilon_{ij} = 1.103$ kJ/mol

d	R	ΔE (kJ/mol)	$\Delta E_{LJ_{ws}}$ (kJ/mol)	$\Delta E_{LJ_{ww}}$ (kJ/mol)	$\Delta E_{C_{ww}}$ (kJ/mol)
0.52	3.625	-71.368777	34.775407 ± 2.838974	-105.51596 ± 10.55244	-0.628224 ± 0.074661
0.78	3.074	-68.202676	22.133009 ± 1.295963	-89.731353 ± 2.338198	-0.604332 ± 0.032397
1.04	2.68	-85.196958	22.675497 ± 0.166264	-107.00759 ± 0.574842	-0.864857 ± 0.028404
1.3	2.388	-0.736108	-4.004076 ± 0.044169	3.27826 ± 0.426929	-0.010292 ± 0.001097
1.56	2.166	-3.147365	-2.688926 ± 0.145815	-0.341797 ± 10.44803	-0.116642 ± 0.004387
1.82	1.994	-18.312164	-2.277332 ± 1.21782	-15.833436 ± 1.45107	-0.201396 ± 0.024718
2.08	1.857	5.383931	-3.853683 ± 0.58713	9.38202 ± 1.559067	-0.144406 ± 0.005529
2.34	1.746	-8.223311	-0.817508 ± 1.981641	-7.200073 ± 0.812763	-0.20573 ± 0.022299
2.6	1.656	-14.736919	-3.575119 ± 0.824913	-10.967285 ± 0.412821	-0.194515 ± 0.005661
2.86	1.581	-4.91016	-2.963833 ± 0.050885	-1.81604 ± 0.826672	-0.130287 ± 0.002973

Set W $\epsilon_{ij} = 1.48$ kJ/mol

d	R	ΔE (kJ/mol)	$\Delta E_{LJ_{ws}}$ (kJ/mol)	$\Delta E_{LJ_{ww}}$ (kJ/mol)	$\Delta E_{C_{ww}}$ (kJ/mol)
0.52	3.625	-23.098655	-16.142486 ± 0.25274	-7.099487 ± 1.423689	0.143318 ± 0.014267
0.78	3.074	-29.505142	-12.312595 ± 0.218418	-16.891602 ± 1.565956	-0.300945 ± 0.003542
1.04	2.68	3.871083	-6.055343 ± 0.232822	10.081756 ± 0.720705	-0.15533 ± 0.012925
1.3	2.388	-10.572865	-6.796856 ± 0.241983	-3.611878 ± 1.026186	-0.164131 ± 0.011168
1.56	2.166	-3.278979	-4.317627 ± 0.08457	1.285218 ± 1.184413	-0.24657 ± 0.003485
1.82	1.994	2.529567	-2.1194 ± 0.446322	5.010498 ± 0.633693	-0.361531 ± 0.005696
2.08	1.857	-3.045656	-1.947533 ± 0.106387	-0.755616 ± 0.867153	-0.342507 ± 0.004592
2.34	1.746	-20.066719	-0.993034 ± 0.034258	-18.750245 ± 0.262118	-0.32344 ± 0.000007
2.6	1.656	-21.626346	-3.321266 ± 0.982959	-18.102783 ± 2.265552	-0.202297 ± 0.004353
2.86	1.581	-6.265331	-2.731079 ± 0.903877	-3.276855 ± 1.281009	-0.257397 ± 0.002253

Observing the trends in ΔE it is imperative to envisage the trends of individual components constituting ΔE. Plots of $\Delta E_{LJ_{ws}}$, $\Delta E_{LJ_{ww}}$, and $\Delta E_{C_{ww}}$ are also depicted in Figure 4.5. And the values of ΔE and its components are summerized in Table 4.2 and 4.3. $\Delta E_{C_{ww}}$ is small for all roughnesses at all ϵ_{ij}s for both the sets compared to other components. Thus contribution from $\Delta E_{C_{ww}}$ to ΔE is least. So the cohesive interaction due to electrostatic interaction between water molecules do not have much role to play in wetting. However, the value of $\Delta E_{LJ_{ws}}$ is positive for the roughness values where water dewets the interpillar spaces. Because, in the dewet state, only the upper surface of the pillars are wet. This is unfavorable in terms of water-surface nonbonded PE, as compared to the fully wet state where surface-water contact area is higher. But, for roughness values where there is no dewetting (R = 1.635 for set 2W at ϵ_{ij} = 0.74 kJ/mol, R = 1.581 to 1.746 for set W at ϵ_{ij} = 1.103 kJ/mol etc.) value of $\Delta E_{LJ_{ws}}$ is smaller (or almost no change). The observed value is due to the rearrangement of water molecules. $\Delta E_{LJ_{ww}}$ shows favorable negative values for roughness values where dewetting occurs. Then slowly moves towards zero as roughness is decreased. It can be observed that the trend in ΔE is primarily guided by $\Delta E_{LJ_{ww}}$. It is evident that there exists a competition between $\Delta E_{LJ_{ww}}$ and $\Delta E_{LJ_{ws}}$. With decrease in roughness, the contact area (not calculated in this work) between water and surface increases, hence the volume of water filling the inter-pillar spaces also increases. Now, dewetting of the inter-pillar spaces implies that water molecules vacate the interpillar spaces and move to the bulk because of favorable interaction. But, to influence the water molecules (by favorable energy) to remain in the inter-pillar spaces $\Delta E_{LJ_{ws}}$ has to overcome $\Delta E_{LJ_{ww}}$. Thus, at $\epsilon_{ij} = 0.74$, with decrease in roughness the difference between $\Delta E_{LJ_{ws}}$ and $\Delta E_{LJ_{ww}}$ (Figure 4.5) decreases and the surfaces remain wet after certain value of R. At ϵ_{ij} = 1.103 kJ/mol, the water-surface

interaction is more favorable than that of 0.74 kJ/mol, thus roughness below which the surfaces remain wet is also much higher. At $\epsilon_{ij} = 1.48$ kJ/mol, difference between $\Delta E_{LJ_{ws}}$ and $\Delta E_{LJ_{ww}}$, remain in the range of wet roughness values of 0.74 kJ/mol and 1.103 kJ/mol. Hence, wetting or dewetting is guided by both roughness and ϵ_{ij}. There is not much difference in the wetting and dewetting behaviors of surfaces belonging to set 2W and W with respect to change in roughness at a certain ϵ_{ij}. This is possibly because after certain d there is not much difference in roughness of the surfaces. Similar roughness can be achieved from completely different set of width of the pillars, inter-pillar distances and heights (variation in height has not been explored in this work). However it seems that wetting to dewetting transition very well follow the unified roughness parameter and gives a predictable observation for certain value of ϵ_{ij}.

Kim et al have studied the drying of the inter-pillar spaces in *hydrophobic* surfaces using grand canonical Monte Carlo simulations[55]. They have studied the dependency of drying on the shape and size of the *hydrophobic* pillars. In the present chapter, we have observed drying of inter-pillar spaces of *hydrophilic* surfaces. We have also explored the critical d and ϵ_{ij} beyond which the dewetting transition does not occur. We may infer that nano-structuring guides the *hydrophilicity* of a hydrophilic surface depending upon both surface topology (in terms of roughness), and the interaction parameters (ϵ_{ij}).

4.4 Conclusion

To conclude this chapter, we have studied wetting and dewetting of hydrophilic pillar surfaces using MD simulations. We have observed that the interpillar spaces un-

dergo dewetting above certain roughness and below certain ϵ_{ij}. Competition between LJ potential energy among water-water, and water-surface guides the wetting and dewetting transitions. These, in turn, depend upon the volume of water present in the interpillar spaces, and hence water-surface contact area. Though, in this chapter, we have varied the W and d of the pillars there is scope of further varying the height of the pillars to understand its effect on wetting. Also the width of the square pillar can be further varied. Changing W and d both will affect roughness. In addition to this, shape of the pillars can also be varied. Thus there is plenty of scope to extend the observations gathered here to further investigate and understand wetting of hydrophilic surfaces.

In chapter 5, construction of the model surface is further varied with introduction of hydrophobic block. However, interface of water is maintained with hydrophilic block.

[1]The results and figures are adapted from the publication P. R. Pandey and S. Roy, Is it Possible to Change Wettability of Hydrophilic Surface by Changing its Roughness?, The Journal of Physical Chemistry Letters, 2013, 4(21), 3692-3697.

Chapter 5

Retention and Ordering of Water at Surface and Interface made of Model Atomistic Protrusions

5.1 Introduction

In the previous chapter (chapter 4), interface of water-model surface were discussed with the motivation to understand their wetting and dewetting behaviour. In the present chapter, the construction of the model surface has been modified, and hydrophobicity is introduced in the model. Interface of water-model surface is studied with the motivation to understand the structure and dynamics of water near model atomistic protrusions. Also, effect of temperature and pressure on the structure and dynamics of water near atomistic protrusions have also been elucidated.

Water is present in nature as bulk, as well as in confined regions with different structural arrangement than bulk. Water inside confined regions has drawn signif-

icant amount of research attention in the recent past [60, 61]. Confined water is structurally different and show properties not similar to bulk [62]. The importance, and characteristics of confined water has been envisaged in varied range of systems. Biological systems (protein grooves, cell membranes) [9, 10], nanostructured materials [63, 64], geological systems [65] have been studied experimentally and theoretically with the motivation to understand the structure and dynamics of water present under confinement. In addition to structure and dynamics, phase behavior of water inside confined regions were also studied in the past [66]. This is because confinement is capable of inducing melting-freezing, wetting-drying transitions, and also prewetting and predrying transitions (reference [66] and references therein). The effect of confinement of water on its structuring has been discussed by Mancinelli [61].

Molecular dynamics (MD) simulations have been used extensively in understanding of molecular level structure and dynamics of water inside confined regions. Phase behavior of water confined inside hydrophobic surfaces was studied by using MD simulations by Koga et al [66]. They have analyzed the structural, and thermodynamical aspects of water inside the hydrophobic surfaces. Johnston et al. have studied the phase behavior of water inside Lennard-Jones (LJ) 9-3 walls [67]. Phase diagram of water was investigated inside carbon nanoube (CNT) by Takaiwa et al. as a function of diameter of the tube [62]. Khan et al. have studied wetting of textured surfaces by nanodroplets using MD simulations [68]. Rotational entropy of water inside CNT was studied by Kumar et al. [69]. Lombardo et al. have investigated the mechanical and structural properties of glassy water confined inside atomistic silica based surfaces [70]. Bauer et al. have studied the effect of confined water on the energetics of assembly of large hydrophobic plates [71]. All these studies are performed either in model systems or in nano-structured materials and collectively explained

the structural, and thermodynamical properties of confined water. These properties are expected to be tunable by changing the parameters (hydrophobicity, roughness, dimension and volume of confinement) of the model systems or changing the pattern and chemical constituent of the nano-structured materials. Changing chemical constituent can be resembled with changing hydrophobic or hydrophilic strength of the material. There is high possibility of existence of combination of both hydrophobic and hydrophilic nature in the same nano-structure which can alter the properties of water differently confined in it. Therefore, a model system with varied hydrophilicity and hydrophobicity may help in achieving desirable ordering and retention of water molecules in confined region or on its surface/interface. The know-how gained from such model system will further allow designing nano-structures with desirable properties and better understanding of the process of structuring of water. The design and morphology of the model can further be varied to approach closer to a real system. Designing such a model with incremental changes will further facilitate designing and understanding smart materials with *a priori* knowledge of the parameters to achieve desirable structuring and retention.

For organisms living in extremely cold conditions (below freezing point of water) freezing of water inside the cells can be life threatening. They withstand such drastic conditions by inhibiting freezing of water and hence ice formation by the use of some antifreeze proteins [51]. Lyophilization is a widely used technique for preservation in pharmaceutical industry [50]. This process involves freezing, followed by drying of the material for preservation. However, during the process of freezing, ordering of water molecules is capable to damage the material. In the above examples structuring of water in ordered fashion near nano-structures is the fundamental aspect to address. Thus learning from nature is may be the best way to design nano-structures with

desired properties.

Extending the previous chapter on wettability of rough hydrophilic surfaces [72], in the present chapter we have designed a model system consisting of linear protrusions having hydrophobic and hydrophilic blocks. We have added the water molecules on top of the hydrophilic blocks, and investigated the structuring of water molecules near these linear atomistic protrusions for a wide range of temperatures and pressures. The model system studied here, with hydrophobic and hydrophilic blocks, and water on top of the hydrophilic blocks, is motivated from lipid bilayer-water like systems structurally, where the solute due to the presence of hydophilic head groups and hydrophobic tails self assembles as a lamella with its hydrophilic groups pointing towards water. Model systems having structural resemblance with a real system may prove to be a guide for designing smart materials. However, in the present thesis we have not drawn any comparison between the model nano-structure and any real lipid bilayer like systems. The protrusions are constructed of LJ particles. Hydrophilicity and hydrophobicity of the protrusions are controlled by controlling the σ and ϵ of the LJ-particles forming the protrusions (see Computational Methods). We have studied the local structuring, ordering and energetics of water at various positions near to the model atomistic protrusions at different temperatures and pressures keeping the position of the protrusions fixed. Temperature is varied from 290K to 200K in steps, and starting from 270 K, pressure is varied from 1 bar to 200 bar. Such variation in temperature and pressure is performed to understand the effect of high pressure, and low temperature on the structuring and retention properties of water near the model nano-structure presented in this chapter. We have shown in chapter 4, that wettability of rough hydrophilic surfaces can vary depending upon its roughness, and surface-water non-bonded potential energy[72]. Systematic study of such model systems and

further implementation of these in experimental synthesis of nano-structures would help in preparing new smart materials with tunable water retention and ordering.

5.2 Computational Method

5.2.1 The Model

The structure of the protrusion is constructed as linear with one hydrophobic and one hydrophilic block (Figure 5.1). The hydrophobic block contains only one kind of particle (Hb). But, the hydrophilic block contains two kinds of particles (Hln and Hlp). The hydrophobic Hb-particles do not bear any charges.

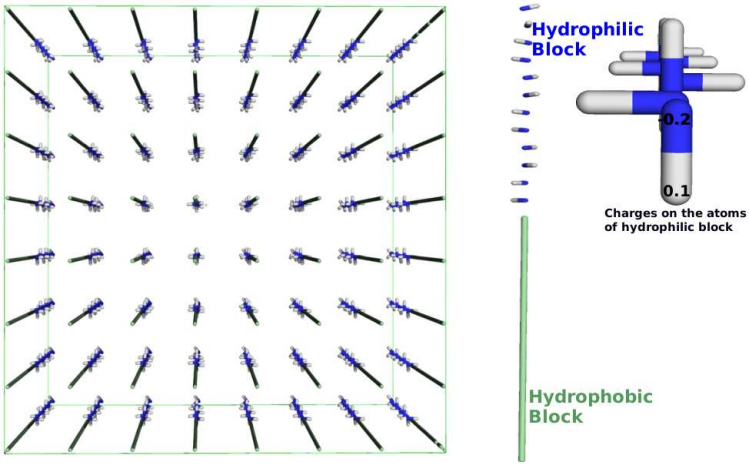

Figure 5.1: The model protruded system. Individial protrusions contain one hydrophilic (blue), and one hydrophobic block (green). Hydrophobic block contains Hb-type particles (green), and hydrophilic block contains negatively charged Hln (blue) and positively charged Hlp (white) type particles. Hlp-type particles point out radially in space from protrusion. Protrusions are multiplied in the XY-plane.

Hydrophobic Hb-type particles are joined one over other along the Z-axis to construct the hydrophobic block. This is followed by the hydrophilic Hln-type particles in the same direction to form the hydrophilic block. This, as a whole, gives a linear

protruded structure (Figure 5.1). In addition to this, one Hlp-type particle is attached to each of the Hln-type particles in the hydrophilic block. The Hlp-type particles are arranged in the coordinate space such that they radially point outwards from the hydrophilic block (Figure 5.1). This may enhance ordering of water molecules because of its inherent symmetry around the protrusions. Each of the Hlp-type (hydrophilic positively charged) particles bear a charge of +0.1 and alternate Hln-type (hydrophilic negatively charged) particles bear -0.2 (Figure 5.1). This makes each of the protruded structure neutral as a whole. Finally, the protrusions were arranged along the XY-plane (8×8) to give 64-protrusions in total (Figure 5.1). A distance of 0.8 nm has been maintained between the protrusions in the starting structure throughout the XY-plane.

The model system contains distinct hydrophobic and hydrophilic regions along the Z-direction made up of the hydrophobic and hydrophilic blocks present in each of the individual protrusions. The hydrophobicity or hydrophilicity of individual particles are maintained by tuning the Lennard-Jones (LJ) interaction parameters, i.e., σ and ϵ for each type of particle. The σ and ϵ values for Hb and Hln-type particles were considered by comparing force field parameters (non-bonded LJ) of different types of atoms (hydrophobic and hydrophilic) and finally by plotting inter-particle LJ potentials, which is,

$$V_{ij} = 4\epsilon_{ij}\left[\left(\frac{\sigma_{ij}}{r_{ij}}\right)^{12} - \left(\frac{\sigma_{ij}}{r_{ij}}\right)^{6}\right] \tag{5.1}$$

where r_{ij} is the distance between i and j^{th} particle.

Non-bonded interactions i.e. LJ potentials between Hb and Hln with oxygen (O) of water are shown in Figure 5.2. Here r_{ij} is the distance between water O and

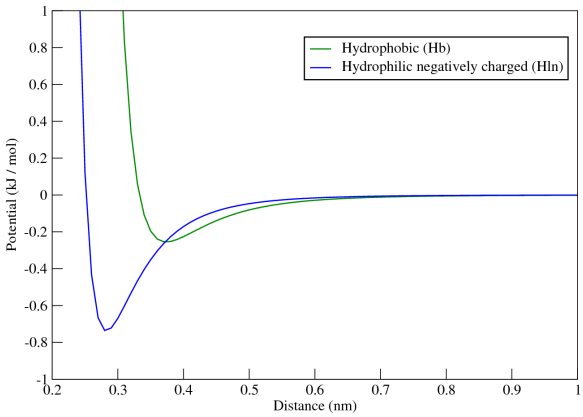

Figure 5.2: LJ potential plot between Hb and Hln-type particles, and oxygen of SPC/E water.

Table 5.1: List of the nonbonded parameters used for the protrusions and water.

Particle	σ (nm)	ϵ (kJ/mol)	q (e)
Hb	0.35	0.1	0.0
Hln	0.2	0.8368	-0.2
Hlp	0.0	0.0	0.1
Water O	0.3165	0.6501	-0.8476
Water H	0.0	0.0	0.4238

the particle (Hln or Hlp), and σ_{ij} and ϵ_{ij} are determined by the combination rules $\sigma_{ij} = \sqrt{\sigma_{i(watO)}\sigma_{j(Hlb/Hln)}}$, and $\epsilon_{ij} = \sqrt{\epsilon_{i(watO)}\epsilon_{j(Hlb/Hln)}}$. It is evident from Figure 5.2 that the LJ-potentials for the hydrophobic and the hydrophilic particles differ in both σ and ϵ. Much lower values of σ and ϵ for the hydrophilic Hln-type particles makes their interaction with water more favorable than the hydrophobic Hb-type particles. The LJ-parameters used in the present chapter are listed in Table 5.1. σ and ϵ for the Hlp-type particles are 0, but they bear a positive charge (Table 5.1). Charges on other particles forming the protrusions are also listed in Table 5.1. In addition to this, σ, ϵ, and charges of the SPC/E water model [73] are also given in Table 5.1.

Protrusion–protrusion, water–water, and water–protrusion non-bonded interac-

tions were taken care of using the following relation

$$V_{nonbonded} = V_{LJ} + V_{coulomb} \tag{5.2}$$

where $V_{coulomb}$ is the Coulomb interaction potential.

Water was added on the top of hydrophilic region of the protrusions in the initial structure (Figure 5.3), such that, protrusion-water interface was created along the Z-axis. Positions of all the protrusion particles were restrained during the simulations. Water, being free to move, enters inside the hydrophilic region.

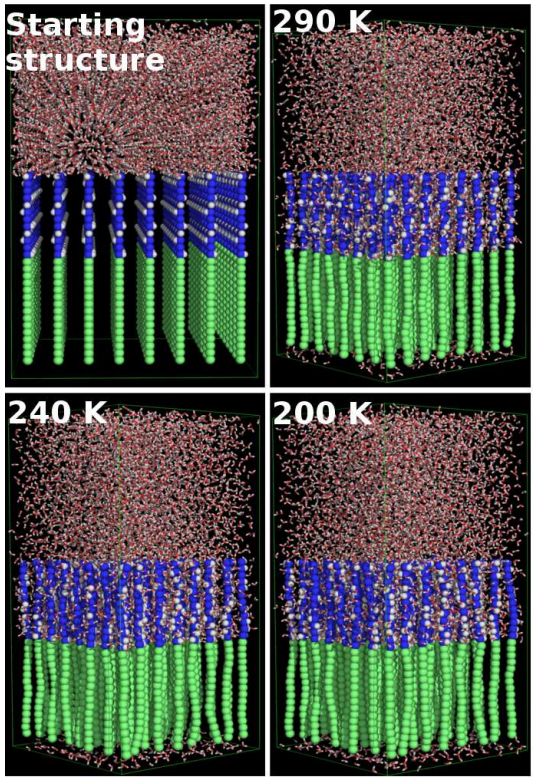

Figure 5.3: Snapshots of the system at different temperatures and 1 bar.

5.2.2 Details of Simulations

All the simulations were performed using gromacs-4.5.5 package [43]. For both LJ and coulombic interactions cut off distance of 1.0 nm was applied. Long range electrostatic interactions were treated with particle mesh Ewald (PME) method[22, 74]. The initial system (Figure 5.3) was allowed to equilibrate at 290 K and 1 bar for 10 ns. Then a production run of 10 ns was performed and analyzed further. Finally, the temperature was decreased slowly in steps of 10 K upto 200 K by taking the output structure at each temperature as an input for the next lower temperature. 20 ns simulations were performed at each temperature. We have checked the average potential energy in different regions of the system as a function of time (discussed in section 5.3.2) to confirm that the system is equilibrated. The protrusions were position restrained, as implemented in gromacs-4.5.5, in all the simulations. This process of cooling allowed the water molecules to penetrate more inside the hydrophilic region. In addition to this, 20 ns simulations were also performed at higher pressures from 270 to 200 K temperatures. Simulations were performed at 1, 200, 100, and 1000 bar pressures. 1000 bar pressure was studied to check the effect of such high pressure on structure and dynamics of water molecules. All the simulations were performed using isothermal-isobaric (NPT) ensemble. V-rescale thermostat [35] and Berendsen barostat[38] was used to keep the temperature and pressure constant respectively. Semi-isotropic pressure coupling in XY- and Z-directions and periodic boundary condition (PBC) were applied in all the simulations.

5.3 Results

Water-protrusion interface was created along Z-axis in the initial structure (Figure 5.3), and water was allowed to interact with the protrusions. No water molecules were present inside any regions of the protrusions in the initial structure. During the equilibration at 290 K and 1 bar water enters inside the hydrophilic region of the protrusions (Figure 5.3). Further, as the temperature is decreased at 1 bar water molecules move deeper inside the hydrophilic region, upto the starting of hydrophobic region (Figure 5.3). Protrusions, being position restrained in all the simulations i.e., fluctuates around mean positions, the hydrophilic and hydrophobic regions are well defined in all the simulations. Further, to quantitatively understand upto what point water enters inside the hydrophilic region, partial density of water along Z-axis (direction of protrusion-water interface) is calculated and shown in Figure 5.4. At a particular temperature partial density of water is shown for different pressures (Figure 5.4). Since the position of protrusions are fixed in all the simulations, only one partial density is shown for them. The partial densities for hydrophilic, and hydrophobic regions are shown distinctly. At a particular temperature, water enters more deeper inside the protrusions as the pressure is increased. At 270 K and 1 bar water penetrates upto the junction of hydrophobic and hydrophilic regions, but at 1000 bar the water molecules seem to move inside the starting of the hydrophobic region. This level of penetration upto the hydrophobic region keep increasing gradually on moving from 1 bar to 1000 bar. Similar gradual increase can be observed at 230, and 200 K also. At all these temperatures and pressures water molecules are wetting the hydrophilic region because of choice of attractive LJ potentials and electrostatic interaction. These interactions are further quantified in section 5.3.2.

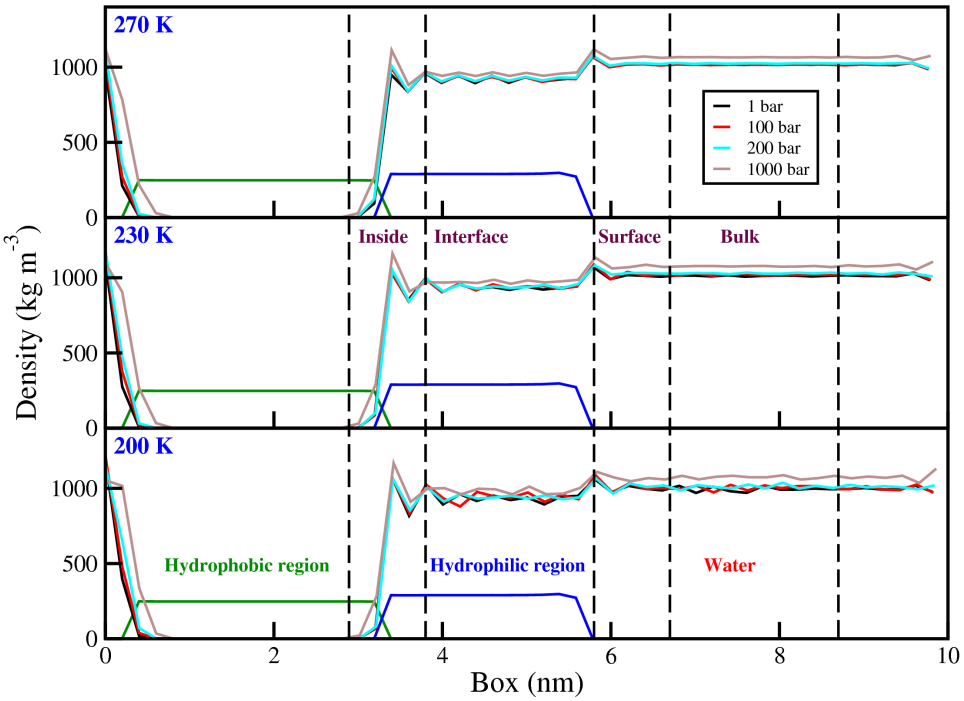

Figure 5.4: Partial density of water and protrusions along Z-axis (axis perpendicular to the protrusion-water interface). Different regions are defined depending upon density of water.

Few water molecules are present near the end hydrophobic region (Hb-type) i.e., near 0-1 nm due to periodic boundary condition along Z-axis.

Depending upon density of water we have defined four regions along the Z-axis: inside (2.8–3.8 nm), interface (3.8–5.8 nm), surface (5.8–6.7 nm), and bulk (6.7–8.7 nm). In the inside region, water is closest to the hydrophobic region of protrusions and water density keeps on increasing and almost touches 1000 kg m^{-3} in this region. The region starting from the end of the inside region and ending at the end of hydrophilic region has been defined as the interface region. The density of water fluctuates around 1000 kg m^{-3}. Further, a small block just above the hydrophilic protrusions where the density of water continues to fluctuate is defined as the surface region. Water molecules in this region are closest to the protruded hydrophilic

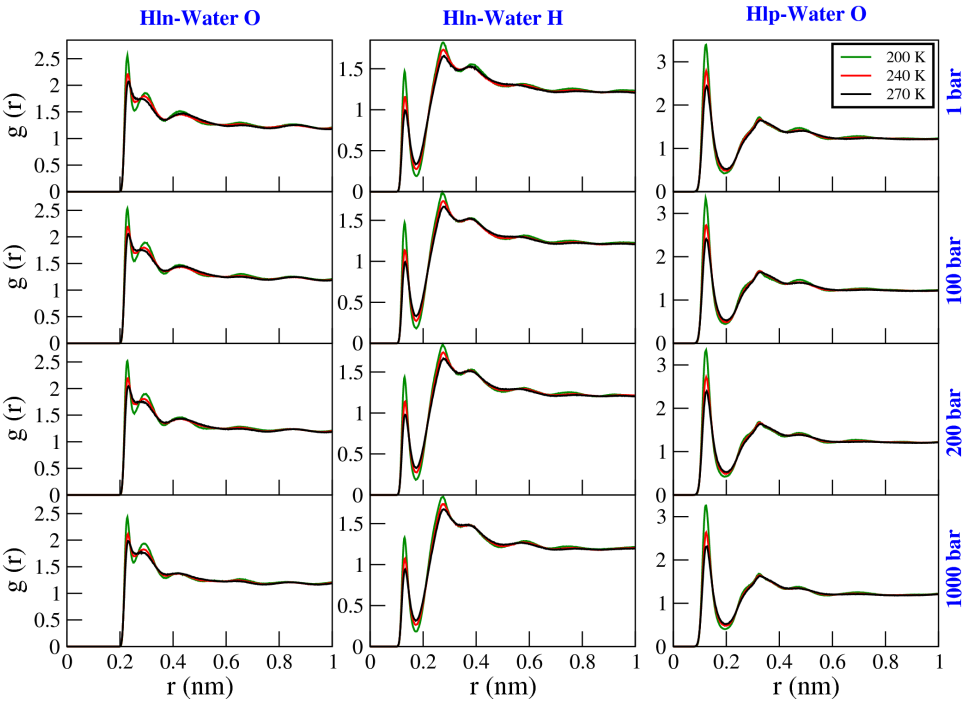

Figure 5.5: RDF between water and different particles of protrusions.

surface. Fluctuations in water density and structuring of water molecules near hydrophobic surfaces, and have been studied in the past[75–77]. Thus it is interesting to understand such phenomenon near the hydrophilic surface formed by the hydrophilic region of the protrusions. Finally, the region with almost same density (less fluctuation) is defined as the bulk. We have analyzed and distinguished the differences in structuring and energetics of water in these regions separately.

5.3.1 Ordering of Water Molecules

Ordering of Water Molecules Near Protrusions

Water molecules penetrate the hydrophilic region because of favourable interaction potential. The Hlp particles point radially outward from the hydrophilic region of the

protrusions. This may support the ordering of water molecules near the protrusions. Radial distribution function (RDF) plots are shown in Figure 5.5 at different temperatures at a particular pressure to understand the ordering of water molecules around Hln and Hlp-type particles present in the hydrophilic region of protrusions. The peak heights of all the RDF plots increase with decrease in temperature at one pressure. This indicates more ordering of water molecules near the Hln and Hlp-type particles with decrease in temperature. For all the RDFs between particle Hln and water O a sharp first peak at 0.23 nm is present at all the temperatures and pressures. A second peak gradually forms with decrease in temperature at a particular pressure. This indicates that though the water molecules order near the Hln-type particles, the ordering is translated further in the second solvation shell with decrease in temperature. This is more evident from the RDFs between particle Hln and water H. There are two distinct peaks at all temperatures and pressures indicative of two solvation shells and the peak heights of both the peaks increase with decrease in temperature. This shows increase in ordering of water molecules in both the solvation shells with decrease in temperature. The first peak height, corresponding to first solvation shell, in the RDF between particle Hlp and water O also increases with decrease in temperature at all pressures. Though there is not much change in the second peak.

Further, to construe the overall picture of ordering of water molecules near the protrusions, distribution of angles between water O, Hln-type particle, and water O (O-Hln-O) is calculated and shown in Figure 5.6. For calculating these distributions, first, all the water molecules falling within a distance of 0.4 nm (corresponding to minima of second peak of particle Hln-water O RDF in Figure 5.5) from the Hln-type particles, which have more than two water molecules as its neighbour, were identified. Then, the O-Hln-O angle was computed for all such water molecules, and the angles

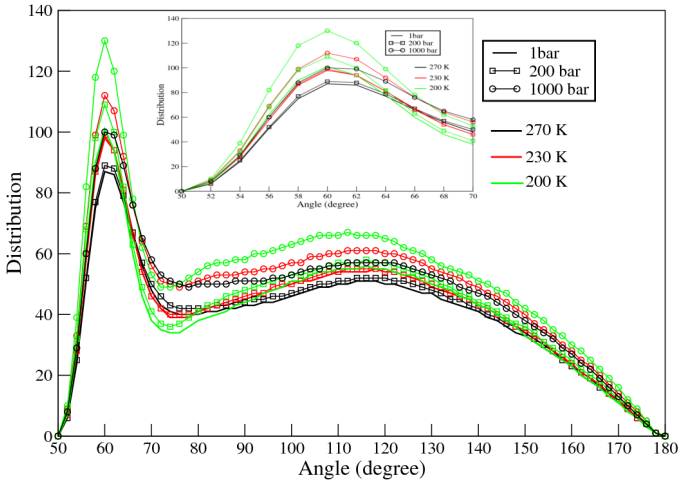

Figure 5.6: Distribution of the angle between water O, particle Hln, and water O. The first peak is focussed in the inset.

were converted into a histogram. Finally, the distributions were plotted for all sets of simulations and normalized over the number of frames present in the last 2 ns of the trajectories. Two distinct peaks can be observed at all the temperatures and pressures (Figure 5.6). The second peak is comparatively broader than the first. At a particular temperature, peak heights increases with increase in pressure. Not much difference in peak height is observed for 1 bar and 200 bar pressures at a particular temperature, but at 1000 bar peak height is the highest (first peaks are zoomed in the inset of Figure 5.6). Also, peak height increases on decreasing temperature. This is in correspondence with the peak heights of RDF plots, and indicate higher ordering at lower temperatures. The first peak near 60° suggests that a particular orientation of water molecules near the protrusions is favoured. Broad second peak of O-Hln-O angle distribution may have been caused by the water molecules residing in the second solvation shell. Ordering of water molecules present in the second solvation shell experience less attraction from Hln and Hlp-type particles because of shielding by the first solvation shell as well as water-water interactions may get favoured. However,

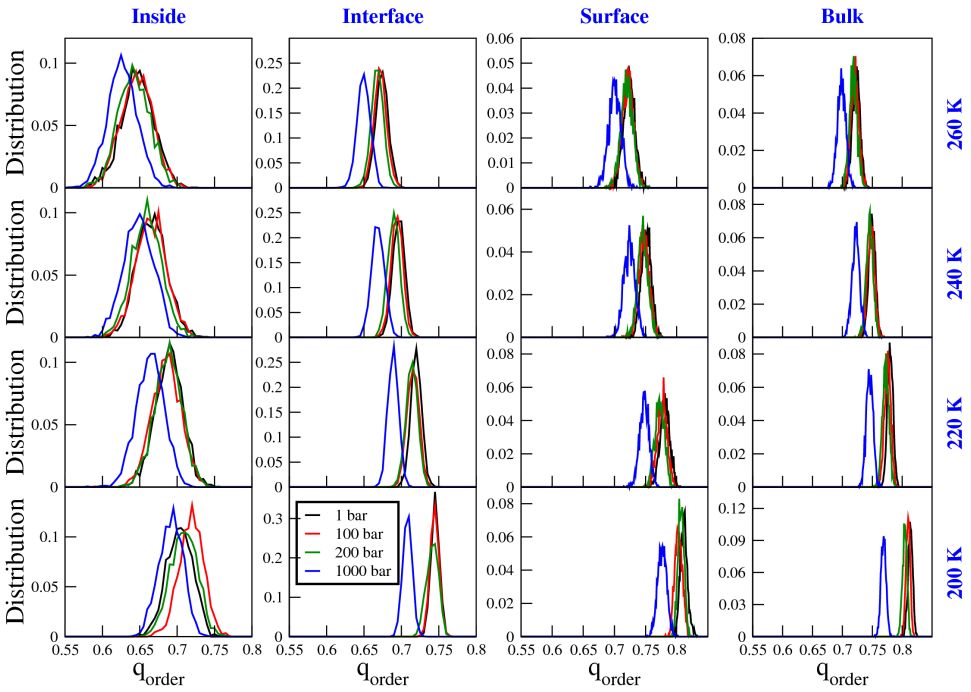

Figure 5.7: Distribution of order parameters calculated for different regions at different temperatures and pressures.

water molecules inside the hydrophilic region experience interaction from Hln and Hlp-type particles and favours ordering near to the nearest protrusions.

Water–Water Ordering

In addition to ordering of water molecules involving the particles of protrusions at the interface region, it is also important to investigate the structuring of water molecules at the surface and bulk region due to the presence of protrusions. Orientational order parameter [78] (q_{order}) is calculated to understand such water-water ordering. It is defined as

$$q_{order} = 1 - \frac{3}{8}\sum_{i=1}^{3}\sum_{j=i+1}^{4}\left(\cos\theta_{ij} + \frac{1}{3}\right)^2 \tag{5.3}$$

where θ_{ij} is the angle between the vectors joining the oxygen atom of one water molecule and oxygen atom of its nearest neighbour water molecules i and $j(\leq 4)$. Distribution of q_{order} at different pressures at particular temperature is shown in Figure 5.7. q_{order} signifies the extent by which four nearest neighbours assemble in a tetrahedral configuration [78]. For a perfect tetrahedral arrangement $q_{order} = 1$, and $q_{order} = 0$ for random arrangement. q_{order} has been calculated in the past for water molecules confined inside hydrophobic, hydrophilic, and heterogeneous plates by Giovambattista et al [79]. Thus, calculation of q_{order} is relevant to understand the water-water ordering in different regions defined in Figure 5.4. q_{order} per water was calculated first for each region separately and converted into histogram. Finally, distributions are plotted normalizing over total number of frames in last 2 ns for all the trajectories (Figure 5.7).

The peaks of the distributions can clearly be seen to be shifting towards higher q_{order} value with decrease in temperature (Figure 5.7). Higher q_{order} value indicates higher tetrahedral ordering, so it is somehow obvious that water molecules are more tetrahedrally ordered at low temperatures. For a temperature q_{order} is lower for 1000 bar with respect to 1, 100, and 200 bar pressures. Although, even at 1000 bar q_{order} increases on lowering the temperature.

Distributions of q_{order} for inside region is broader than interface, surface, and bulk. This fact is evident from the the q_{order} distributions shown in Figure 5.8 at 1 bar and different temperatures. It suggests that at a temperature the q_{order} value varies as inside <interface <surface $\simeq$ bulk. This is because, in the inside region water molecules are nearest to the hydrophobic Hb-type particles. Due to the unfavourable interactions with the Hb-particles inside region water molecules deviate more from tetrahedral arrangement (lower q_{order} value). Also, plot of average θ_{ij} as function of

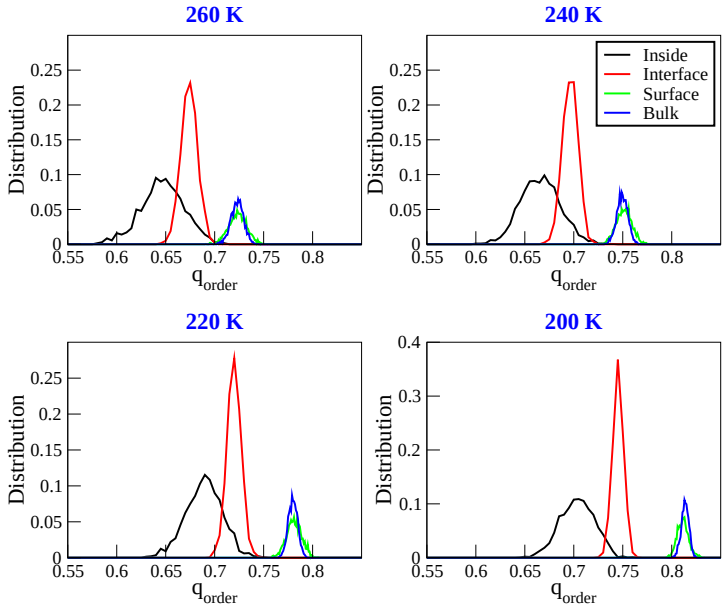

Figure 5.8: Distribution of q_{order} at 1 bar and different temperature. It indicates that at a particular temperature and pressure the value of q_{order} varies as inside <interface <surface $\simeq$ bulk.

time given in Figure 5.9 shows higher fluctuation for inside region. This accounts for the broadness of the q_{order} plot for inside region (Figure 5.7 and 5.8). From the RDF (Figure 5.5) and angle distribution (Figure 5.6) we have seen that water molecules are ordered near the protrusion and the interactions between protrusion particles and water molecules may facilitate the departure from tetrahedral ordering. Water molecules present in the interface region are nearest to the Hln- and Hlp-type particles. But at the same time they feel the unfavourable hydrophobic interactions of Hb-type particles. As a result, distribution of q_{order} for the interface region appear at higher value than inside region (Figure 5.7 and 5.8). The nonbonded interactions are quantified in section 5.3.2. Surface region water molecules are closest to surface formed by the hydrophilic particles of the protrusions. They face least unfavourable hydrophobic interactions with the Hb-type particles as they are farther, and also due

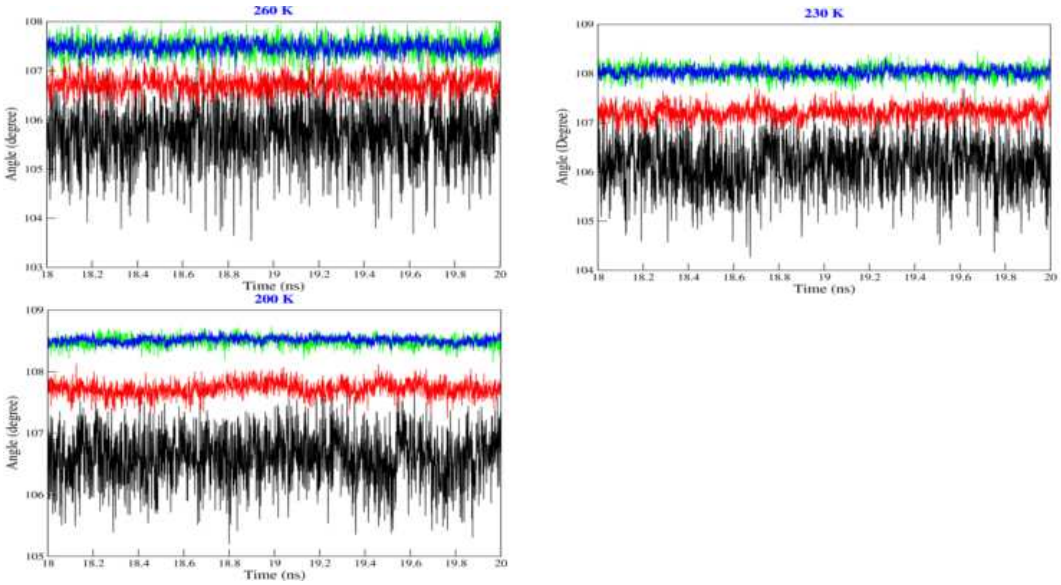

Figure 5.9: θ_{ij} in q_{order} as a funtion of time for different temperatures and 1 bar pressure.

to screening by the inside and interface region water molecules. Higher ordering in the surface region accounts for the fluctuations in density observed (Figure 5.4).

5.3.2 Energy Profiles for Different Regions

Higher ordering can also be related to favourable potential energy. Therefore, it is important to check whether the tetrahedrally ordered surface or ordered (but less tetrahedrally) interface water molecules are at the lower potential energy than other regions. Therefore total non-bonded interactions per water molecule is computed and plotted for each region in Figure 5.10. It represents the average total non-bonded potential felt by individual water molecules present in a particular region. The non-bonded interactions experienced by each water molecule present in any region are sum of van der Waals and Coulombic interaction among water molecules, and between water protrusions particles. The total non-bonded interaction potential energy is

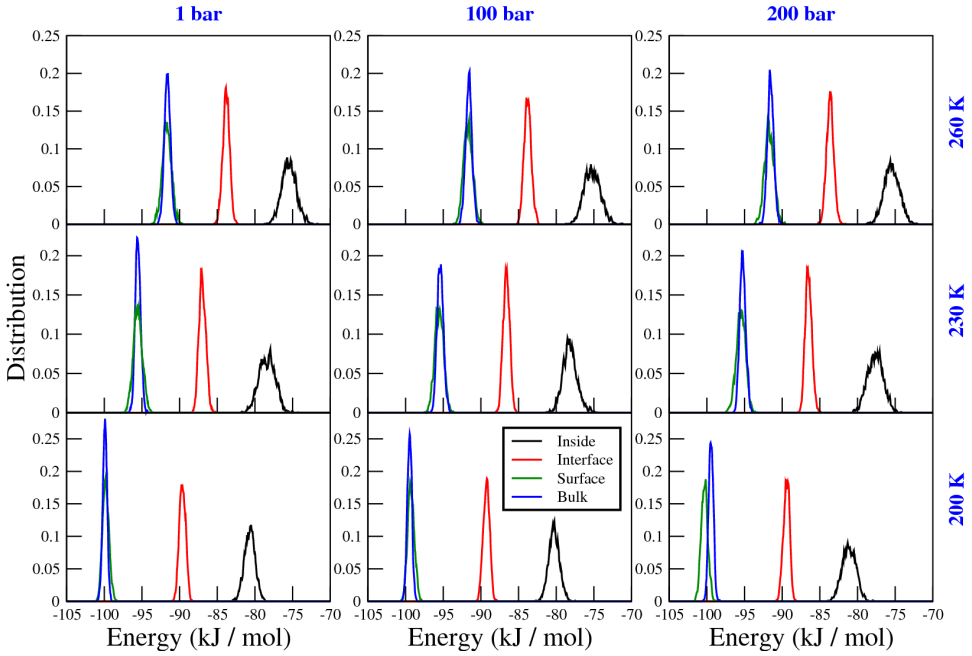

Figure 5.10: Distribution of average total non-bonded potential energy.

calculated as the sum of LJ and Coulomb. The LJ potentials were calculated using equation 1 for the pair of particles concerned. Coulombic potentials were computed as $q_i q_j / 4\pi\epsilon_\circ r_{ij}$, where q_i and q_j are the charges on the concerned atoms and r_{ij} is the distance between them, and $\epsilon_\circ$ is the permittivity of vacuum. The term ϵ_r (permittivity of the medium) was taken as 1 in all the simulations. The term $1/4\pi\epsilon_\circ$ is equal to 138.935485 kJ mol^{-1} nm e^{-2}. Though we have used PME electrostatics in all our simulation, calculation of coulombic interactions in this way gives the exact electrostatic potential experienced by each water molecule present in a region. The water molecules present in each region (see Figure 5.4) were tagged in each frame. The sum of LJ and Coulombic potentials was computed for each water molecule in all the regions separately due to all the other particles present in the system for each frame and averaged over the number of water molecules corresponding to each region separately. This gave the average non-bonded potential energy per water molecule in

each frame for different regions separately. These non-bonded energies as a function of time is provided in Figure 5.11 for last 2 ns of trajectory. Finally, the average non-

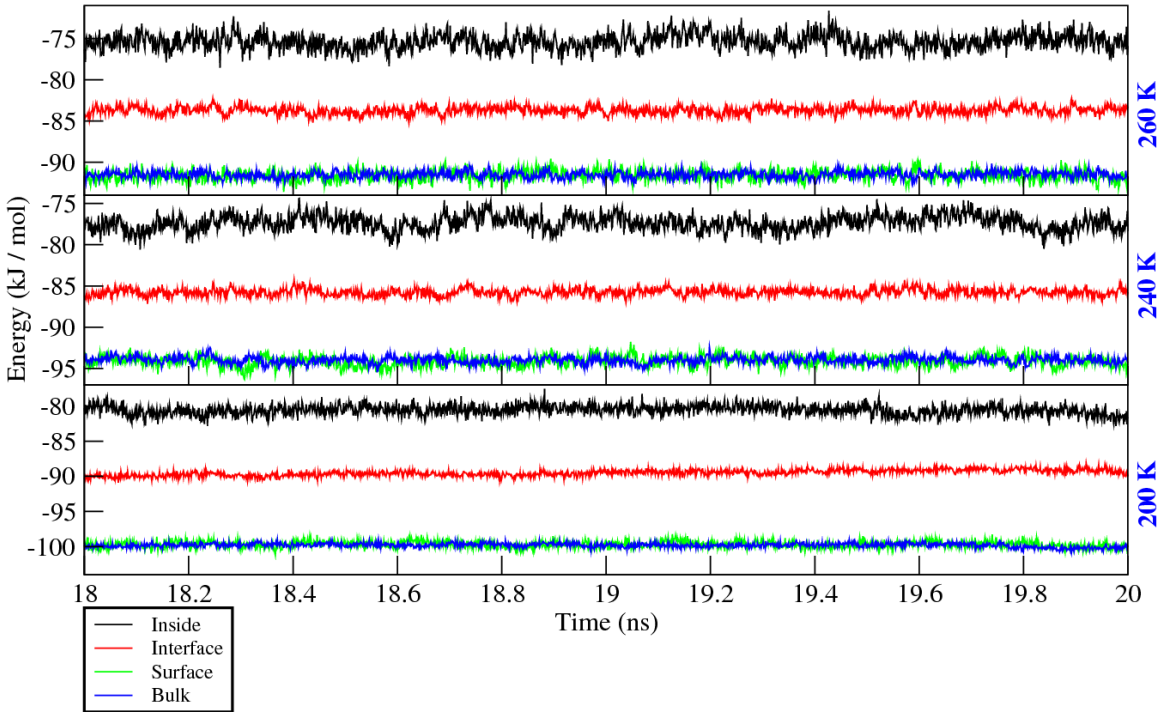

Figure 5.11: Plot of average nonbonded potential energy per water molecule as a function of time for different temperatures and 1 bar pressure.

bonded potential energy per water molecule was converted into a histogram which is further normalized by the number of frames in last 2 ns (see Figure 5.10). It is evident from the plots that at almost all the temperatures and pressures the value of average non-bonded potential energy per water molecule is the least for the surface and bulk regions, and the most for the inside region. The water molecules of the inside region are closest to the hydrophobic region and contribute to repulsive interaction. But the water molecules present in the surface region are interacting more with the particles of the hydrophilic region and less with hydrophobic particles, which in total promotes attractive interaction. This is consistent with the order of q_{order} parameters for the

different regions see Figure 5.7, and Figure 5.8). That is higher ordered region shows lower potential energy.

The water molecules at the surface region are experiencing the attractive hydrophilic interactions due to the protrusion particles and at the same time gaining stability by tetrahedral ordering. As a function of temperature the change in position of peaks (Figure 5.10) is noticeable. This is more evident from the plot of peak height of potential energy distribution at different temperatures (Figure 5.12). Potential energy can be clearly seen to be decreasing with decrease in temperature. This drop is also visible with variation in pressure.

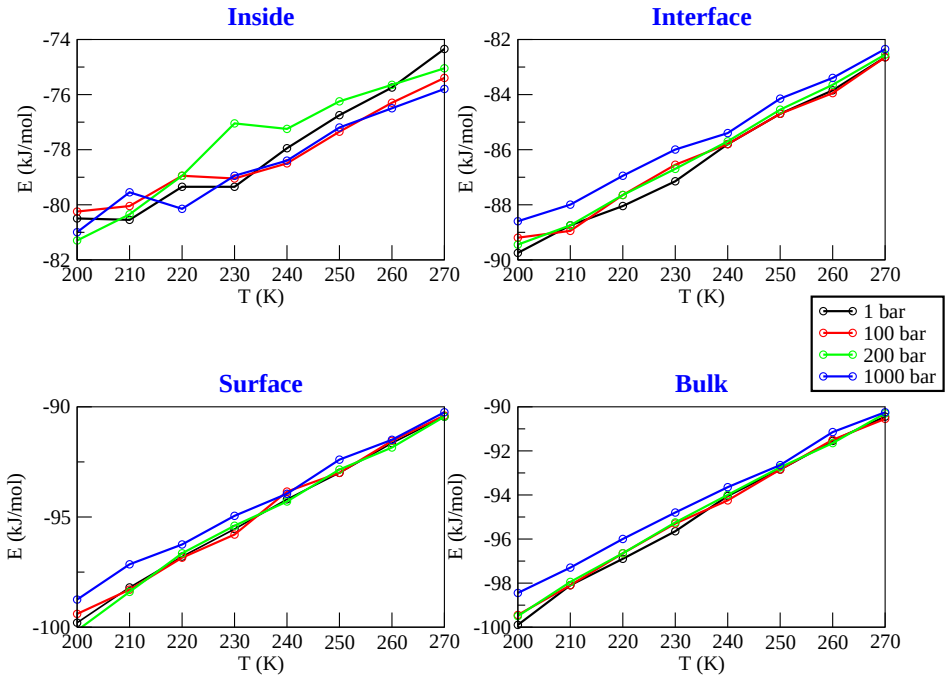

Figure 5.12: Peak height of potential energy distribution as a function of temperature at different pressures.

5.3.3 Residence Time

Survival probability of water molecules present in different layers of lipid bilayer-water system was calculated in the past by Debnath et al. [80]. They represented the probability of a water molecule to stay in a layer for certain duration of time. In our system we have distinct regions and observed differences in potential energy experienced by water molecules at different regions (see Figure 5.10). Thus residence time of water molecules in different regions can provide useful information about the favourable regions for water molecules to stay longer which eventually can be correlated to the probability of water retention. The residence time distribution, i.e., duration upto which a water molecule resides in a particular region (Figure 5.4), is calculated and its distribution is shown in Figure 5.13 i.e., the time is plotted with respect to its occurrence (Figure 5.13). All the simulations were extended for 1 ns because of expected longer residence time and the coordinates of all the atoms were saved every 10 fs (referred as condensed trajectory) for this calculation.

For calculating the time of continuous stay, each region defined in Figure 5.4 is further divided into small slabs of width 0.35 nm (the minima of first peak of O-O RDF of water comes near 0.32 nm) along z-axis. Then, the water molecules present in these slabs were identified in each frame of the condensed 1 ns trajectories. 0.32 nm of slab width was considered along with a soft boundary of 2 ps time for the calculation. This implementation of the soft boundary (as time) to make sure that, if a water molecules move out from a slab and again comes back to the same slab within 2 ps, we considered it to be present in that slab continuously[11]. This is because in 2 ps water molecules can not drift away to a large distance from the slab which makes the boundaries of the slabs much coarser. The soft boundary was also used by Impey

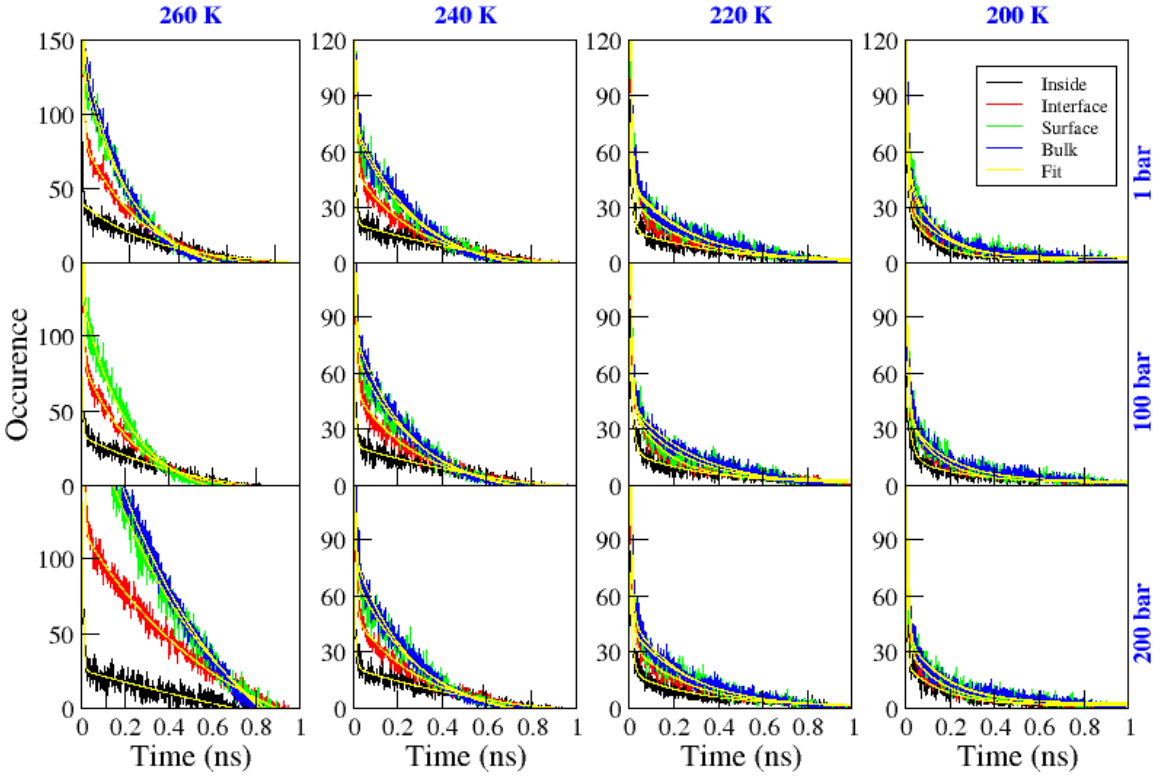

Figure 5.13: Residence time distribution for water molecules in different regions, and fitting of residence time with bi-exponential function.

et al. [81] to calculate the residence time of water molecules in the first solvation shell of ions. Finally, the occurrence as a function of time is depicted in Figure 5.13 for all temperatures and pressures. The occurrences are represented for different regions (Figure 5.4) separately, and are averaged over all the slabs of a certain region.

The residence time distribution for bulk and surface region at high temperatures (260 K) and low pressures (1 bar) is almost same. However at all temperatures and pressures the residence time distribution decays faster in the interface and inside regions than surface region indicating fast and slow dynamical motions of water

molecules. Lower residence time for inside region water molecules may attributed to the hydrophobic repulsion from the hydrophobic particles which drives out the water molecules towards the interface region, and there is a fast exchange happening between these two regions. Additionally, the interface region is energetically favourable (refer Figure 5.10) as compared to inside region, which supports the longer stay of water molecules in this region hence the longer residence time distribution with respect to inside region. Also, water molecules in the surface region are more tetrahedrally oriented than the inside and interface region water molecules (Figure 5.7 and 5.8). This contributes to the higher residence time for water molecules present in surface region as compared to inside and interface regions. Because higher ordering implies hopping motion of water between different sites which may result into lesser exchange with other regions. Thus there might be a competition between ordering and energetics to guide the residence time of water. At 260 K, residence time is more for the inside region than the surface region. Here, energetics guides the ordering. But, as the temperature is lowered ordering starts to guide the residence time. That is why at 200 K surface region water molecules have higher residence time than that of inside region.

Further, the residence time plots (Figure 5.13) were fitted with a bi-exponential function of the form

$$y = a_f exp(-\frac{t}{\tau_f}) + a_s exp(-\frac{t}{\tau_s}) + a_0 \tag{5.4}$$

where τ_f and τ_s are the fast and slow relaxation times respectively, and a_f and a_s are the respective amplitudes[11, 80]. The fitted plots for different regions at different temperatures and pressures are provided in Figure 5.13. Higher value of τ_f or τ_s

represent slower relaxation and hence slower dynamics. Table containing values of τ_f, τ_s, a_f and a_s for different regions at different temperature and pressure are provided in Table 5.2. The values are higher as compared to the values reported in references [80] and [11] as the temperatures at which residence times are calculated are lower in the present study. Also the definition of the regions to calculate the survival probability are different. They are computed with respect to their motion along z-axis in different regions. The lateral motion is not accounted for as motion of water molecules in xy-plane does not change the region (Figure 5.4). τ_f is lower for the surface region as compared to the inside and interface regions (Table 5.2) for all regions at all temperatures and pressures. This indicates that the fast decaying component is lower for surface region.

Table 5.2: Components of bi-exponential fitting of residence time distribution at different temperatures and pressures.

		Inside					**Interface**		
260K	a_s	τ_s **(ns)**	a_s	τ_s**(ns)**	**260K**	a_s	τ_s **(ns)**	a_s	τ_s**(ns)**
1 bar	45.5469	0.5736	91.6534	0.004318	**1 bar**	89.4762	0.2385	225.464	0.005286
100 bar	45.3208	0.573	85.588	0.004546	**100 bar**	89.1516	0.2360	226.788	0.005337
200 bar	103.621	2.478	222.344	0.005158	**200 bar**	162.071	0.6702	418.232	0.006191
240K					**240K**				
1 bar	36.1919	0.9703	84.6565	0.007076	**1 bar**	52.4022	0.2791	192.458	0.007444
100 bar	33.962	0.9169	77.9956	0.007141	**100 bar**	53.3352	0.2705	184.014	0.007580
200 bar	33.2244	0.8365	78.5308	0.007506	**200 bar**	52.1139	0.2938	178.069	0.00720
220K					**220K**				
1 bar	18.6233	0.5007	61.7121	0.01247	**1 bar**	33.483	0.2394	163.719	0.009469
100 bar	16.9514	0.3560	64.9655	0.01443	**100 bar**	38.1451	0.1719	150.357	0.008678
200 bar	17.3841	0.3603	56.745	0.01369	**200 bar**	34.0236	0.2490	141	0.00928
200K					**200K**				
1 bar	28.5703	0.1240	81.3607	0.007949	**1 bar**	30.5753	0.1865	112.991	0.009711
100 bar	13.6863	0.2501	42.2989	0.02141	**100 bar**	36.8842	0.1423	118.033	0.00824
200 bar	21.8807	0.1745	77.3748	0.005857	**200 bar**	30.5296	0.1674	110.773	0.009760
		Surface					**Bulk**		
260K	a_s	τ_s **(ns)**	a_s	τ_s**(ns)**	**260K**	a_s	τ_s **(ns)**	a_s	τ_s**(ns)**
1 bar	140.074	0.2062	283.761	0.003798	**1 bar**	155.676	0.1814	284.609	0.003581
100 bar	135.374	0.2166	272.392	0.004393	**100 bar**	153.632	0.1867	276.208	0.003420
200 bar	272.698	0.5634	512.935	0.004305	**200 bar**	307.295	0.5681	495.405	0.004230
240K					**240K**				
1 bar	77.8862	0.2712	213.621	0.00582	**1 bar**	83.4287	0.2871	252.992	0.005916
100 bar	77.8739	0.2811	230.353	0.006424	**100 bar**	87.8087	0.2508	226.523	0.006104
200 bar	78.5998	0.2927	238.374	0.005538	**200 bar**	88.347	0.2582	251.074	0.005069
220K					**220K**				
1 bar	42.3192	0.2620	190.485	0.007690	**1 bar**	43.5488	0.2756	193.799	0.008254
100 bar	39.636	0.2371	162.412	0.009729	**100 bar**	44.5122	0.2838	196.185	0.00811
200 bar	42.8219	0.285	194.775	0.007021	**200 bar**	47.8152	0.2464	170.044	0.008678
200K					**200K**				
1 bar	51.3495	0.1148	130.027	0.006577	**1 bar**	42.2377	0.1468	133.635	0.008365
100 bar	34.6056	0.1830	122.683	0.01069	**100 bar**	35.2742	0.1850	122.917	0.01055
200 bar	36.2709	0.1789	118.605	0.009263	**200 bar**	35.6283	0.1867	155.314	0.009083

5.4 Conclusion

The model nano-structure studied here favours structuring and retention of water molecules. The LJ particles constructing the protrusions are defined with respect to their interaction with the SPC/E water. The parameters defined are good enough to

allow water molecules to penetrate inside the hydrophilic region. The main advantage of the model is the penetration of water molecules can be enhanced just by tuning the parameters of the protrusions. The main limitation of the model is the protrusions are position restrained so the high flexibility of the surface atoms are not considered. This may lead to some amount of discrepancies in the results.

In chapter 4, the effect of roughness, and non-bonded interaction parameters on wetting of hydrophilic surfaces are discussed[72]. In the present chapter, we have diversified the model system to understand the effect of both hydrophobic, and hydrophilic particles on structural and dynamical properties of water. The knowledge gained from these model systems can be helpful in designing smart materials that can retain water inside them. The residence time of water molecules is atleast 100 ps in any region at different temperature and pressure (Figure 5.13). Such retention can also be acheived for solvents other than water by just tuning the parameters of protrusions. Also, the residence time of water molecules can be further increased by increasing the hydrophilicity or decreasing hydrophobicity of the particles of protrusions. However, as a model system this is one of the first approach to rationally design such atomic protrusion water interface which can address many fundamental questions related to ordering and retention of water molecules.

In this work MD simulations were performed over a range of temperatures and pressures. Initially, no water molecules were present inside the protrusions. The water molecules penetrate the hydrophilic region of the protrusions. This penetration has been quantified by plotting the partial densities (Figure 5.4) which also helped us designating different regions. We have observed tetrahedral ordering of water molecules in the surface region. Water molecules experience favourable potential energy in the interface region due to the hydrophilic environment. The water molecules at the

surface region are also experiencing favourable potential energy which facilitate the tetrahedral ordering. From the residence time of water molecules it is clear that there are faster and slower motion of water molecules residing in the inside and surface regions due to balance between hydrophobic repulsion from protrusion particles (inside region) and favourable (energetically) interface region.

The ice-water transition (melting) for SPC/E water model has been reported to be taking place near 213 K [82]. In our simulations with the model protrusions, we have not observed any ice formation. Though the ordering of water molecules increase at lower temperatures (Figure 5.7), we did not observe any ice formation. It has been reported in the past that water in its supercooled state can have large value of order parameters, but it does not necessarily mean ice formation [83, 84]. The nucleation and growth of ice involves an energy barrier to be crossed. Also, in the present model system the different LJ particles may favour or hinder the ice nucleation. This is an important issue to be addressed. Because at very low temperatures ice formation in the hydrophilic region of lipid bilayer may rupture it. Also, ice formation inside the hydrophilic grooves can be a challenge for the lyophilization [50] process as it can damage the structure of the material. Thus, understanding the structuring, and growth of ice inside the atomistic model protrusions discussed here would better equip us to deal with the problems in the real systems. But, the main challenge to such study is the nucleation of ice in molecular dynamics time scale.

The model system studied here is the first step in designing smart materials having water retention capability. Being an atomistic model it helps to understand the ordering of water molecules at the structural level. Such a structural level insight can be the basis to understand structuring of water in the real systems. The atomistic model can be further extended to structured models in the future keeping the

hydrophilic, and hydrophobic blocks intact. The parameters can also be tuned to get desired properties. In addition to this, ice formation and growth inside the nano confined region formed by the protrusions can also be studied further.

Construction of the model atomistic protrusions is structurally motivated from lipid bilayer-water interface. Extending the study on model system in the present chapter, we have moved closer to real systems in chapters 8 and 9. We have focussed on phospholipid bilayer-water interface and self assembly of sophorolipids in water in chapters 8 and 9 respectively. Although there exists gradient of hydrophilicity in the head group of phospholipids, the present model system gives a good representation of hydrophilic and hydrophobic environment of lipid bilayer-water interface.

[2]The results and figures are adapted from the publication P. R. Pandey and S. Roy, Model Atomistic Protrusions Favouring Ordering and Retention of Water, Physical Chemistry Chemical Physics, 2014, 16, 15856-15865.

PART-B: Biologically Inspired Systems

Chapter 6

Introduction to Biologically Inspired Systems

In part A, effect of varying roughness and hydrophilicity on wetting and dewetting of model patterned surfaces (chapter 4), and structure and dynamics of water near model protrusions (chapter 5) are elucidated. Extending the study on model systems in part A, here in part B we move closer to real systems. In part B, structure, dynamics and energetics of biologically inspired systems are envisaged in water. However, similar to part A, systems of study vary depending upon degree of hydrophobicity/hydrophilicity. For example, in chapter 7 early stage unwinding mechanism of α-helical peptides varying in side-chain hydrophobicity are investigated in water. In chapter 5 of part A model atomistic protrusions structurally motivated from lipid bilayer-water system are discussed. As an extension of this model system close to real systems, interaction of phospholipid and sophorolipid with water are discussed in chapters 8 and 9 respectively. Although, the systems are different in parts A and B, interface with water is common in all the systems.

Building blocks of proteins are amino acids. Amino acids are classified depending upon the groups present in their side chain. Side chain polarity is a critical factor in interaction of amino acids with water. This, as a whole, affects the three dimensional structure of proteins and their function. Water present in the grooves of certain proteins guide the function of the entire protein [9, 10]. This is also an example of guidance of structure and function depending upon interaction with water. Thus it is important to envisage the interactions of different class of biological systems with varying hydrophobicity and hydrophilicity.

Water is the most abundant solvent in the biological systems. It is the medium for both intracellular and extracellular matrices. Water is necessary for structure and function of biomolecules. Interactions of the hydrophobic/hydrophilic groups present in the biomolecules with water are crucial for their structure and function. Cell membranes are barrier between intracellular and extracellular matrices. They consist of oriented globular proteins and lipids [85]. Lipids, containing hydrophilic head groups and hydrophobic tails, assemble as bilayers in the cell membrane pointing their hydrophilic head groups towards intracellular and extracellular matrix and the hdrophobic tails are packed close to each other. Such bilayer like arrangement is guided by the presence of water in the extracellular and intracellular matrices. This is a classical example of guiding the structure (bilayer) and function (barrier between extra- and intracellular matrices) of a moiety due to the presence of hydrophobic and hydrophilic groups.

In this part of the thesis, structural and dynamical properties of biologically inspired systems in water are studied using MD simulations. Different class of systems are considered such that they differ structurally in the degree of hydrophobic/hydrophilic groups present. Unwinding mechanisms of model α-helical homopoly-

meric peptides in water are discussed. The model peptides are chosen such that they differ in degree of side chain hydrophobicity. Mechanism of water insertion into phospholipid bilayer and self-assembly of sophorolipids in water are studied. Phospholipids and sophorolipids differ in the degree of hydrophobicity/hydrophilicity present in their structure. Phospholipids contain one hydrophilic head group and two hydrophobic tails, whereas sophorolipids contain two hydrophilic head groups and one hydrophobic tail.

Chapter 7 deals with unwinding mechanism of model α-helical homopolymeric peptides in water. Out of all the secondary structures of proteins, α-helix is the most abundant structural form and has crucial importance to understand the unfolding mechanism of proteins. Hence many experimental and theoretical studies have been performed since last two decades to understand the folding and unfolding of α-helical peptides in water. Various choices of peptides have been made for these studies, for example, helical portion of a large protein [86], artificial peptides made up of combination of various amino acids to check their stability [87], peptides assembled with only one kind of amino acids [88, 89], i.e., homopolymers, also peptide composed of β amino acids [90] etc. Each helical turn in an α-helix consist of 3.6 amino acid residues. An α-helix is constructed by hydrogen bonding between carbonyl oxygen (C=O) of i^{th} and hydrogen on amide group (NH) of $i+4^{th}$ residue (Figure 6.1). In water unwinding of helix is achieved by breaking of hydrogen bonds between oxygen of C=O and hygrogen of NH and forming of hydrogen bond with water [91, 92]. In the present thesis unwinding mechanism of zwitterionic, capped and neutral forms of polyalanine, polyleucine, polylysine, and polyglutamic acid helices are studied in water. These helices differ in the degree of side chain hydrophobicity. Details of the different forms and choice of helices are further discussed in detail in Chapter 7.

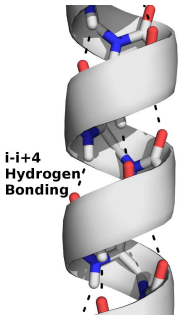

Figure 6.1: Hydrogen bonding betweer C=O of ith and NH of $i+4$th residue in the polypeptide backbone.

Chapter 8 deals with mechanism of water insertion into phospholipid bilayer. As mentioned above, cell membrane consists of oriented globular proteins and lipids. Phospholipids are the major kind of lipid molecules present in the biological systems. Various kinds of phospholipids present in biological system are phosphatidylserine, phosphatidylethanolamine and phosphatidylcholine. They differ in the structure of their hydrophilic head groups. 1,2-dipalmitoyl-sn-phosphocholine (DPPC, Figure 6.2) contains choline group at its head group. Further, it contains two long hydrophobic tails. Structure and dynamics of phospholipids have been studied extensively [93–98].

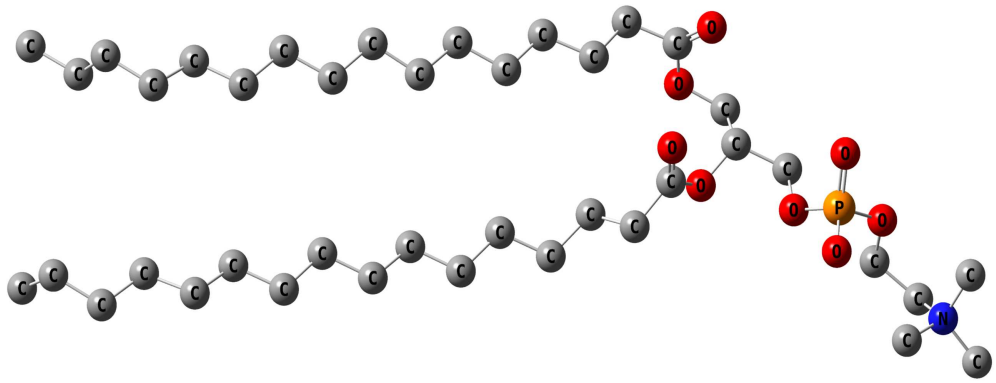

Figure 6.2: Structure of DPPC molecule. Hydrogens are not shown for simplicity.

In these experimental studies X-ray crystallography and NMR have largely been used

and proved to be helpful techniques for elucidating the structure of various kinds of crystalline and amorphous phospholipids. In the present thesis, biological membrane is mimicked by constructing DPPC bilayer-water interface. At this interface mechanism of water insertion upto the starting point of the hydrophobic region of lipid bilayer is studied. The mechanism and the approach of investigation is discussed in detail in chapter 8.

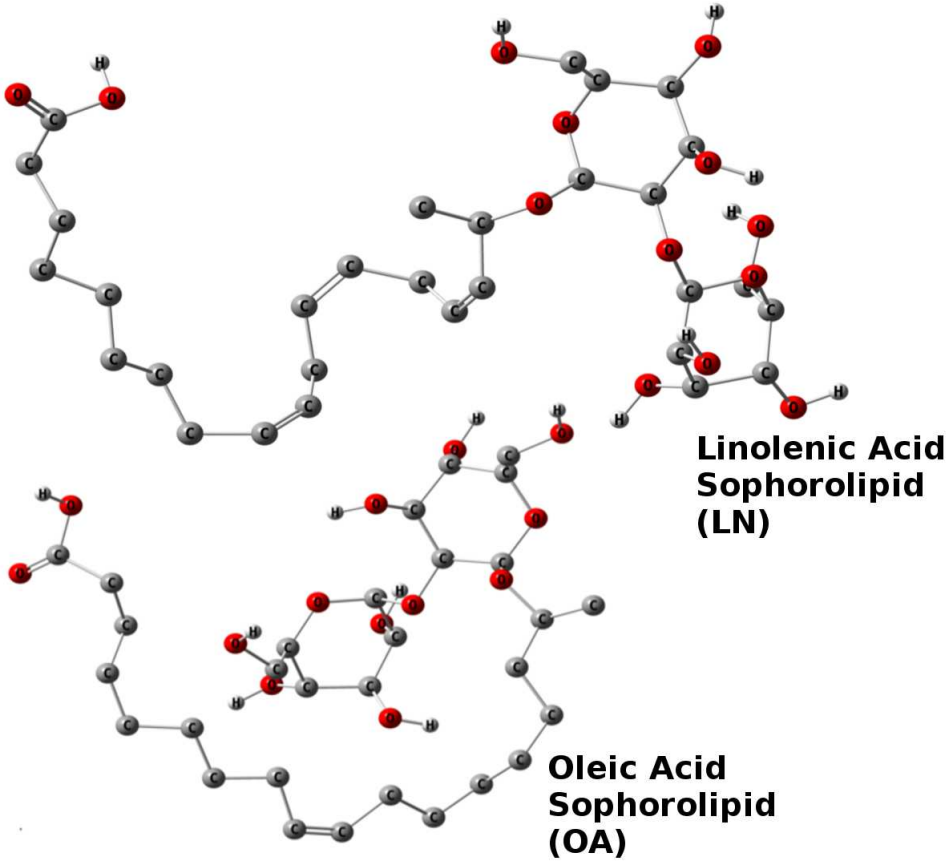

Figure 6.3: Structures of Linolenic acid and Oleic acid sophorolidids. Non-polar hydrogens are not shown for simplicity.

Chapter 9 deals with self-assembly of sophorolipids in water. Sophorolipids contain carboxylic acid group at one end and a dimeric glucose moiety at the other end of a long hydrophobic tail (Figure 6.3) [99]. Since these molecules contain two hydrophilic

groups attached with one hydrophobic tail, they are also called bolaamphiphiles. The hydrophobic chain may contains varying number of cis double bonds (Figrue 6.3). Due to the presence of -COOH group, dimeric glucose moiety, and long hydrophobic tail these molecules form different self-assembled structures at different pH [100]. But the molecular level insight into the self assembled structures is lacking. In the present thesis we have studied the self-assembly of OA and LN in water using classical MD simulations. The details of self-assembly simulations are discussed in Chapter 9.

Chapter 7

Unwinding Mechanisms of Zwitterionic, Capped and Neutral Forms of Different α-Helical Homopolymeric Peptides: In Nanosecond Timescale

7.1 Introduction

Hydrophilicity and hydrophobicity play crucial role in biological systems. Hydrophobic/hydrophilic groups present in biomolecules can control their structure and function (discussed in chapter 6). In the present chapter, early stage unwinding mechanisms of different α-helical homopolymeric peptides are studied in water. The different homopolymeric peptides differ in the degree of sidechain hydrophobicity. This

way, the mechanisms of unwinding can be distinguished as a function of sidechain hydrophobicity.

Secondary structure of peptides and proteins refer to the highly regular local substructures. α-helices are the most abundant secondary structure among all the secondary structures of protein. Hydrogen (H-) bonded structures of α-helix was first proposed by Pauling and Corey[101]. Since then many studies have been performed to understand the stability of α-helices ([89] and references therein). H-bonding between the carbonyl oxygen (C=O) of ith residue and amide hydrogen (NH) of $i+4$th residue on the peptide backbone gives the peptide chain a α-helical structure. Being the mostly available secondary structure, understanding of the unwinding mechanism of α-helices may augment our understanding of protein unfolding.

Experimental and theoretical studies have been performed to understand the structure, stability, and dynamics of helices. Kemp et al. have a series of studies on helices using ^{1}H NMR, ^{13}C NMR, and also CD spectroscopic techniques [102–104]. Zagrovic et al. have measured the radii of gyration of alanine based peptides using synchrotron radiation and the small-angle X-ray scattering techniques [105]. They have also analyzed the discrepancies using the analytical Zimm - Bragg - Nagai theory and with molecular dynamics (MD) simulations. Podtelezhnikov et al. have shown the influence of H-bonding on polyalanine conformations using Metropolis Monte Carlo procedure for protein modeling [106]. Agostini et al. have used generalized simulated annealing method coupled to the GROMOS96 molecular force field to find the minimum energy conformation of polyalanine [107]. Recently Diana et al. have studied the thermal unfolding of a 15-mer endothelial growth factor mimicking α-helical peptide through combination of computational and spectroscopic analysis [108]. Asciutto et al. have further studied the AP peptide (a 21 residue ALA rich

peptide) and have observed unwinding from the terminal of the helical chain[109].

α-helical peptides of only one type of amino acid, i.e., homopolymeric, have been studied in the past to understand various properties of a helical structure. Helical propensity of various amino acids have been defined by studying different homopolymeric peptides ([89] and references therein). Sorin et al. have chosen capped polyalanine and Fs peptide (α-helical arginine substituted analogue of capped polyalanine) in their study to understand helix-coil transitions [110]. Garcia et al. have studied the effect of implicit and explicit solvation on helix-coil transition and established force fields [111–113]. MD simulations have proved to be an useful tool in understanding the mechanism of helix formation, its stabilization, and disruption [114].

In our previous report we have studied the early stage unwinding mechanisms of only zwitterionic α-helical polyalanine (PA), polyleucine (PL), and polylysine (PLY) in water at 300 K using classical MD simulations [115]. We have proposed that the unwinding of 30 amino acid long chain of zwitterionic α-helical PA, PL, and PLY is triggered by higher fluctuations of the terminal residues. The unwinding is relayed from the terminals to the middle for PA and PL, but not for PLY. After initial unwinding from the terminals the PLY helix broke in the middle due to inter residual H-bonding in the side chain. In continuation to the study of zwitterionic form of PA, PL, and PLY here we present the similarities and dissimilarities of early stage unwinding mechanisms of the capped and neutral form of these helices. We have also studied the unwinding mechanisms of zwitterionic, capped, and neutral polyglutamic acid (PG) helices in the present chapter. The C- and N-terminals were capped with -$NHCH_3$ and -$COCH_3$ respectively in all the capped helices. The terminals were kept as -NH_2 and -COOH in all the neutral helices. These are compared with the zwitterionic helices where the terminal residues were taken as -COO^- and -NH_3^+.

The primary motivation to study the unwinding mechanism of the different forms of the homopolymeric α-helical peptides is to gain information for designing stable helical peptides in the future to understand the diseases caused due to unwinding of protein, protein-drug interactions and other biological phenomenon. Know-how of such unwinding can help in developing predictive models for determining early stage unwinding positions of α-helical peptides and proteins. We are systematically targeting to elucidate the unfolding behaviour of amino acids in their own environment as a step forward to understand the early stage unwinding of naturally occurring proteins and peptides.

Here we have considered four different 30 amino acid long polypeptides PA, PL, PLY and PG and their three different forms - zwitterionic, capped and neutral. To check the statistics we perfomed three independent simulations of these helices in water and have proposed their unwinding mechanisms. The resullts of all sets of simulations are presented here. ALA and LEU were considered because of their higher helix forming propensity among amino acids with hydrophobic alkyl side chain [116]. Additionally, their polymers PA and PL differ in the degree of side chain hydrophobicity as ALA has methyl and LEU has isobutyl group as side chain. PLY contains -NH_2 group in its side chain which is hydrophilic in nature. The purpose for choosing polymer of glutamic acid in the present chapter is to compare the unwinding mechanisms of the PG helices with the PLY helices. LYS contains -NH_2 group in its side chain, and we have observed that inter residual H-bonding among these side chain -NH_2 groups influence the unwinding mechanism of zwitterionic PLY helix. GLU contains propanoic acid (-$(CH_2)_2$-COOH) group in its side chain. Thus there exists a possibility of formation of inter residual H-bonding among the side chain -COOH groups in the PG helices. Apart from this, the effect of the short length hydrophobic

spacer group (-$(CH_2)_2$) and hydrophilic side chain in PG can be explored on the early stage unwinding mechanism. LYS contains n-butyl amine (-$(CH_2)_4$-NH_2) group in its side chain. However the hydrophilic character is similar in the GLU and LYS side chains. The zwitterionic PLY and PG with side chain as -NH_2 and -COOH respectively are physically difficuilt to synthesize so it is only of theoretical interest. This is because the PLY side chain and PG side chains can remain as -NH_2 and -COOH only at a high and low pH respectively. But at high pH the N-terminal can not remain as -NH_3^+ and at low pH C-terminal can not remain as -COO^-. Such a condition is difficult to achieve experimentally. However, such forms of PLY and PG serve our purpose of introducing hydrophilic groups with different spacer groups length in the side chain to understand its effect in the unwinding mechanism of helices containing different terminal groups.

Sharp distinctions have been observed in the unwinding mechanisms of polypeptides with the change in terminal groups. The neutral forms of the helices containing hydrophobic side chains i.e. PA and PL tend to unwind from the terminals similar to their zwitterionic analogue and this unwinding is relayed to the middle. Their capped forms start to unwind from the terminals, which is not relayed further to the middle. PLY helices of all the forms (zwitterionic, capped, and neutral) with hydrophilic side chain unwind from the middle. All the forms of PG helices unwind from the terminals. The mechanism determining this interesting distinctions in the early stage unwinding pathways have been investigated for the first time in this report .

The role of water in unwinding of α-helical peptides has been studied in the past by DiCapua et al. [117, 118]. H-bond exchange method is an useful tool to understand the H-bonded structures in proteins [119]. Several approaches taken to realize the relation between solvation and peptide folding has been explained by

Baldwin [120]. An α-helix unwinds in water due to the exchange in intra backbone H-bonding between C=O of ith and NH of i+4th residue with H-bonding with water. In the present chapter also we have investigated the role of water in the unwinding mechanism of the different helices.

7.2 Computational Methods

All the simulations were performed using GROMACS 4.0.7 package [121, 122]. All atomistic OPLS force field [123] has been used for the study. In our previous study [115] we have performed the calculations with Amber force field [25] also and showed that amber over stabilizes the helix but produces the same result in longer time scale for zwitterionic helices. All the peptide helices were first energy minimised using steepest descent method to relax the angles and dihedrals. Then all the systems were constructed by placing the energy minimised peptide in the middle of the simulation box maintaining a distance of 2 nm from the walls of the box. Then the peptide helix was solvated with water. Explicit TIP3P [124] water model has been used in the study as it is the most acceptable water model for studying biomolecules. Further, a 2 ns equilibration run was performed with peptide being position restrained. This allowed the water molecules of the system to equilibrate and organise themselves around the peptide. Finally the position restraint was taken off and trajectories were recorded for 30 ns for further analysis. Three independent sets of simulation for each case, i.e. zwitterionic, capped, neutral, were performed with different initial configuration of water molecules. The initial velocities were also different for all these different simulation sets.

This chapter primarily deals with the understanding of early stage unwinding

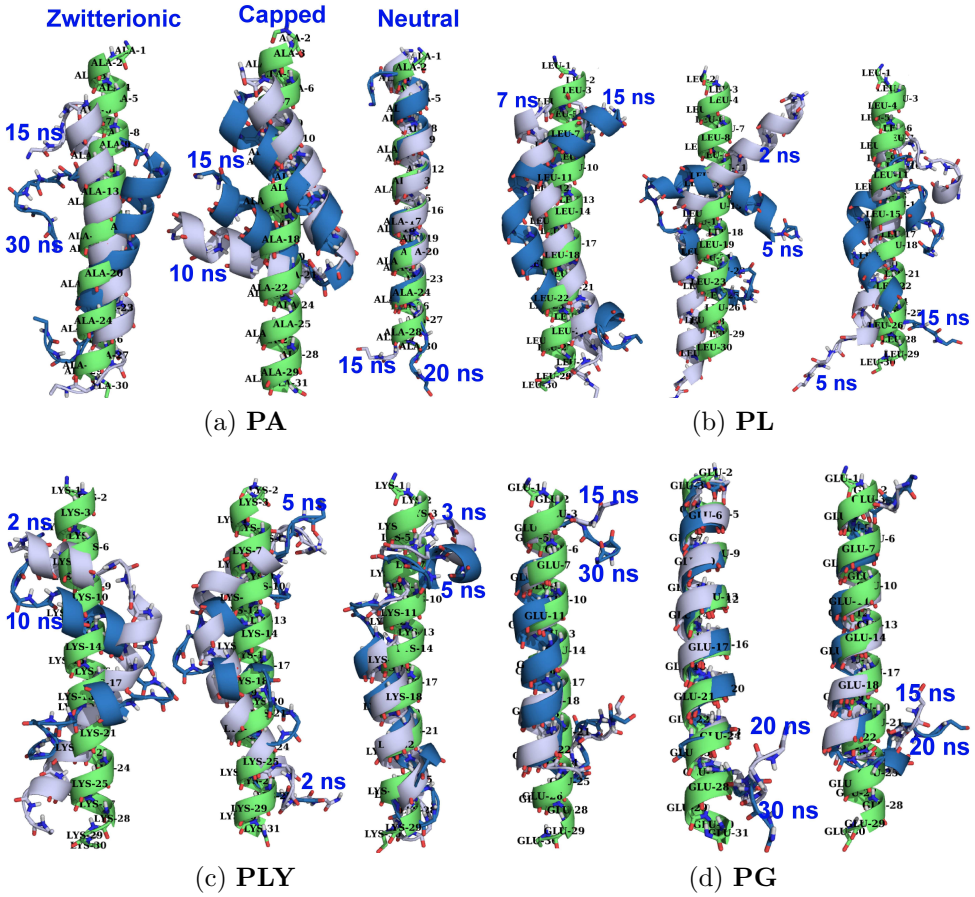

(a) **PA** (b) **PL**

(c) **PLY** (d) **PG**

Figure 7.1: Snapshots at different times for (a) PA, (b) PL, (c) PLY, and (d) PG helices. Water and side chains have not been shown for simplicity. 0 ns is shown with green in all the systems. Other colours corresponding to other times have been indicated in the figures. The order of zwitterionic, capped, and neutral from left to right has been maintained in all the systems similar to the PA system.

mechanisms of various forms of homopolymeric α-helices. In this 30ns timescale, various conformational changes were obseved for the helical peptides, also, unwinding and potential rewinding also takes place in this time scale. Thus simulation time of 30 ns provides us ample scope for further analysis. Isothermal and isobaric ensemble (NPT) and periodic boundary conditions (PBC) were used. Temperature was kept constant at 300 K for all the three systems using v-rescale thermostat. Isotropic

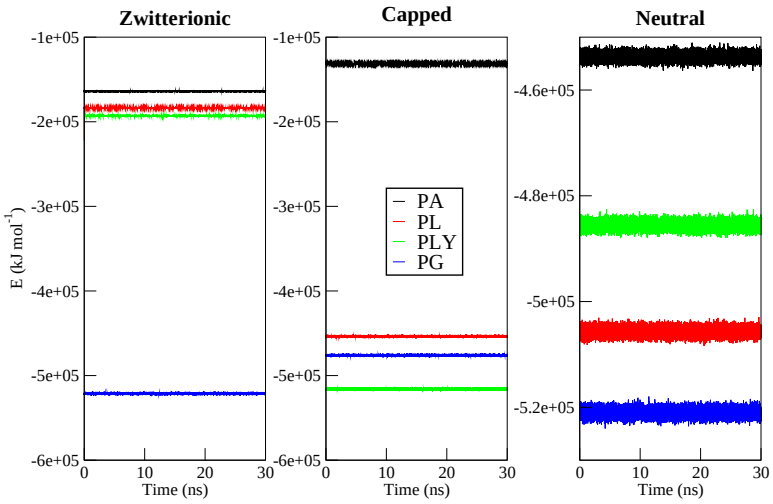

Figure 7.2: Potential energy of the whole system with respect to time.

pressure coupling was applied using Berendsen barostat [38] for all three systems. Bonds were not constrained and a time-step of 1 fs was used for the simulations. For Lennard-Jones interaction, a cut-off at 1.0 nm was applied; electrostatic interactions were taken care of with particle mesh Ewald (PME) [125] method with a real space cut-off of 1.0 nm. Trajectories were analyzed to calculate root mean square fluctuations, and radial distribution functions. All other analysis methods have been described along with results and discussions. The potential energies as a function of time (30 ns) for all the forms, for the simulation set 1, has been checked and depicted in Figure 7.2 to confirm that there is no phase change in this period of time.

7.3 Results and Discussion

We report here the unwinding mechanisms of various forms of PA, PL, PLY, and PG helices. The unwinding mechanisms of zwitterionic form of PA, PL and PLY

helices have been included in our previous report[115], here we present the unwinding mechanisms of neutral and capped forms of PA, PL and PLY. In addition to neutral and capped forms, zwitterionic form of PG has also been reported in the present chapter and a systematic comparison has been performed.

7.3.1 Position and Time-scale for Unwinding of the Helices

Noticeable distinctions have been observed in the unwinding pathways of the various helices with the change in terminal groups. Snapshots at various times for the different systems have been shown in Figure 7.1. Water and side chains of the amino acids have not been shown for simplicity. Capped form of both PA and PL appear to unwind from the middle of the α-helical chain (Figures 7.1a and 7.1b). The neutral and zwitterionic forms of both of these α-helices unwind from terminals (Figures 7.1a and 7.1b). All the forms of PLY unwinds from the middle of the helical chain (Figure 7.1c). Snapshots of zwitterionic, capped and neutral forms of PG have been depicted in Figure 7.1d. All the forms of PG appear to be unwinding from the terminals in the initial 30 ns (Figure 7.1d).

The time-scale of unwinding of different helices have been estimated from the distribution of distance between C=O of ith and NH of i+4th residues as a function of time shown in Figure 7.3.1. Since H-bonding between C=O of ith and NH of i+4th residues is responsible for the α-helical structure of a peptide, the distance distribution as a function of time gives the estimation of the time-scale of breaking of such H-bonds. Distance between C=O of residue 1 and NH of residue 5, and C=O of residue 11 and NH of residue 15 were first calculated and the distributions were plotted averaging over each 2 ns intervals of time for the systems. All the distance distributions were

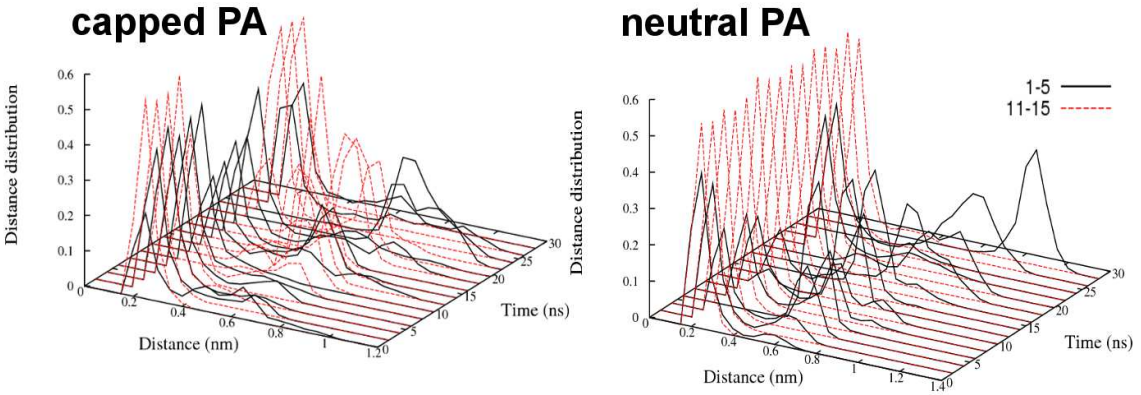

(a) **PA**

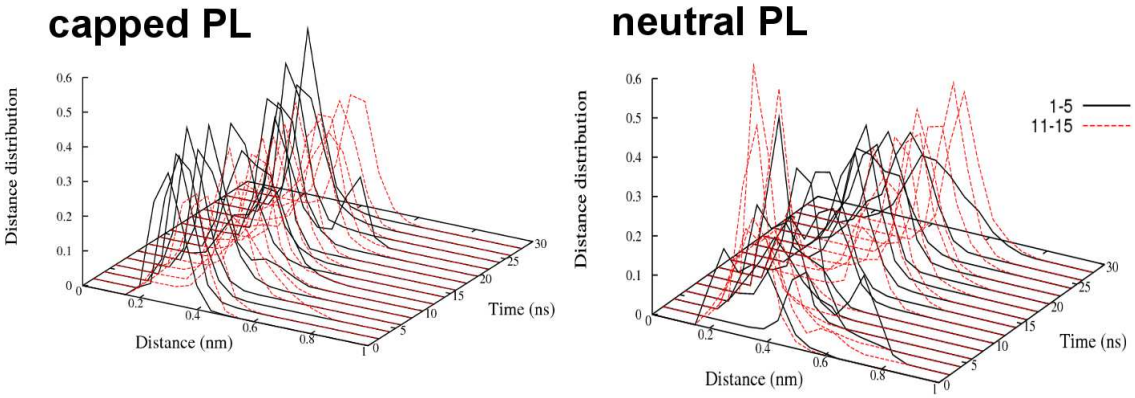

(b) **PL**

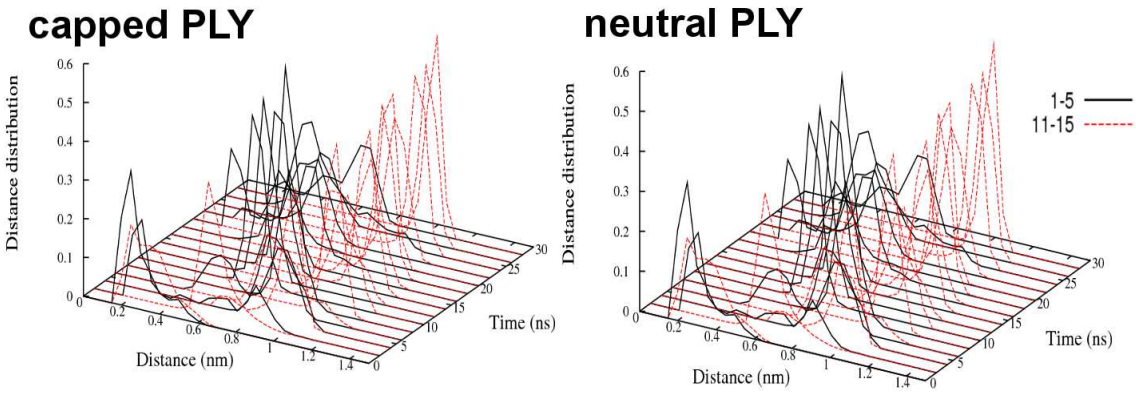

(c) **PLY**

Figure 7.3:

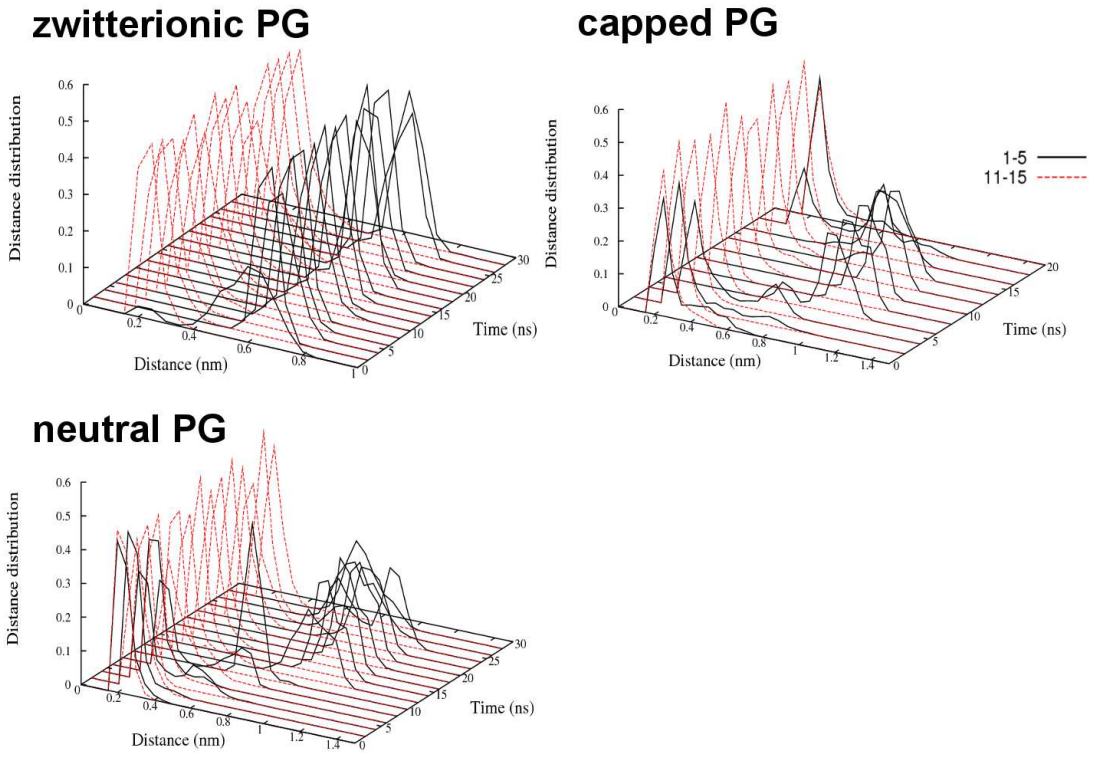

(d) **PG**

Figure 7.3: Distribution of distance between C=O of residue 1 and NH of residue 5, and between residue 11 and residue 15 plotted against time for (a) PA, (b) PL, (c) PLY, and (d) PG helices.

averaged over number of frames in the 2 ns interval of time. The capped PA and PL helices unwind from the middle (see Figures 7.1a and 7.1b). Therefore the distance distributions between residue 11 and residue 15 for these helices move away from H-bonding distance much earlier than distance distributions between residue 1 and residue 5 (Figures 7.3a and 7.3b). This shows that the middle residues unwind much earlier than the terminal residues for capped PA and PL helices. But for neutral PA and neutral PL helices (Figures 7.3a and 7.3b) the case is opposite. This shows that the neutral PA (in nearly 8 ns) and neutral PL (in nearly 2 ns) starts to unwind from the terminals as in the case of zwitterionic PA and PL [115]. Further, similar distance

distribution plots for all the forms of PLY (zwitterionic [115]) shows that it unwinds from the middle of the α-helical chain (Figure 7.1c) in a time-scale of initial 2-3 ns. Similar distance distribution were also plotted for the other two simulation sets and are depicted in Figures 7.3.1 and 7.3.1.

In some of the cases, a difference of 2-4 ns have been observed in the unwinding timescales, but, the mechanism of unwinding remains the same. All the forms of PG helices are observed, from the snapshots, to be unwinding from the terminals (Figure 7.1d) but none of them unwinds completely in the 30 ns simulation time. The distance distribution of PG between residues 1 and 5 are seen to be moving away from H-bonding distance at very early stage for all the forms of PG helices (Figure 7.3d). But the distance distributions between residue 11 and residue 15 do not shift from H-bonding distance in 30 ns (Figure 7.3d). A shift in the distance distribution plot for neutral PG in the second simulation set can be observed around 24 ns timescale (Figure 7.3.1). In the present context where we are interested in understanding the early stage unwinding mechanism of the helices, the pattern of unwinding of PG is clear in this time-scale of 30 ns.

7.3.2 Fluctuations and Unwinding

Unwinding of the helices from terminals can be attributed to the higher fluctuation of the terminal residues. To check this we have investigated the relationship between unwinding of the various helices to the fluctuations of the residues present in the respective helices. Root mean square fluctuation (RMSF) of the (C_α) carbons of helical backbone has been plotted in Figure 7.6. All these RMSF plots have been calculated for certain intervals of time, i.e., 0-1 ns, 1-2 ns etc. The intervals were

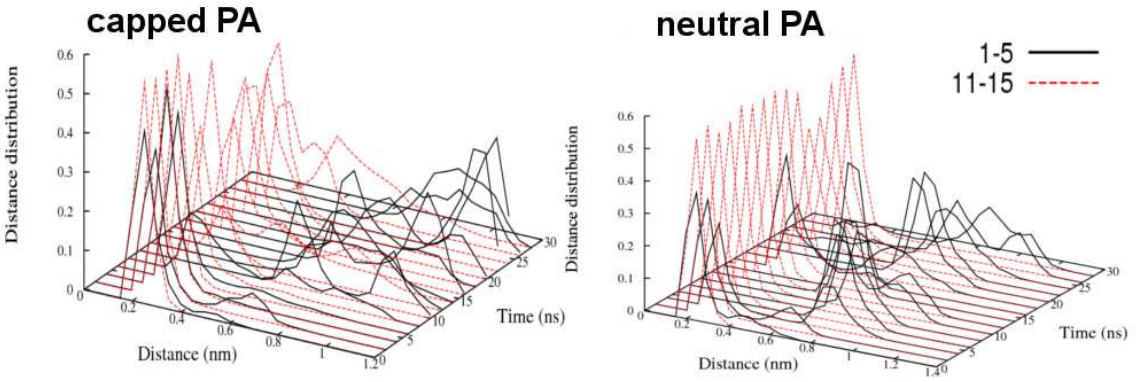

(a) **PA**

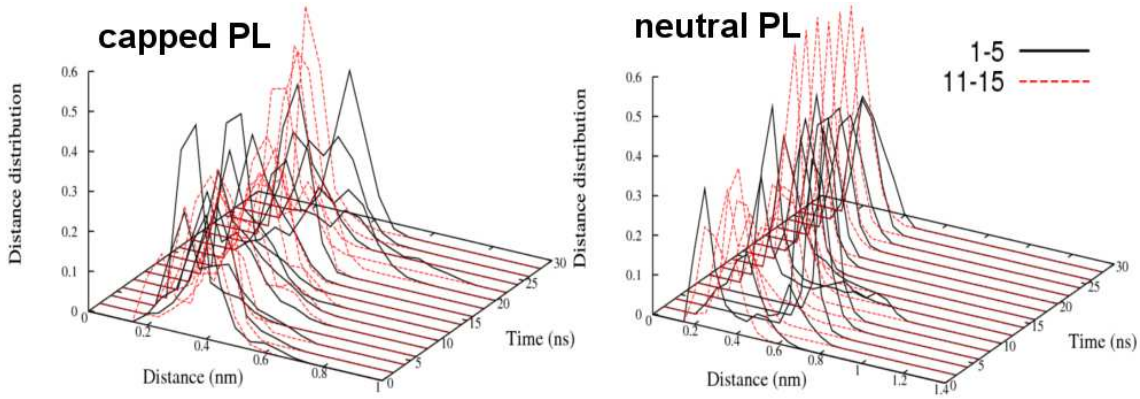

(b) **PL**

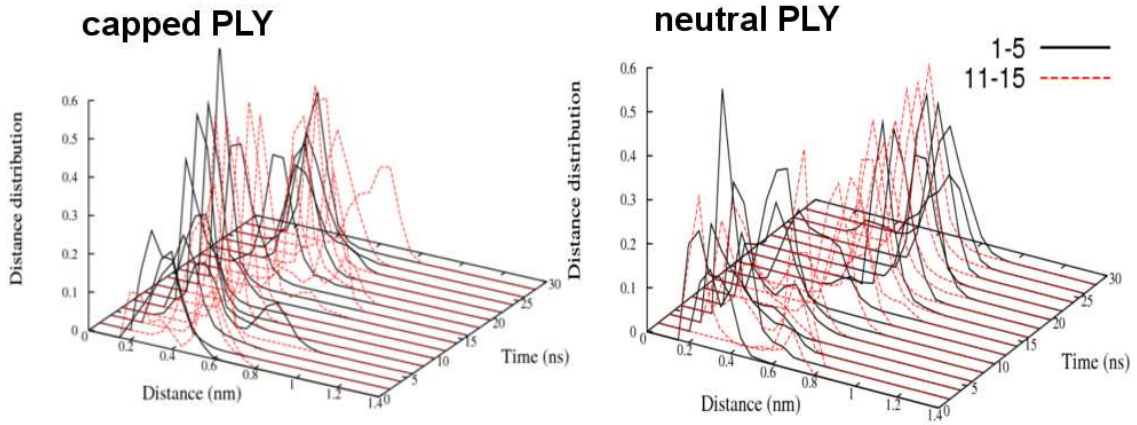

(c) **PLY**

Figure 7.4:

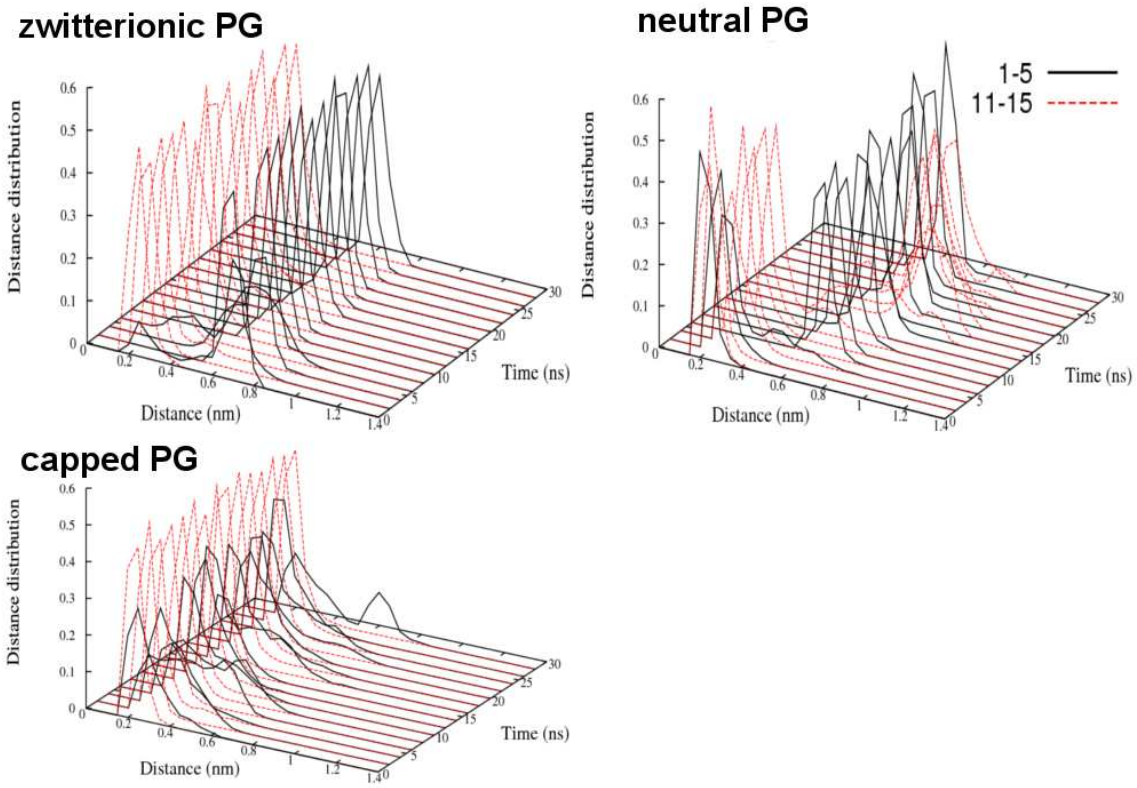

(d) **PG**

Figure 7.4: Distance distribution plots from **Simulation set - 2**.

chosen depending upon time-scale of unwinding of the investigated helices as observed from the distance distribution from Figure 7.3.1.

For both capped and neutral PA helices the intervals were chosen to be 5 ns (Figure 7.6a). The capped PA helix unwinds completely in 30 ns, but not the neutral PA helix. It is evident from the snapshots that the capped PA helix unwinds from the middle of the α-helical chain (Figure 7.1a). RMSF for the (C_α) carbons of terminal residues is the highest in the first interval, i.e., 0-5 ns for capped PA (Figure 7.6a). Further as the time increases, the RMSF of (C_α) carbons of the middle residues increase and become almost equal to the RMSF of N-terminal residue. Asymmetry

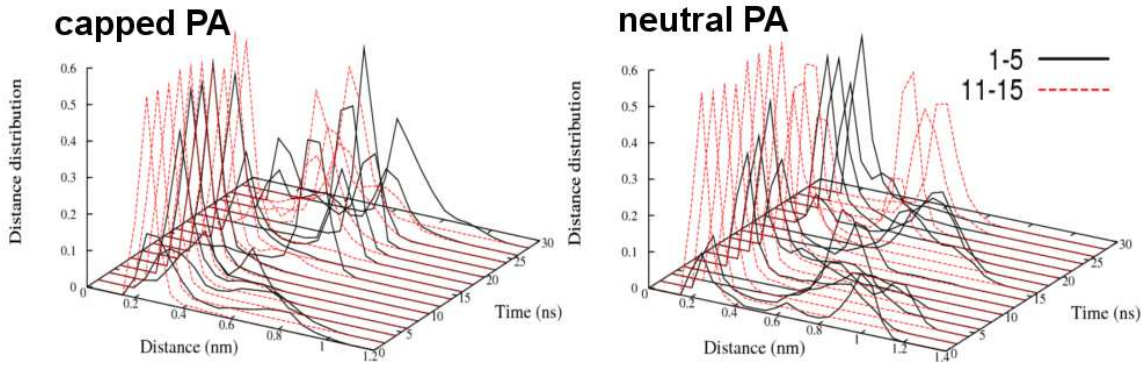

(a) **PA**

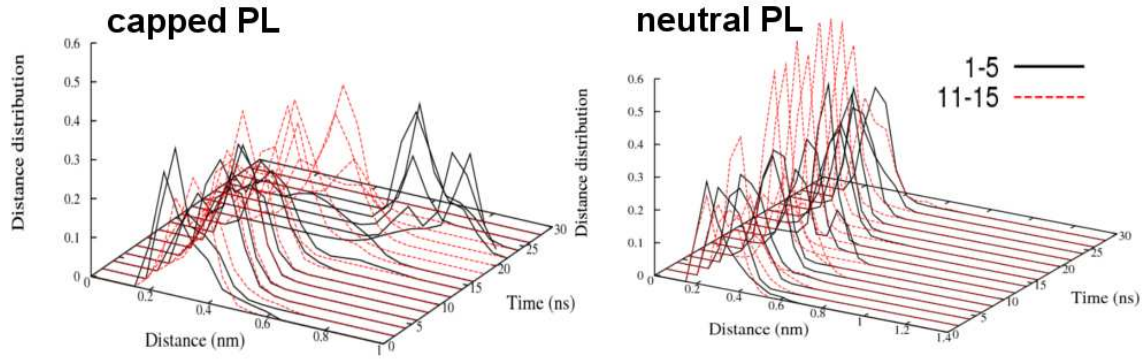

(b) **PL**

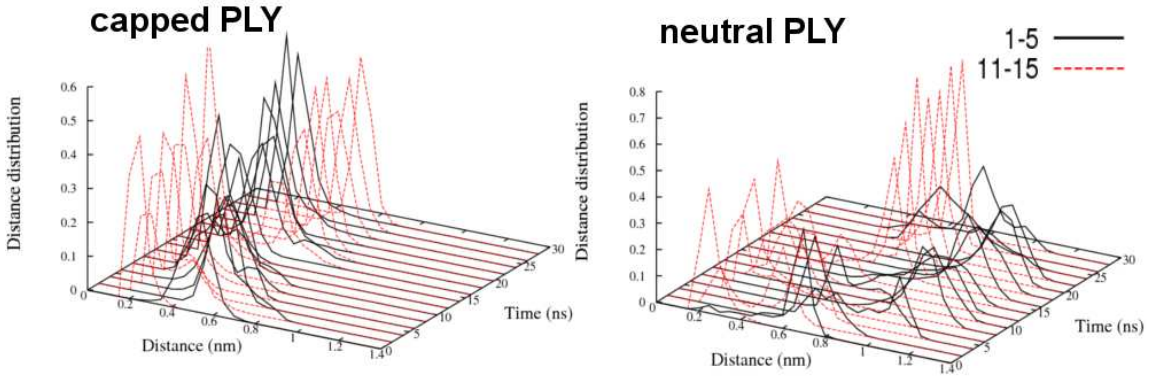

(c) **PLY**

Figure 7.5:

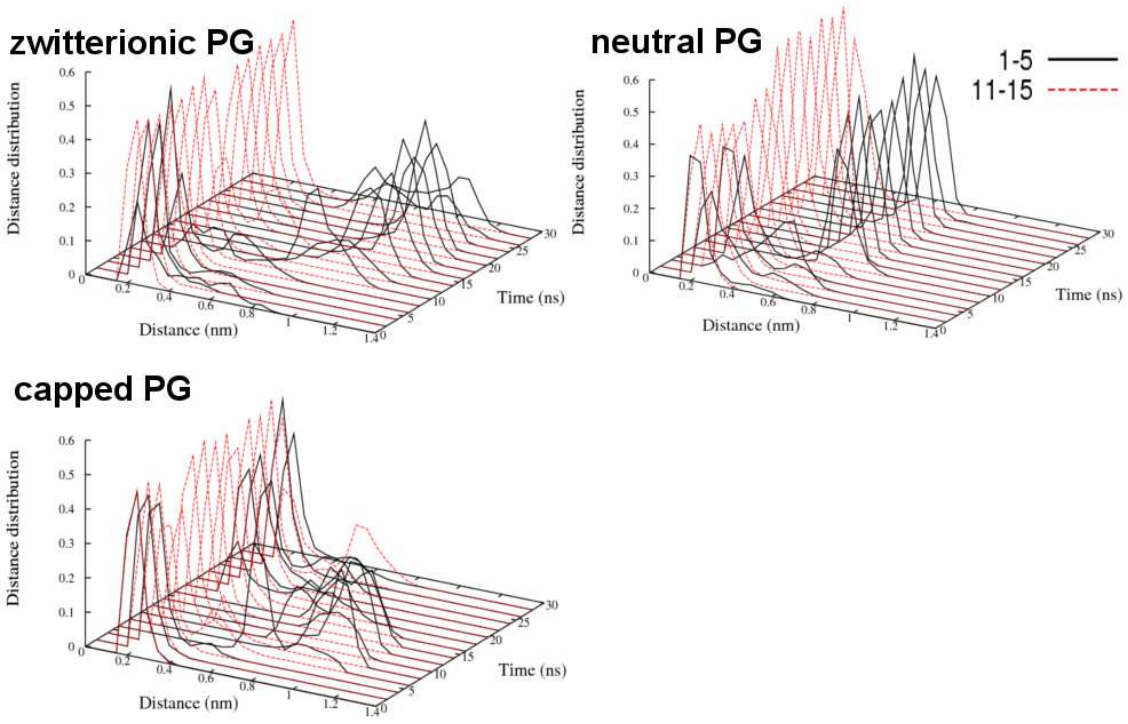

(d) **PG**

Figure 7.5: Distance distribution plots from **Simulation set - 3**.

in the unwinding is visible in the 0-5 and 5-10 ns intervals as the RMSF of the residues near C-terminal (residue 30) is higher than that of N-terminals (residue 1). However for neutral PA helix the RMSFs of the terminal residues are higher in all intervals (Figure 7.6a). The asymmetry in RMSF is visible in some cases in some particular time intervals e.g., 25-30 ns for neutral PA. Though the unwinding of neutral PA is not complete in the 30 ns time-scale, the early stage pattern of unwinding is distinct from the terminals of the α-helical chain. Zwitterionic PA shows the similar property as reported earlier [115]. Similar to PA, capped and neutral helix of PL unwinds from middle and terminals respectively (Figure 7.1b). But the time-scales of unwinding of

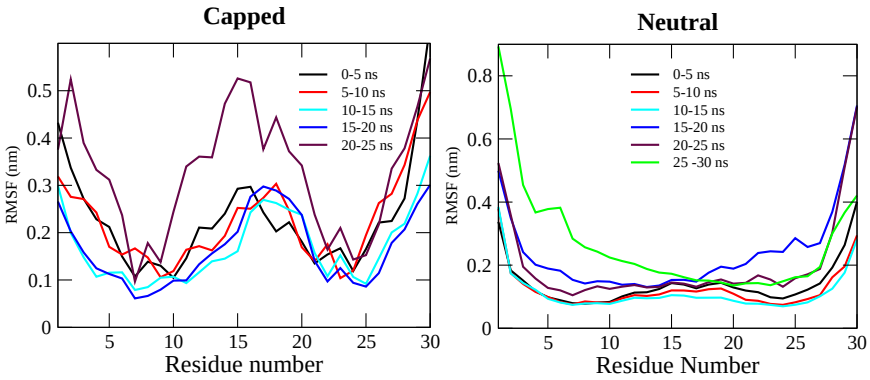

(a) **PA**

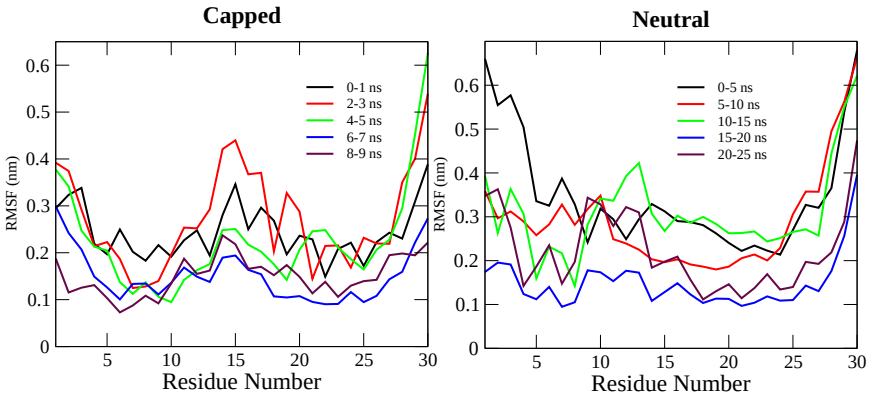

(b) **PL**

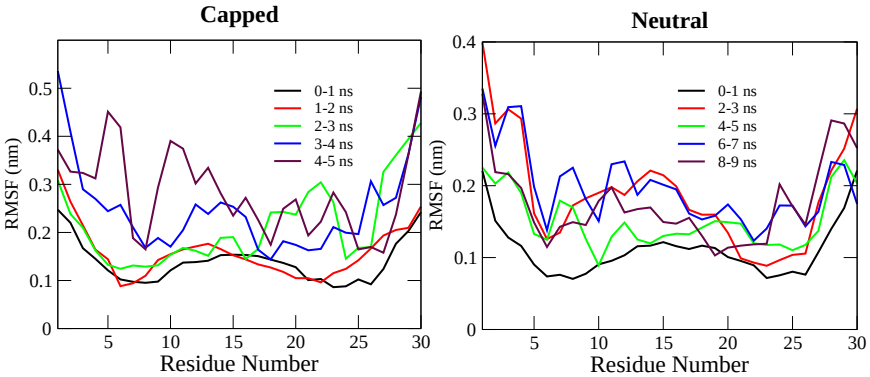

(c) **PLY**

Figure 7.6:

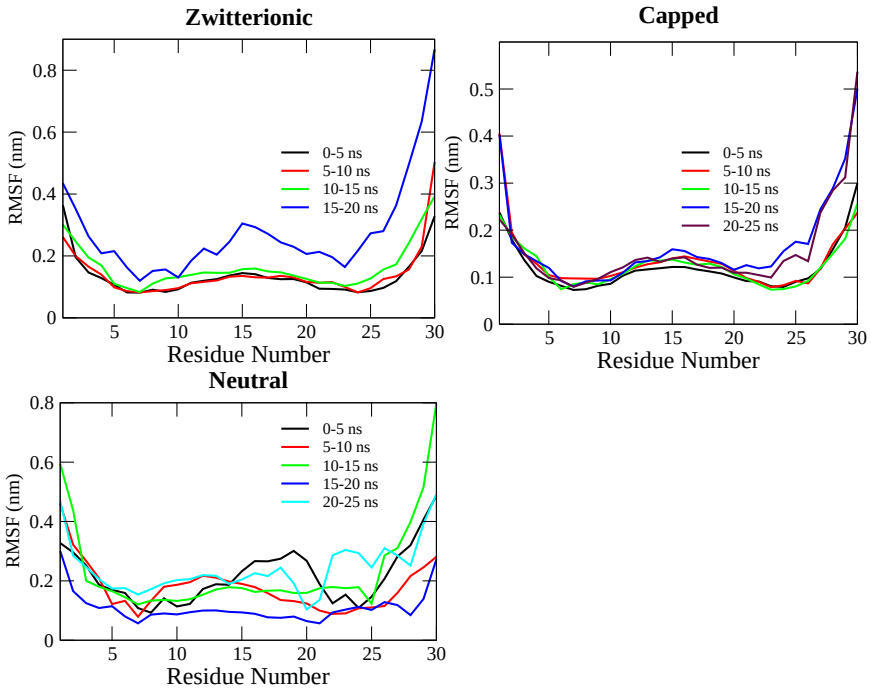

(d) **PG**

Figure 7.6: RMSFs of C_α carbons on the helical backbone at different intervals of time for (a) PA, (b) PL, (c) PLY, and (d) PG helices.

PL helices are different than that of PA helices (Figure 7.3.1). Capped PL unwinds completely within 10 ns and the neutral PL in 30 ns. Thus the intervals selected for plotting RMSFs were 1 ns upto 10 ns for capped PL and 5 ns upto 30 ns for neutral PL (Figure 7.6b). The RMSFs of the middle residues are almost similar to that of the terminal residues in the 0-1 ns interval for capped PL (Figure 7.6b). The RMSFs of the middle residues further increases in the 2-3 ns interval. This validates the unwinding of the capped PL helix from the middle of the α-helical chain triggered by the fluctuation in the middle residues. For neutral PL helix the RMSFs for the terminal residues are distinctly higher than the middle residues in the 0-5 ns interval (Figure 7.6b) and helix breaks from the terminal. A sharp drop in the RMSFs of the N-terminal residues can be observed in the 5-10 ns compared to 0-5 ns interval. This

is possibly because of the rewinding in that time interval for these residues.

The zwitterionic α-helical PLY starts to unwind from the terminals because of higher fluctuations of the terminal residues, but the unwinding is not relayed to the middle of the α-helical chain [115]. Instead, the side chain -NH_2 groups of lysine form inter residual H-bonds and the helix breaks in the middle. We have also observed for both neutral and capped PLY helices, the RMSFs (Figure 7.6c) of the terminal residues are higher than the middle residues in the first intervals. With increasing time the fluctuations of the middle residues keep increasing. However, the snapshots for both neutral and capped PLY helices (Figure 7.1c) suggest unwinding from middle of the α-helical chains. Similar RMSFs have been calculated and depicted in Figure 7.6d for zwitterionic, capped, and neutral PG helices . All forms of PG helices do not completely unwind in the 30 ns time-scale. But, unwinding and rewinding to α-helical state has also been observed in 30 ns time-scale for all the forms of PG helices. The RMSFs for the terminal residues is higher than the middle residues in all intervals of time for all the forms of PG (Figure 7.6d). Therefore the unwinding pattern remain same even after rewinding for all forms of PG helices, i.e., all the helices unwind from the terminals (Figure 7.1d). Higher fluctuations of the terminal residues triggers the unwinding process for all forms of PG helices. Asymmetry in RMSF for terminal residues can again be observed here because the RMSFs of the C-terminal (residue 30) residues attain higher value than the RMSFs of N-terminal (residue 1) residues in the same intervals of time (Figure 7.6d) for all the forms of PG helices. This is also visible in the snapshots of the PG helices (Figure 7.1d).

Radial distribution function (RDF) plots for side chains and main chain H-bonding distances of PLY and PG are depicted in Figure 7.7 to understand H-bonding in these helices with. For all the forms of the PLY and PG helices the main chain RDFs were

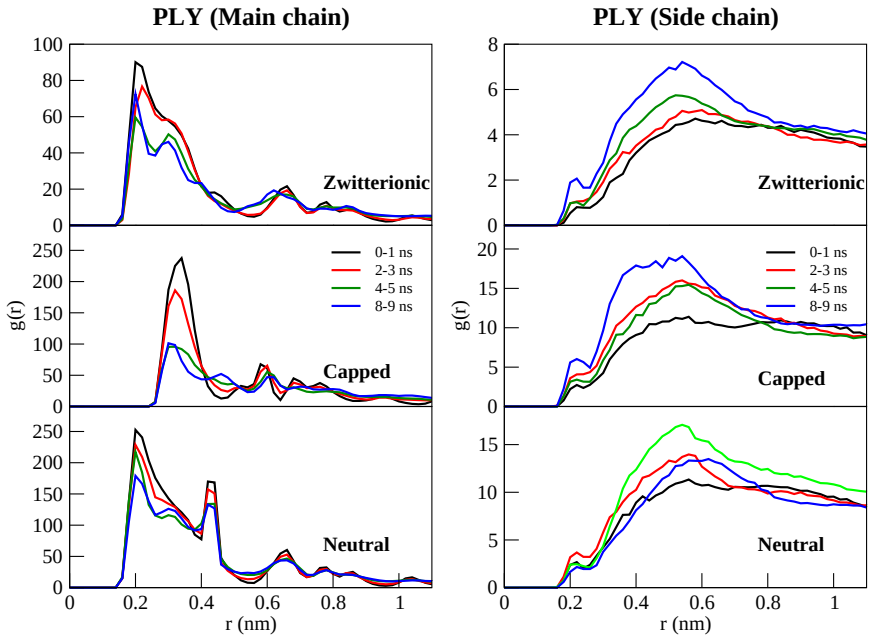

(a) **PLY**

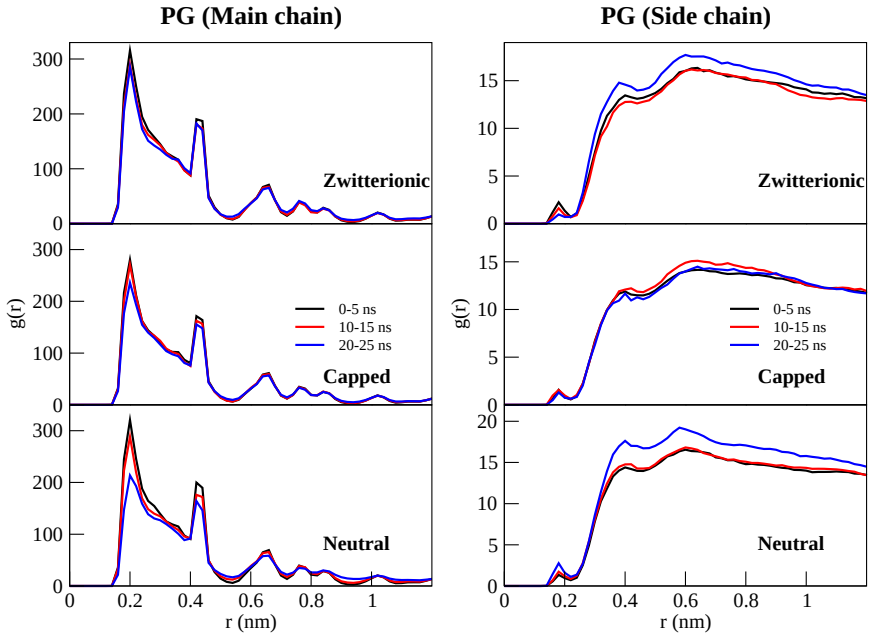

(b) **PG**

Figure 7.7: RDF among the (a) side chain NH_2 groups for PLY helices, and (b) side chain -COOH groups for PG helices at different intervals of time.

plotted between C=O and NH of the peptide backbone. Side chain RDFs were plotted between N and H of the side chain -NH_2 groups for PLY and between oxygens and H of the side chain -COOH groups for PG. All the RDFs are averaged over certain intervals of time, i.e., 1 ns for PLY and 5 ns for PG. From Figure 7.7a the side chain RDF peaks (first peak) for all the forms of PLY are clearly visible to be increasing with time and in the same time-scale the main-chain RDF peaks are decreasing. This suggests that the unwinding of all the forms of PLY helices from the middle of the α-helical chain is driven by inter residual H-bonding among the side chain -NH_2 groups. On the contrary, there is almost no indication of inter residual H-bonding among the side chain -COOH groups in any form of the PG helices (Figure 7.7b). There is almost no change in the first RDF peaks with increase in time. There is, however, a small drop in the peak heights for the main chain RDFs of PG helices because of the unwinding of the helices, though they are from the terminals. The inability of the PG helices to form inter residual side chain H-bonds can be attributed to the lower length of the side chains in PG than in PLY. Possibly because of long flexible side chains, PLY helices attain the proper orientation to create side chain H-bonding.

7.3.3 Role of Water on unwinding of helices

The secondary structure of high propensity α-helical peptides stays as α-helix primarily because of the H-bonding between carbonyl oxygen (C=O) of the ith and amide hydrogen (NH) of the $i+4$th residue of the backbone. These H-bonds can be exchanged with the surrounding solvent (in this case water) to unwind the α-helical peptides. DiCapua et al. have shown that for such an exchange of hydrogen bonding, water molecules must enter the accessible regions inside the helical backbone

[117, 118]. Li et al have studied the effect of solvation and side chain modulation on the peptide backbone conformation using a model peptide $AcGGAGGNH_2$ [126]. Therefore, the role of water in unwinding of the different helices become important. In the present chapter the initial 2 ns position restrained simulations for all the systems allow the water molecules to equilibrate and settle around the α-helix. So water molecules are present in the accessible regions around the α-helical backbone in the initial conformation from which we have started to record the trajectory for analysis.

To understand the effect of water on the unwinding of the α-helical chain, count of water molecules forming H-bond with the backbone NH has been plotted as a function of the distance between water oxygen (OW) and NH in Figure 7.8 for all the systems. The distribution of the H-bond count as a function of distance has been calculated in the following manner. Initially the distance between all the NH and OW in a polypeptide were calculated in all the frames for each intervals of time. Then the donor-hydrogen-acceptor (N-H-OW) angles were computed for all the water molecules confined between 0.1-0.4 nm from NH. Among them only those water molecules were counted for which the N-H-OW angle was greater than 150°considering the linear nature of H-bond. Subsequently the normalized count of hydrogen bond distances has been depicted as histogram with respect to the NH-OW distance. All these distributions were plotted for certain intervals of time similar to the other plots reported. It is observed from Figure 7.8 that the height of peaks of the distributions are increasing with the increment in time for all the systems. This confirms that formation of H-bonds between the peptide backbone and water increases with time. Only for capped PA, the peak height of the distribution decreases at 5-10 ns interval (Figure 7.8a) may be because of some rewinding to the helical form happens in this interval. However, after this interval the peak height increases like other forms of

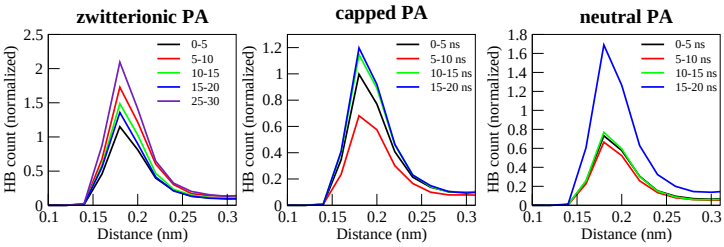

(a) **PA**

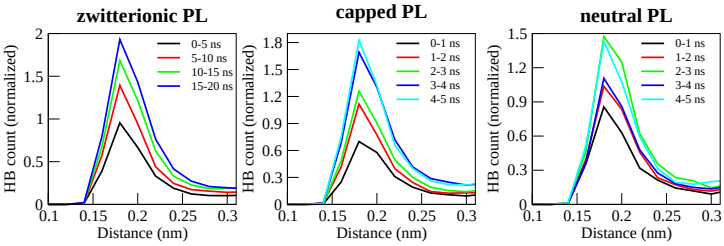

(b) **PL**

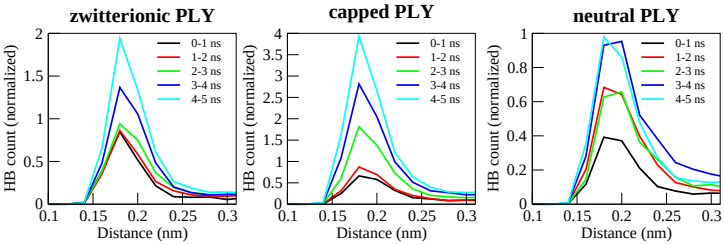

(c) **PLY**

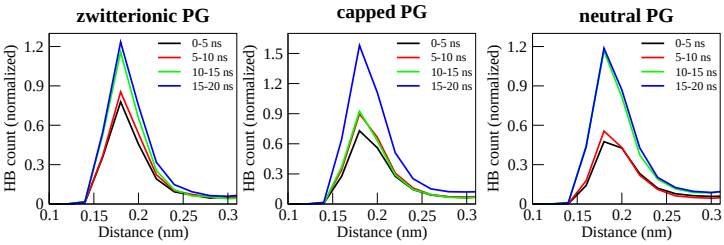

(d) **PG**

Figure 7.8: Count of number of H-bond among backbone NH and water oxygen at different intervals of time for (a) PA, (b) PL, (c) PLY, and (d) PG helices.

helices. H-bond count distribution peak increases continuously in all the intervals for capped PL (Figure 7.8b). However for neutral PL a drop in the peak height can be observed in the 3-4 ns interval (Figure 7.8b). Peak heights of capped PLY also increases with time (Figure 7.8c). Notably the peak height in the last (4-5 ns) interval for capped PLY is the highest among all the systems studied. This is because capped PLY unwinds completely in 5 ns and higher amount of unwinding implies higher probability of H-bonding between NH and OW. For neutral PLY also the peak heights increase, but the peak heights are similar in the 1-2 ns and 2-3 ns intervals and also in 3-4 ns and 4-5 ns intervals. This implies that in these intervals amount of helix unwinding and hence the probability of H-bond formation between NH and OW are similar. All the PG systems have the highest unwinding time-scale among the homopolymeric helices studied here. Any of the PG helices do not completely unwind in the 30 ns time-scale (Figure 7.1d). Zwitterionic PG unwinds with steady increase in the H-bond count in all the intervals (Figure 7.8d). Capped PG shows a sharp increase in the peak height in the 15-20 ns interval and the neutral PG shows a sharp increment in the 10-15 ns interval (Figure 7.8d). The unwinding of the helical chain has some correlation with the H-bond count because in the same time-scale helices also start to unwind. In Figure 7.9 we have elucidated the correlation between the hydrogen bond count and change in helicity as a function of the same intervals of times. Change in helicity is calculated as a ratio between the number of non helical H-bonded (within the backbone) residues and H-bonded residues. We have set a similar criteria to count the H-bonded residues as above. In this plot (Figure 7.9) the count of the H-bond is nothing but the maxima of H-bond count distribution of Figure 7.8 for all the systems. The correlation between the probability of H-bond formation between the solvent water and the change in helicity is evident from all the systems

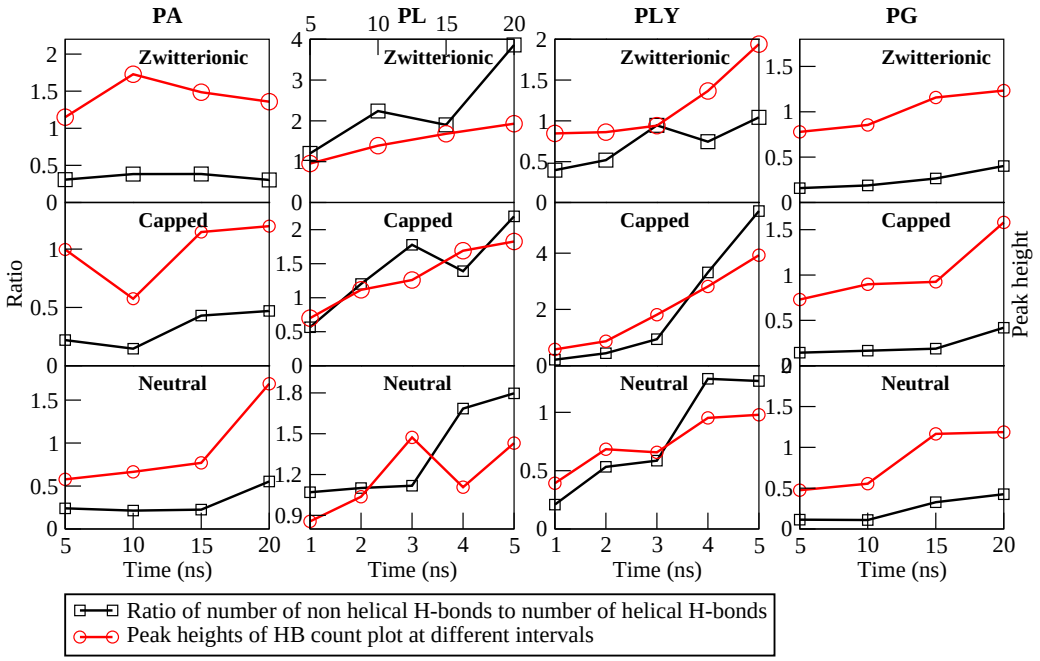

Figure 7.9: Ratio of number of helix forming H-bonds (C=O of ith and NH of i+4th residue) to non helical H-bonds for all the systems plotted against time. Also the peak heights at different intervals of time in Figure 7.8 have been plotted as a function of time. The plot of zwitterionic PL is depicted in 20 ns timescale, but capped and neutral PL are depicted in 5 ns timescale.

as we observed from Figure 7.8. Whenever there is a higher ratio of unwinding versus rewinding the distribution of H-bond distance increases like in neutral PA shows a sharp jump in the peak height in 15-20 ns interval (Figure 7.8a). The jump is due to the maximum amount of unwinding in that time-scale (Figure 7.9). Capped PA shows a dip in the peak height in the 5-10 ns interval due to rewinding as we have predicted from the H-bond distribution. In case of neutral PA there is an increase in helicity (rewinding) is observed in the interval of 3-4 ns, but the H-bond count increases. This is may be because of the faster dynamics of the system. For all the forms of

PG, PA and PLY the correlation is highly satisfactory. Similar correlations have also been investigated for the other two simulation sets (Figure 7.10). Though there is a small difference in the unwinding timescales, the H-bond formation probability among backbone and water molecules, and the change in helicity are highly correlated in the other two simulation sets also.

The measure of average H-bond count is a useful quantity to understand the relation between unwinding of helix and the effect of water on it. But the driving force for exchange of H-bonding within the α-helical backbone with water can not be understood by this. H-bonding is primarily an electrostatic interaction. Thus to understand the exchange of H-bonding within the α-helical backbone with water, electrostatic interaction energy for the H-bonding between C=O of ith and NH of i+4th residue has been calculated and compared with the H-bonding energy between NH and OW (represented by dotted line) in Figure 7.11. For computing these energies Coulombic interaction potential energy among the concerned atoms has been used, i.e., $q_i q_j / 4\pi\epsilon_\circ r_{ij}$, where q_i and q_j are the charges on the concerned atoms and r_{ij} is the distance between them, and $\epsilon_\circ$ is the permittivity of free space. In our simulations the term ϵ_r (permittivity of the medium) is always 1 as the long range electrostatic interactions were taken care by using PME. The term $1/4\pi\epsilon_\circ$ is equal to 138.935 485 kJ mol^{-1} nm e^{-2}. To calculate the electrostatic interaction energy for the H-bonding between C=O of ith and NH of i+4th residue, first the r_{ij} among all these pairs were computed and then the energy was calculated only for pairs which have N-H...O angle more than 150° and r_{ij} was between 0.1-0.4 nm. Further the total energy was normalized by number of residues and frames. Finally normalized distribution of the energy was plotted averaging over the time-scale of early stage helix unwinding, e.g., 15 ns for capped PA and 5 ns for capped PL. The higher range of r_{ij} as H-bond

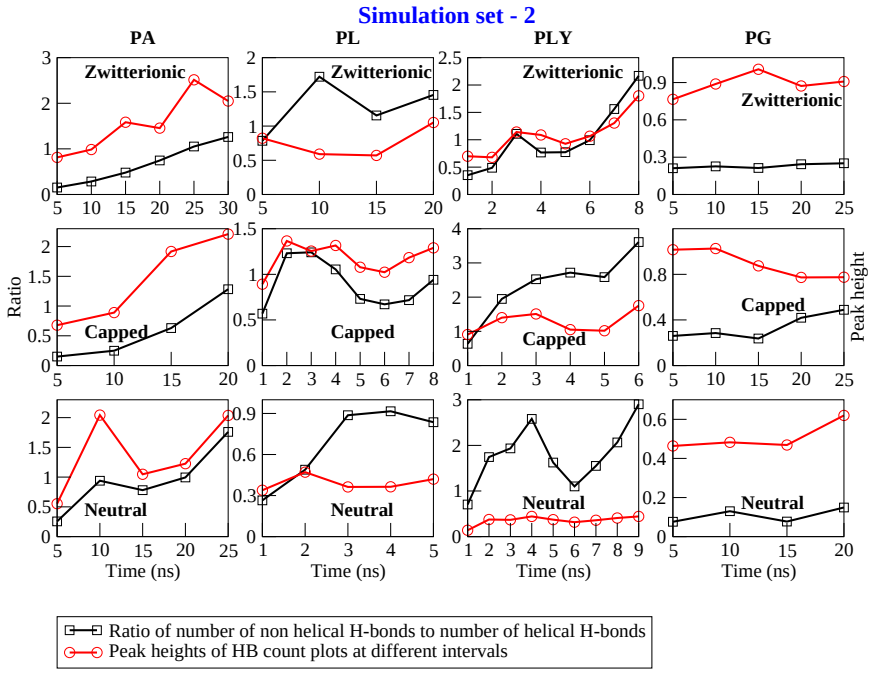

(a)

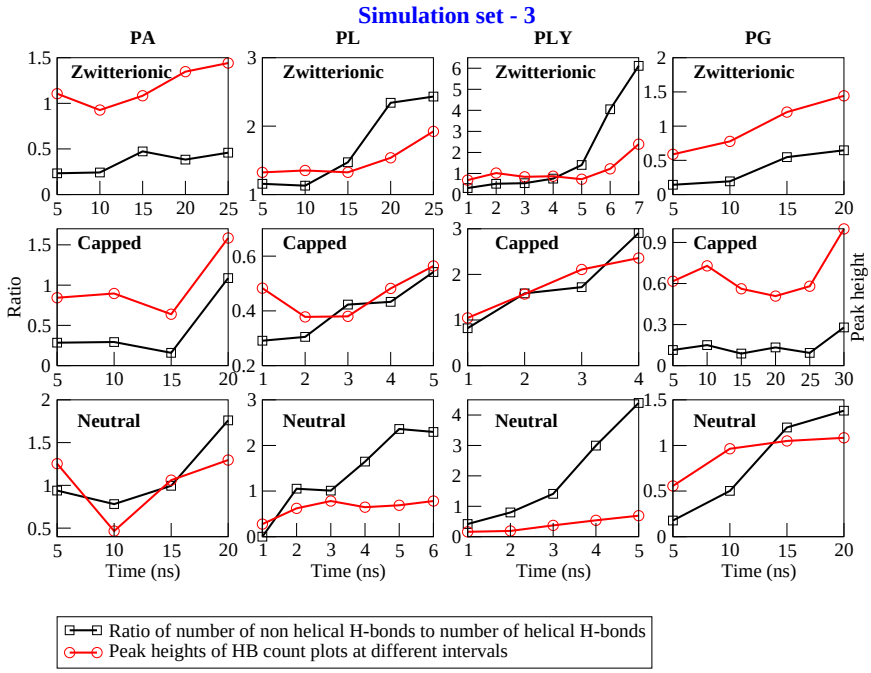

(b)

Figure 7.10: Ratio of number of helix forming H-bonds (C=O of ith and NH of i+4th residue) to non helical H-bonds for all the systems plotted against time. Also the peak heights of HB-count at different intervals of time in are plotted as a function of time.

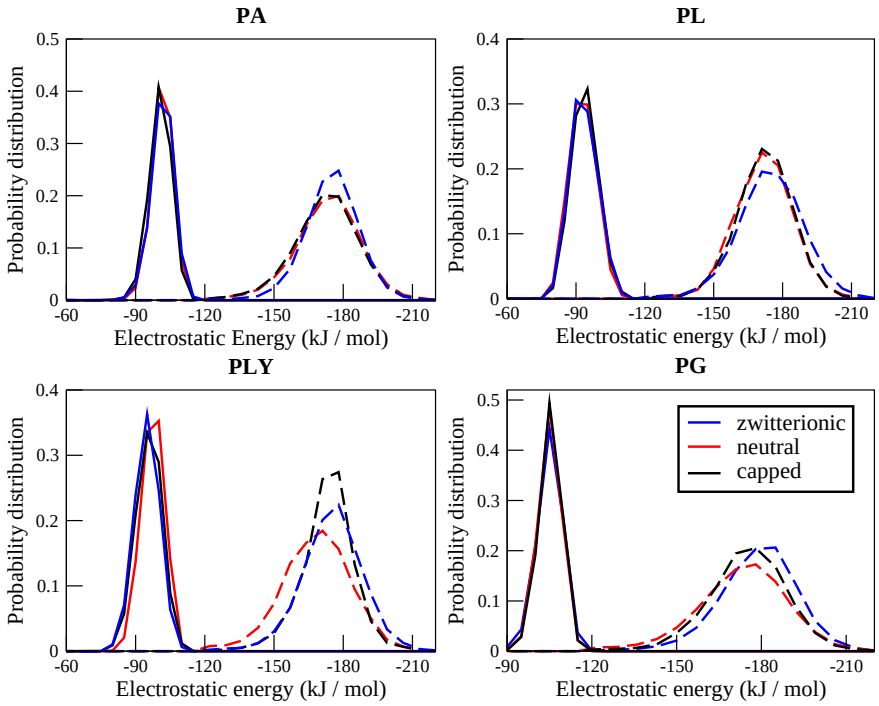

Figure 7.11: Distribution of electrostatic interaction energy of interaction between backbone C=O and NH (solid line), and between NH and water(dashed line).

criteria was chosen to be large as we have observed in Figure 7.3.1, that, the H-bonding distances of the backbone keep fluctuating within this range. Further for calculating the electrostatic interaction energy for the H-bonding between NH and OW same H-bond distance range has been used as in Figure 7.8. The interaction energy between NH and OW (represented by dashed line) is lower than the energy between C=O of ith and NH of i+4th residue (solid line) in the helical backbone for all the systems (Figure 7.11). From this we can infer that the unwinding of the helices are favoured by the more stabilizing H-bonding interactions between NH and OW than the intra helical H-bonding interactions. There is not much difference in the distribution peaks of electrostatic energies for intra helical H-bonding interactions of capped and neutral

systems. This is may be because of the charges on C=O ($q_{C=O} = -0.5$) and NH ($q_{NH} = 0.3$) for all helices studied here are same in the OPLS-AA force field. The end group were not taken into account in any of these distributions. Charge on OW for TIP3P water model is -0.834. Thus there is not much distinction between the distributions of interaction energies among NH and OW for all the helices except PLY. Peak of capped PLY appears at considerably higher value than neutral PLY. This is due to the fact that capped PLY has the highest distribution of H-bond count (Figure 7.8c). Thus higher probability of H-bonding due to the favorable H-bond electrostatic energy translates to highest unwinding. The peak distribution for electrostatic energy between NH and OW is broader than similar energy between C=O of ith and NH of i+4th residue. This indicates the fluctuations in the energy values are larger for H-bonding interactions between NH and OW than the intra helical H-bonding interaction. To show this energies as a function of time has been included and discussed in the Figure 7.12. As observed in the distributions also, the electrostatic energy between NH and water if always higher than the similar energy between C=O of ith and NH of i+4th residue. However the fluctuation of the energy betewwn NH and water fluctuates more than the other energy. Even in some of the frames it touches zero (Figure 7.12). This is because in some frames none of the water molecules satisfy the criteria of H-bonding with NH. The energetics of peptide H-bonds have always been thought of as a very important criteria in helix formation right from the time when H-bonded structures of α-helix was proposed by Pauling and Corey [101]. After that, various approaches have been adopted to understand the relation between solvation and peptide folding [120]. Doruker et al. have shown that the effect of water on helices is highly residue specific [127]. Electrostatic solvation free energy calculations have been performed in the past to understand the role of

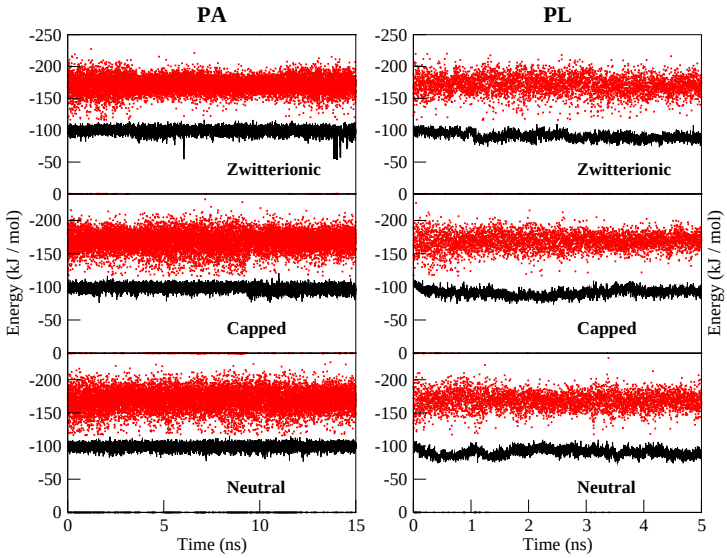

(a) **PA and PL**

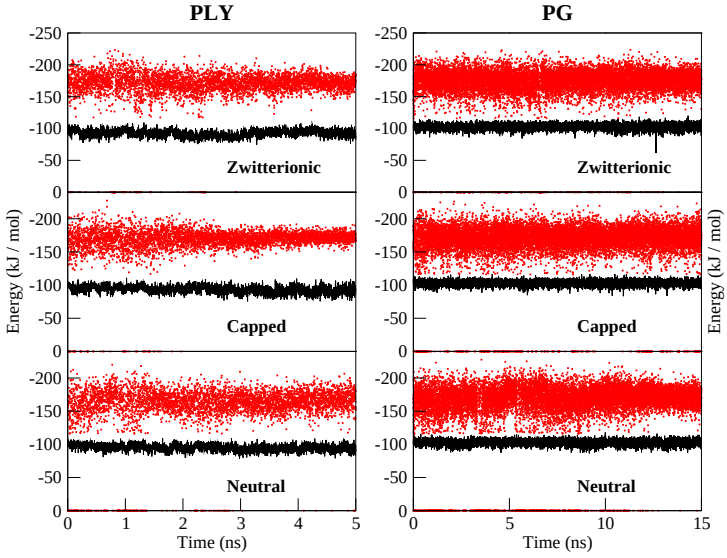

(b) **PLY and PG**

Figure 7.12: Electrostatic energy of interaction between backbone C=O and NH (black), and between NH and water (dotted red) with respect to time.

interaction between helical peptide groups and water in determining helix propensities [128, 129]. Here, we have taken a simple approach of calculating the electrostatic

potential energies for intra helical H-bonding interactions and interaction of helical backbone with water to understand the driving force for helix unwinding in water.

7.3.4 Distinction of the Helix Unwinding Sites

Calculation of the electrostatic energies show the possible driving factor for unwinding of the different helices but it does not clarify the unwinding of the different helices at different sites i.e., middle and terminals. RMSFs (Figure 7.6) for each variants have shown that fluctuation play a role to trigger the unwinding process. Still the question remains what is the extend of this fluctuation to dictate the process of unwinding sites. Therefore we have calculated the angle between two vectors, between C_α carbon of residue 15 and C_α carbon of residue 11 and the vector between C_α carbon of residue 15 and C_α carbon of residue 19, i.e., the vectors constitute the helical turn at the middle of the α-helical chain and plotted as function of time in Figure 7.13. All the systems in the plot show the starting angle of nearly 180° between the vectors, which is obvious as the starting structures are prefect α-helical. As the time increases the angle starts to fluctuate and in some cases moves quite far from linearity (i.e. 180°). We have already observed in the snapshots that the capped PA and PL helices seems to unwind from the middle of the α-helical chain and the neutral form from the terminals (Figures 7.1a and 7.1b). The zwitterionic form of these two helices were also observed to unwind from the terminals [115]. In Figure 7.13 we see that for PA, the angle fluctuation between the vectors are less for zwitterionic and neutral forms than the capped PA in the early stages. Further similar results for the three forms of the PL helices can be observed in Figure 7.13. For capped PA and PL angle diverts from linearity much faster than any other forms of the same peptide. Since

the capping has been done with -$NHCH_3$ at C-terminal and with -$COCH_3$ at the N terminal, it makes the helical chain uniform. Therefore, the C=O and NH groups of the terminals can also get involved in the H-bonding within the α-helical backbone which is not possible for the zwitterionic and neutral forms. Change in angle between the vectors to less than 180° for the capped forms of the helices indicates that the side-chains protruding out of the helical backbone come close to each other. Due to this a stabilizing non-bonded interaction is developed among the side chains. Being uniform, the capped helix have the possibility to unwind from any point of the helix. However the stabilization due to the non-bonded interactions among the side-chains coming close to each other drives the unwinding pathway from the middle of the helical chain. In this regard Sorin et al. [110], in their study with capped homopolymeric helices, have observed that unfolding of the helices initiates by breakage of helices into multiple helical segments. This non-bonded interaction is dominated by inter residual H-bonding among the side chain -NH_2 groups in all the forms of PLY helices (Figure 7.7). Due to higher fluctuations of helical backbone in some cases, mainly the capped from of PA, PL and all the forms of PLY, the long-range non-bonded interactions get favorable hence helices start to unwind from the middle.

We have proposed in our previous report [115] that it is the higher fluctuations of the terminal residues that trigger the unwinding of the zwitterionic helices from the terminals. However in Figure 7.6, the fluctuations can be observed to be higher for the terminal residues for all the helices studied in the first interval of time e.g., 0-5 ns for capped PA or 0-1 ns for capped PLY. Thus the factor of higher fluctuation of the terminal residues exists in all forms of the helices. In addition to this the stabilizing long-range non-bonded interactions among the side chains exits due to higher fluctuations of backbone. Either of these two become a dominating factor

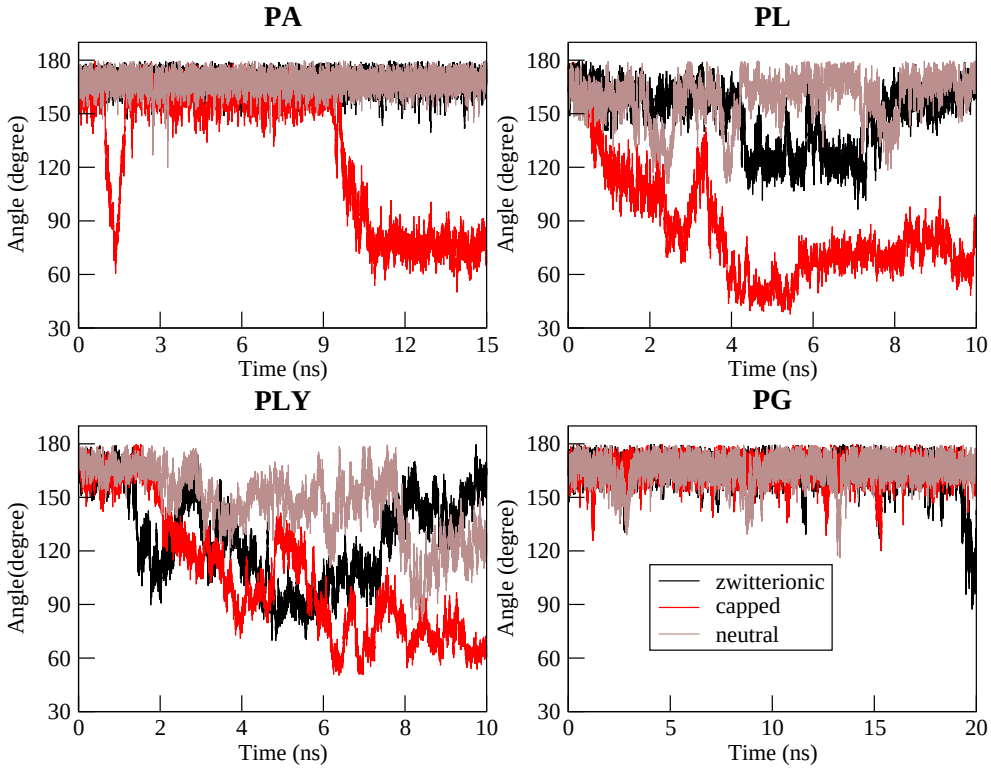

Figure 7.13: Angle between the two vectors as a function of time.

during the unwinding process. All the PG helices unwind from the terminals. Hence we can propose that the unwinding from middle for capped PA and PL helices is caused by more dominating stabilizing long-range non-bonded interactions among the side chains. That is the capped PA and PL helices starts to unwind from the terminals due to higher fluctuations of the terminal residues but then the stabilizing long-range non-bonded interactions among the side chains predominates and the helices unwind from the middle.

7.4 Conclusion

Classical molecular dynamics simulations of the various forms of α-helical PA, PL, PLY, and PG in water at 300 K shows sharp distinctions in their unwinding mechanisms. The distinctions in the unwinding mechanisms were extracted and analysed to understand their source. The neutral forms of PA and PL helices unwind from the terminals akin to their zwitterionic analogue. However, their capped forms unwind from the middle of the α-helical chain due to higher fluctuation in the backbone and favorable non-bonded interactions among the side chains. All the forms of the PLY helices show inter residual H-bonding among the side chain -NH_2 groups, which drives the unwinding of the PLY helices from the middle of the α-helical chain. Higher fluctuations of the terminal residues cause all the forms of PG helix to unwind from the terminals. No inter residual H-bonding exists among the side chain -COOH groups in any of the PG helices. Calculation of electrostatic interaction energy for the interaction between water and NH on peptide backbone show that the interaction with water is more stabilizing. In addition to the higher fluctuations of the terminal residues, the H-bonding interactions with water molecules are also a determining factor for the unwinding of α-helical homopolymeric peptides.

Though higher fluctuations of the terminal residues and H-bonding interactions with water are the key factors determining the unwinding mechanism, but stabilizing long-range non-bonded interactions may favour for the unwinding from middle. For example, the capped PA and PL helices, and all forms of the PLY helices start to unwind from the terminals due to higher fluctuations of the terminal residues but the unwinding is not relayed to the middle. Due to stabilizing long-range non-bonded interactions among the side chains they eventually unwind from the middle.

Similar results from multiple simulations signify that the mechanism of unwinding is statistically robust. Though the unwinding timescales in the multiple runs vary in 2-4 ns range, but the unwinding pathways are similar.

We have considered 30 amino acid long chains of the α-helix in all our simulations. Chain length is an important factor which may also dictate the unwinding mechanisms. Couch et al. have studied the helical contents of polyalanine peptides by varying the length of helix from 10 to 40 residues [130]. Increasing length of the chain also affects the flexibility of an α-helix [131]. Hence further understanding is needed for longer chain lengths helical peptides. Choe et al. have shown that bending modulus of helices is independent of the amino acid sequence [132]. The long chain simulations with explicit solvent are difficult taking all atomistic details into account, as the system size will be very large. For such simulations, coarse graining can be an option. Further all the PLY and PG simulations were performed taking side chains as -NH_2 and -COOH respectively. For more complete understanding, simulations of these systems needs to be performed at different protonated states . Also, the unwinding mechanisms of helices constructed of combination of amino acids needs to be understood on the basis of our finding.

In chapter 4 of part A, effect of hydrophilicity of surface on its wetting/dewetting is established. In the present chapter effect of hydrophobicity at the structural level is elucidated. The unwinding mechanisms of the different helices vary as a function of sidechain hydrophobicity. The effect of hydrophilicity/hydrophobicity at the structural level is further explored in biologically inspired systems in chapters 8 and 9 for phospholipids and sophorolipids.

[3]The results and figures are adapted from the publication P. R. Pandey and S. Roy, Distinctions in early stage unwinding mechanisms of zwitterionic, capped, and neutral forms of different -Helical homopolymeric peptides, The Journal of Physical Chemistry B, 2012, 116, 4731-4740.

Chapter 8

Head group mediated water insertion into DPPC Bilayer-Water Interface

8.1 Introduction

Model atomistic protrusions depicted in chapter 5 of part A are structurally motivated from lipid bilayer-water interface. Extending the study on structure and dynamics of water near model protrusions, in the present chapter we move close to real system, and have studied phospholipid bilayer-water interface. The model protrusions (chapter 5) are constructed of hydrophobic and hydrophilic blocks with water on top of the hydrophilic blocks. In case of phospholipid bilayer-water interface the hydrophilic head groups point towards water and hydrophobic tails cluster near each other.

S.J. Singer and G.L. Nicolson proposed in their famous fluid mosaic model [85] of the biological membranes, that, it contains oriented globular proteins and lipids.

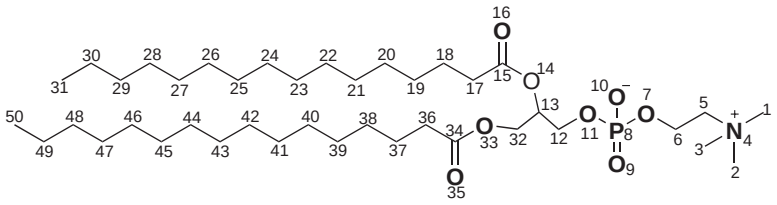

Figure 8.1: Stucture of DPPC molecule with atom numbering as used in the text.

Water is present near both sides of the bilayer in the extracellular and intracellular fluid. Lipid molecules contain polar head groups and non polar hydrocarbon tails. They assemble to form a lipid bilayer. Being polar, the head groups are hydrophilic in nature and point towards the extracellular fluid and towards cytoplasm. Tails of the two layers face each other and form a hydrophobic region.

Phospholipids are the major kind of lipid molecules present in the biological systems. Various kinds of phospholipids present in biological system are phosphatidylserine, phosphatidylethanolamine and phosphatidylcholine. They differ in the structure of their head groups. 1,2-dipalmitoyl-sn-phosphocholine (DPPC, Figure 8.1) contains choline group at its head group. Since phospholipids are the building blocks of biological membranes, their structure and dynamics have been studied extensively [93–98]. In these experimental studies X-ray crystallography and NMR have largely been used and proved to be helpful techniques for elucidating the structure of various kinds of crystalline and amorphous phospholipids. Though this is a subject of interest for almost two decades but interesting questions still remain unsolved. How the head group of the lipid molecules in the bilayer interact with water is one among them? Or in other words, how at the lipid-water interface the hydrophilic head group of lipid molecules interact with adjacent water molecules? In this regard, NMR [133–137] and neutron scattering [138–140] experiments have shown that water molecules permeate the bilayer interface with a steeply decreasing concentration as they proceeds

towards the inner hydrophobic region of the bilayer. Studies with other experimental techniques (e.g. FTIR) have also provided similar insight [141].

For quantitative understanding of the interactions of water molecules with polar head groups at the lipid-water interface at molecular level, molecular dynamics (MD) simulations have been proved to be useful. MD simulations have also enforced the facts, just like experimental studies, that majority of the water molecules residing in the polar region of the membrane are hydrogen (H-) bonded to the phosphate groups, with a smaller fraction binding to the carbonyl groups located deeper in the bilayer, but with more extensive structural details [142–146]. One of the initial reports that presented the study of lipid-water interface on dilauroylphosphatidylethanolamine lipid bilayer with MD simulations was by Damodaran et.al. [147]. They calculated velocity autocorrelation function for both lipid and water, and also orientational correlation function for water to understand dynamics of the system and diffusive properties of the system respectively. MD simulations have also shown that organization of water molecules at the lipid-water interface depends upon the type of lipid head group [148].

The most critical component of any MD simulation is the force field used, which consists of a set of mathematical functions and parameters that describes the bonded and nonbonded interactions between the particles (atoms, united atoms) of the system under study. Recently Kukol in his study [149] has proposed a model for DPPC, which reproduces the area per lipid of the lipid bilayer within 3% error without the assumption of a constant surface area or the inclusion of surface pressure as provided by experimental study [150, 151]. In Kukol's model, modification of the original model included in GROMOS96 53a6 [29] force field has been done with two changes in the topology. First, the partial charges on the lipid head group due to Chiu et.al.

[152] was implemented, with a subdivision into four charge groups as suggested by Chandrasekhar et.al. [153]. Second, ester-carbonyl carbon atom type was changed to "CHO" from "C", resulting in increase in the van-der Waals radius for ester-carbonyl carbon atom to 0.664 nm as opposed to 0.336 nm before. These changes resulted into better values for area per lipid and also increased the penetration of water into lipid bilayer headgroup region.

Gierula et.al. have studied the H-bonding dynamics between water and dimyristoylphosphatidylcholine (DMPC) using MD simulation [154]. In their study they have observed that among all the DMPC oxygens, the largest ordering of water is around non-ester phosphate oxygen but to a much lesser extent around ester-carbonyl oxygens. Dynamics of water molecules at the fully hydrated 1-palmitoyl-2-oleoyl-phosphatidylcholine (POPC), 1-palmitoyl-2-oleoyl-phosphatidyl ethanolamine (POPE), and 1-palmitoyl-2-oleoyl-phosphatidylglycerol (POPG) bilayers and the effect of head groups on this motion has been studied by Murzyn et.al. [155]. They have shown that head group plays an important role in dynamics of water molecules at the interface. Inter- and intra-lipid interactions were studied by Zhao et.al. for anionic palmitoyloleoylphosphatidylglycerol (POPG) lipid [156].

Recent experimental study by Sovago et.al. [157] showed that for lipid monolayers of lauric acid (LA), octadecyl trimethyl ammonium bromide (OTAB), 1,2-Myristoyl-sn-glycerol-3-phosphoserine (DMPS), DPPC, 1,2-Dipalmitoyl-sn-Glycero-3-Phosphoethanolamine (DPPE), and 1,2-Dipamitoyl-3-trimethyl ammonium-propane (DPTAP), buried water molecules exist between the lipid headgroups and their alkyl tail. Also, they have shown that these water molecules have a weaker H-bond network than that of bulk water. As water penetrated much deeper in the bilayer has been proved by experiment and theory [149], in this chapter, we have studied for the

first time, to the best of our knowledge, the mechanism of further insertion of water molecules, which crosses through the head group region of DPPC bilayer and remain in between the head and tail of lipid molecules. We have also studied the change in hydrogen bonding environment, using the modified topology proposed by Kukol, around different electronegative groups of DPPC molecules. This has been studied by clustering of water molecules and also the H-bonding of the water molecules attached to non-ester carbonyl oxygens, phosphoryl oxygens and NMe_3 of the lipid molecules. We have shown that the insertion of these water molecules inside the bilayer occurs with the help of NMe_3 group present at the head group of DPPC. All the structural details obtained points to the mechanism as proposed in this work.

8.2 Computational methods

Initial structure of the DPPC bilayer and water system was taken from last frame of the 40 ns run from Kukol's work. Each DPPC molecule was taken as united atom model with 50 atoms as discussed by Kukol. However, all atomistic model of DPPC contains total of 130 atoms. Choice of united atom model was made as it is the best known model at this stage for DPPC and is even better than any other atomistic models, and certainly provides faster and longer time scale simulation, hence better statistics. The initial coordinates consisted of DPPC bilayer having 128 DPPC molecules hydrated with 3655 water molecules (Figure 8.2). The previous model of DPPC based on GROMOS-53a6 has failed to reproduce the experimental data with high accuracy, which has already been shown in previous studies [158]. Force field by Berger et.al. [159–161] has also been used for DPPC but without much success in the case of membrane protein. In this work, DPPC bilayer was simulated for 40 ns using

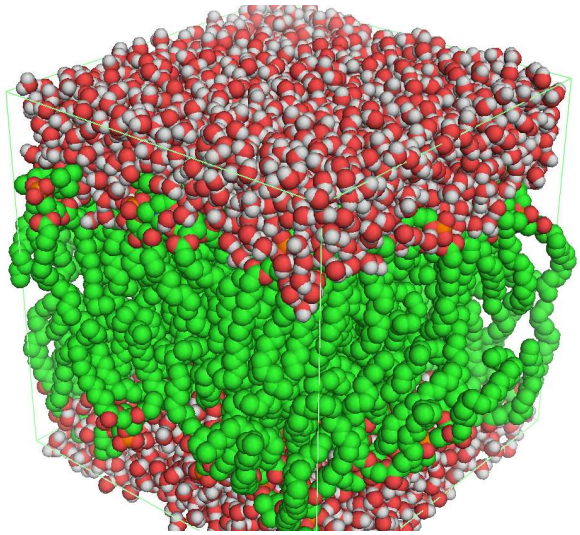

Figure 8.2: DPPC-water interface.

GROMACS 4.0.7 [41, 42] package and GROMOS-53a6 [29] force field, with slightly modified topology proposed by Kukol [149], which happens to be the best parameters available for united atom DPPC system and tested for proteins and bilayer assemblies. SPC water model was considered for the simulation. NPT ensemble and periodic boundary conditions were used. Temperature was kept constant at 325 K using v-rescale thermostat for the whole simulation time. At this temperature DPPC exists in liquid crystalline state as its phase transition temperature is 314.5 K [162, 163]. Semi-isotropic pressure coupling was applied using Berendsen barostat [38] with separate coupling to xy-plane and the z-direction (the bilayer normal). Pressure coupling time constant was 2.0 ps in order to maintain a constant pressure of 1.0 bar. For Lennard-Jones interaction a cutoff at 1.4 nm was applied, electrostatic interactions were taken care of with particle mesh Ewald (PME) [125] method and a real space cutoff of 0.9 nm. Electrostatic interactions were treated with the PME method, which did not introduce artificial ordering like reaction field cutoff methods. The lipid molecule

bonds were constrained with the LINCS algorithm. All these parameters were in agreement with Kukol's work. The MD simulation for 40 ns was carried out and trajectory was written every 0.5 ps. The trajectory was further analyzed to calculate radial distribution functions between different atoms of DPPC and water. Partial density profiles are reported as 2-dimensional plot where we have considered the interface along z axis. Dihedral distributions for few specific dihedrals are reported to illustrate the mechanism of water insertion into the bilayer. All other non-convetional analysis methods are described along with the results and discussions.

8.3 Results and discussion

8.3.1 Area per lipid

Area per lipid is the most widely used property for characterization of lipid bilayers as it can also be measured by experiments. Also, area per lipid is related to various other properties like lateral diffusion, membrane elasticity etc. In the present chapter lipid bilayer was along the Z-axis. So area per lipid was calculated from the lengths of box in X and Y direction by the following equation

$$\textbf{area per lipid} = \frac{\textbf{(box length in X)(box length in Y)}}{\textbf{no of lipids in one lamella of bilayer (i.e. 64)}} \tag{8.1}$$

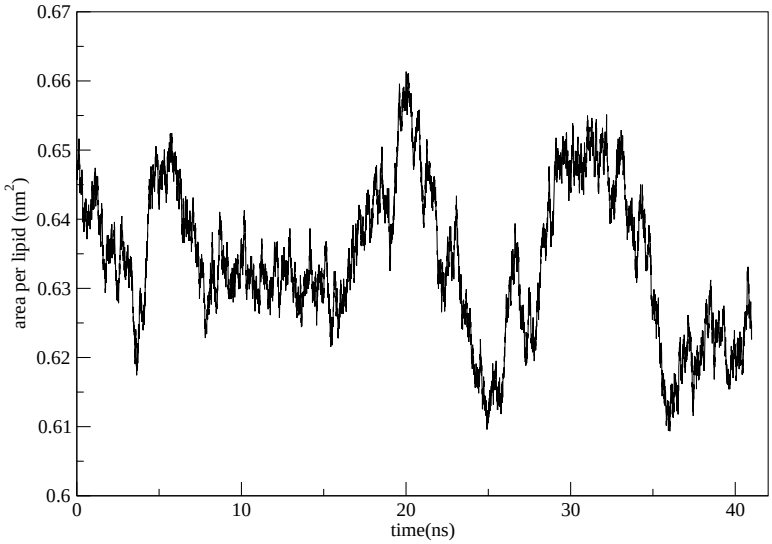

Figure 8.3: Area per lipid.

Plot of area per lipid as a function of time for total 40 ns is shown in Figure 8.3. Trend of the area per lipid was similar as reported in Kukol's work. Average area per lipid for the 40 ns trajectory was calculated to be 0.64063 $\pm$ 0.02 nm^2. This value is within a range of 3% of the experimental value of 0.64 nm^2. This provides the validation of the force field and also shows the reproducibility of our simulation. We have also performed self assembly simulation starting from randomly oriented DPPC in water, using the same force field, and we have obtained the same result for area per lipid after self assembly.

8.3.2 Partial density profile

We have plotted the partial density profile for DPPC, water and various atoms present at the head and neck region of DPPC versus length of simulation box in Z-direction in Figure 8.4. Interfaces between DPPC and water are clearly visible in the plot,

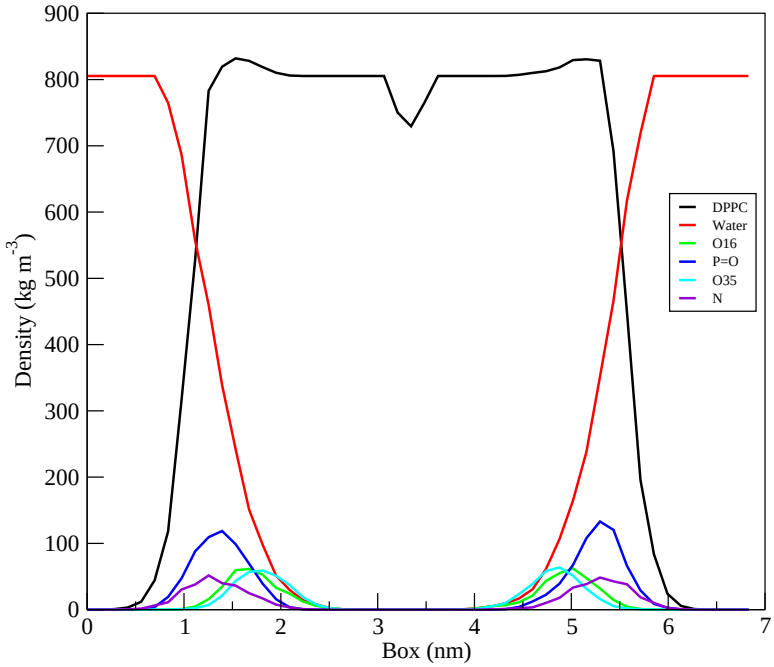

Figure 8.4: Partial density profile.

one from 0.5 nm to 2.5 nm and the other from 4 nm to 6 nm approximately. A small dip in the plot of DPPC (at around 3.5 nm) shows the intersection between the hydrophobic regions of the two monolayers. Peak of nitrogen (N) appears nearest to the water molecules at the interface. This shows that N or NMe_3 group faces most of the bulk of water, which is quite obvious. For phosphoryl group (P=O) both the non-ester oxygens of P=O were treated equivalently. Partial density of P=O is highest amongst all the atoms in head and neck region of DPPC. This is possibly because we have treated both the phosphoryl oxygens as equivalent atoms. Difference between the positions of the peaks of N and P=O is negligible. But, N being the outmost atom, we expect the peak of N in the partial density plot to be present more towards the bulk water at bilayer-water interface. This issue has been clarified

and discussed later. The position of peak of O16 (atom number used as in Figure 8.1) appears more towards the inside of bilayer than N and P=O. The position of the peak of O35 appears more towards the tail region of the bilayer than the others. O35 instead of being present at a difference of one carbon atom (C32) than O16 from the head group, partial density plot shows that O35 is still present at the water-DPPC interface region. This shows that water penetrates deep into the DPPC bilayer.

8.3.3 Environment of head group (NMe_3) and its neighboring group (P=O)

Clustering of water molecules

Figure 8.5 shows the radial distribution functions (RDFs) of oxygen atoms of water molecules with carbon atoms (C15,C34) of carbonyl groups, phosphorus (P) and nitrogen (N) atoms present in DPPC. Thus the RDFs represent the clustering of water molecules around these atoms in DPPC. Integration of the first RDF peak shows that clustering of water molecules is largest around N (as integration of its first peak has a value of 13.64), which is expected as N is located at the external part of the head group of DPPC. As a result of which it sees most of the bulk of water.

The height of first RDF peaks for P and C15 with oxygen of water molecules appear at similar values. Whereas, integration of the first peaks, which is the measure of average number of water molecules present in the first solvation shell is 3.27 for P and 1.87 for C15. This shows that considerable number of water molecules penetrated into the bilayer and there is a rapid decrease in water concentration from NMe_3 to

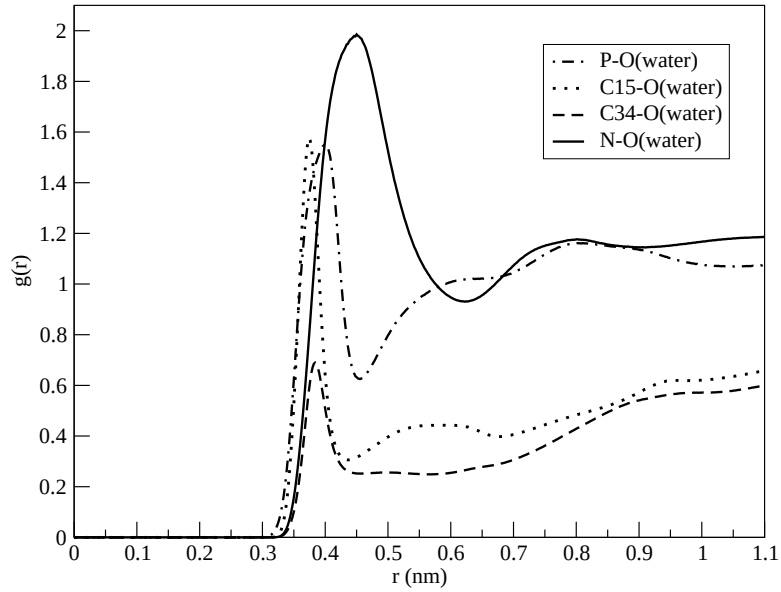

Figure 8.5: RDFs for clustering of oxygens (water) with head group nitrogen, phosphorous and carbonyl carbons.

C15. This is also visible from the partial density profile, where we have observed that O35, despite being situated at the beginning of the tail of DPPC, is present in the interfacial region. The peak of C34 is smallest of all and solvated by only average of 1.02 water molecules. This is because C34 is located deeper inside the bilayer where the hydrophobic region starts to form and is also at a difference of one carbon atom (C32) with respect to C15. Thus, clustering of water molecules around various atoms in the head group and neck region is in the following order as interpreted from the values of the number of water molecules present in the first solvation shell.

N >P >C15 >C34

The size of the solvation shells around these atoms (as interpreted from the 1st minima of the peaks) are in the following order

N >P ≈ C15 >C34

Water environment around O16 (carbonyl oxygen), P=O (non-ester oxygen of phosphorous), O35 (carbonyl oxygen)

Gierula et.al. in their study suggested that largest ordering of water in DMPC bilayer is around phosphoryl non ester oxygens (P=O). They observed less ordering around non ester carbonyl oxygens. Also, Lopez et.al. [145] have obtained similar results with DMPC from a longer trajectory. We have plotted RDFs between hydrogen atoms of water with non ester oxygens of P=O (O9 and O10), O35 and O16 (Figure 8.6a). Height of the first peak in the RDF plot is maximum for O16, suggests, ordering of more number of water molecules around O16 than O9 and O10 (non-ester oxygens of phosphorous atom). This is in direct contradiction to the results obtained by Gierula et.al. First peak of O9 and O10 of phosphorous is smaller than O16, and hence, suggests a less ordering of water molecules around P=O than O16. As expected, number of water molecules present in the 1st solvation shell of O35 is the least among others present at the interface. It appears to be obvious as O35 is located near the starting of the tail and is at a difference of one carbon atom (C32) with respect to O16 from the head group region. Also the peak integrations indicate the same fact. Integration of first RDF peaks for O9+O10, O16 and O35 are 1.04, 1.49 and 0.61 respectively.

Although, we have observed and has also been proposed by Kukol [149] that water penetrates considerably into the bilayer-water interface region, the higher number of water molecules near O16 than O9+O10 (non-ester oxygen of phosphorous) is quite interesting. A question arises that how much water molecules bypass the non-ester oxygens of phosphorous and take part in the solvation shell of O16 which is located

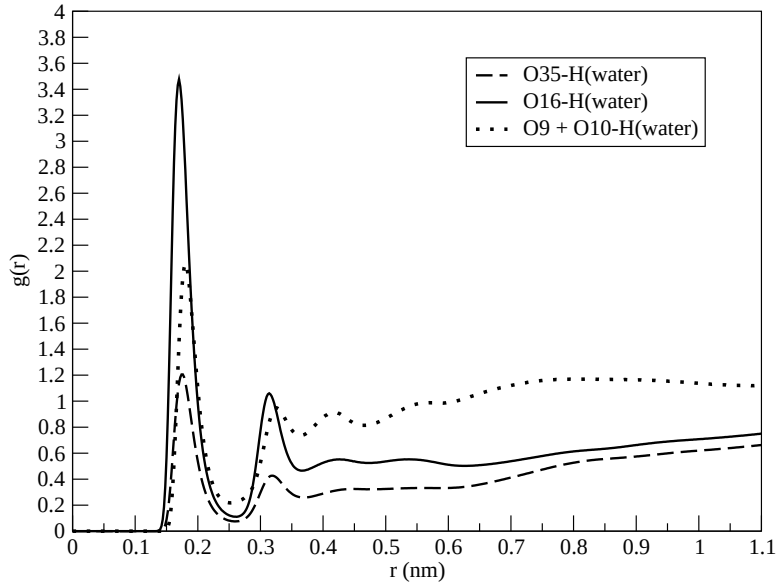

(a)

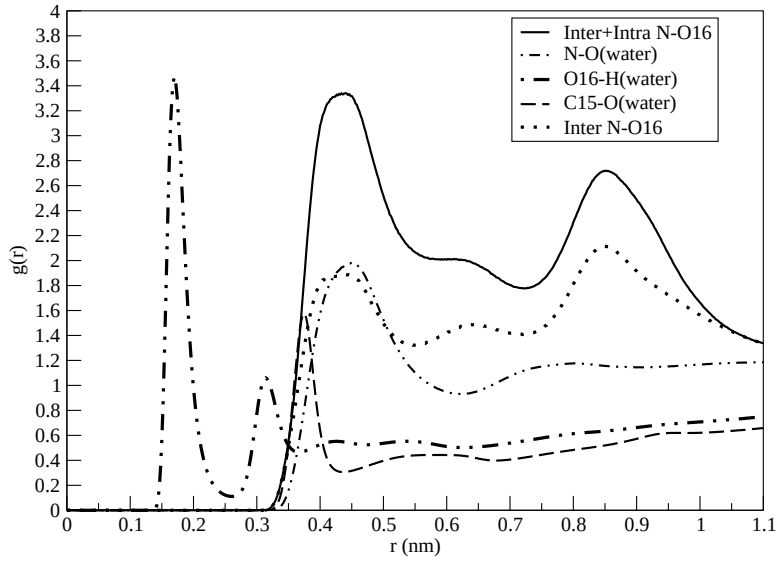

(b)

Figure 8.6: (a) RDFs between carbonyl oxygens and non-ester oxygens of phosphorous with hydrogen of water molecules. (b) RDFs between nitrogen-O16, N-O (water), O16-H (water) and carbonyl C(C15)-O (water)

deeper inside the bilayer than the non-ester oxygens of phosphorous? Since, P=O sees more of the interfacial water as compared to O16, hence water is expected to be more around P=O as compared to O16, as observed by Gierula et.al. for DMPC. Thus, the question is why do we get a higher first peak for O16 than P=O in the RDF plot?

To address this issue and find the mechanism of water insertion deep inside the bilayer, we have compared the RDF plots between N and O16 (combined intermolecular and intramolecular (inter+intra) RDF and only intermolecular (inter) RDF) with RDFs between N and water O (N-O_{water}), O16 and water H (O16-H_{water}) and C15 and water O (C15-O_{water}) in Figure 8.6b. We can readily observe that the minimum of first RDF peak of N and water O appears at a similar distance as that of inter+intra and only inter RDF plot between N and O16. It shows that the solvation shell of O16 merges with clustering shell of NMe_3 group present in the same molecule or on a neighbouring molecule. Similarly, minimum of first peak between C15 (carbonyl carbon) and water O appears within the first peak of N and O16. This shows that size of clustering shell of C15 is within the distance of closeness of N and O16 irrespective of whether they belong to the same DPPC molecule (intramolecular) or to neighbouring DPPC molecule (intermolecular). Thus, it appears that the solvation shell of O16, which is attached to C15, merges with the first solvation shell of NMe_3 group. The peaks with respect to N appear at higher distance than O16 peak because N is surrounded by three -CH_3 (Me_3) groups, and hence water molecules can arrange themselves just outside the -CH_3 groups. Similar is the case with C15, where C is attached with O16 so water molecules arrange around O16. Whereas O16 is naked and directly sees water without any intervening group. At a first intuition it might look unusual that water molecules arrange around hydrophobic -CH_3 groups, but ac-

tually it is rather common. Nitrogen being positively charged (in DPPC) attracts the polar water molecules towards itself. The Coulombic attraction between N and water molecules outweighs the hydrophobic mismatch between -CH_3 and water. Lum et.al. [164] and Chandler et.al. [165] have calculated the hydrophobic interactions between solute and water. Also Godawat et.al. have shown the density fluctuations at the interface of water and a range of hydrophilic and hydrophobic solute [166]. Integration of the peaks also show that N has a larger first solvation shell than O16.

Revisiting our question that why first RDF peak is higher for O16 than P=O in Figure 8.6a, it can be suggested that, since first solvation shell of C15 (and hence O16) merges with first solvation shell of NMe_3(Figure 8.6b), also we have seen that clustering of water around N is the highest (Figure 8.5), it is possible that O16 shares the solvation environment of NMe_3 group in certain intervals. This possibility can only be true if the NMe_3 group periodically bends towards O16 and as a result of which O16 shares the solvating water molecules of NMe_3. Dihedral bending of NMe_3 is represented by the dihedral angle distribution plot of N-C5-C6-O7 sampled from 40 ns trajectory in Figure 8.7a, where C5 and C6 are the connecting methyl groups between head group N and ester oxygen of phosphoryl group. Two peaks in the plot suggests two conformations of NMe_3, one of which corresponding to towards O16 and the other away from it. Krishnamurty et.al. [167] have shown using density functional theory (DFT) calculations that, for DMPC in the lowest energy conformation head group (choline group) is bent towards carbonyl in the neck region. Also, it has been proposed previously [168–172] that the bent head group configuration should minimize the intramolecular electrostatic interaction in the polar region of phospholipids. In other words, the internal electrostatic energy resulting from repulsion between the phosphoryl group and carbonyl oxygen is minimized by attraction between choline

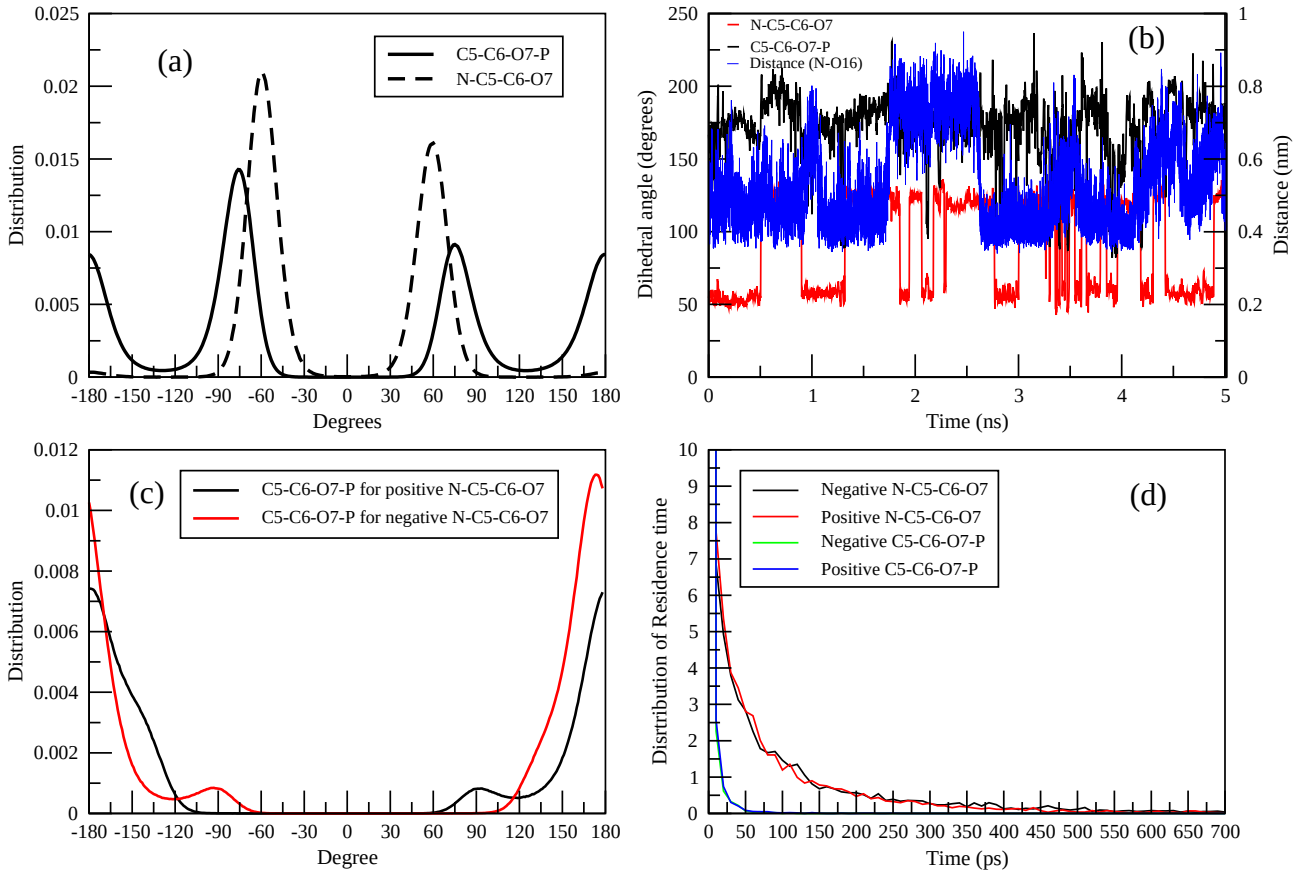

Figure 8.7: (a) Dihedral angle distribution N-C5-C6-O7 and C5-C6-O7-P. (b) Dihedral angles (N-C5-C6-O7 and C5-C6-O7-P) and distance between N and O16 as function of time. (c) Conditional probability distribution of dihedral angle C5-C6-O7-P when N-C5-C6-O7 dihedral angle samples positive and negative angles. (d) Distribution of dihedral residence time for N-C5-C6-O7 and C5-C6-O7-P for both in positive or negative directions.

and carbonyl groups. In Figure 8.6a we have also observed that first RDF peak of P=O (non-ester oxygen of phosphorous) with water H is in the region of first RDF peak of O16 with water H. Hence, from this we can also say that O16 (carbonyl oxygen near to the phosphorous) shares the solvation shell with P=O. Leekumjorn et.al. have shown by varying the percentage of DPPE in DPPC that amine group

in DPPE strongly interacts with phosphoryl and carbonyl groups through intra or intermolecular H-bonding [173]. Also surface sum-frequency generation spectroscopy study of buried water molecules inside phospholipid membranes by Sovago et.al. [157] suggested that water molecules interact with the zwitterionic lipid DPPC with its O-H group pointing towards bulk water and is positioned just below the choline group. This leads to the fact that the interfacial water may have a variety of hydrogen bonding environment. This fact is further confirmed by IR spectroscopic study of various kinds of lipids present in the biological system by Hubner et.al. [174].

Further, in RDF plots between N and O16 (inter+intra and inter) sampled for 40 ns trajectory (Figure 8.6b) we have observed two peaks - one large peak at around 0.4 nm, and another peak at around 0.85 nm. The origin of the predominant two peaks are due to the sampling of dihedral (N-C5-C6-O7) at different conformations. There is a second dihedral C5-C6-O7-P which may also have some effect on the bending of the NMe_3 group towards the carbonyl oxygen (O16). The dihedral angle distribution for the above dihedral angles are plotted in the same figure (Figure 8.7a). We observe that C5-C6-O7-P dihedral is sampling much more angular space than N-C5-C6-O7. To understand the time span of each conformation produced by the combination of these two dihedrals (N-C5-C6-O7 and C5-C6-O7-P) we have plotted the dihedral angles for single DPPC molecule as a function of time in Figure 8.7b. In the same figure we have also depicted the distance between N and O16 (carbonyl oxygen). From the figure it is observed that indeed the dihedral related to the head group samples only two major angles and it is spending maximum of 0.5 ns in each conformation. Whereas the other dihedral (C5-C6-O7-P) samples angles from -180° to 180° with much rapid motion than the other. Therefore, the distance between N and O16 changes mainly due to the head group dihedral motion assisted by the much

frequent another dihedral angle C5-C6-O7-P motion. Taking these observations for one molecule into account distributions of C5-C6-O7-P dihedral were plotted (Figure 8.7c) to understand the motion of C5-C6-O7-P dihedral with respect to N-C5-C6-O7 dihedral under two conditions, first when N-C5-C6-O7 dihedral lies between -180° to 0° (i.e., negative) and second when it lies between 0° to 180° (i.e., positive). These dihedral distributions show that C5-C6-O7-P dihedral samples dihedral angles from -180° to 180° in both positive and negative regions of N-C5-C6-O7 dihedral. It is also interesting to note that C5-C6-O7-P dihedral distribution has a small peak around 90° when N-C5-C6-O7 dihedral lies in the positive region and at -90° when N-C5-C6-O7 dihedral lies in the negative region. This shows the selectivity of a conformation. In Figure 8.7b we have observed that N-C5-C6-O7 dihedral stays in the positive or negative region maximum for 0.5 ns for one molecule. Whereas in this time C5-C6-O7-P dihedral fluctuates very frequently and aquires a larger space. To make this fact statistically more acceptable, we have plotted the distribution of residence time of both the dihedrals (N-C5-C6-O7 and C5-C6-O7-P) in the positive and negative space in Figure 8.7d. We recorded the time for which a dihedral stays in one direction for all DPPC molecules and counted how many dihedrals stay in a particular direction for a particular span of time. Finally, we have converted it into a distribution which is normalised by number of frames and number of DPPC molecules. It is clearly visible from the plot that N-C5-C6-O7 dihedral distribution decays much rapidly than C5-C6-O7-P dihedral. That is N-C5-C6-O7 dihedral stays in either positive or negative direction for much longer time than C5-C6-O7-P dihedral. As a result of these observations, we predict that the distances obtained for different dihedral and dihedral angles conformations correspond to closest distance of approach of N toward O16 of the same molecule. This means that the second peak of RDF plot between N

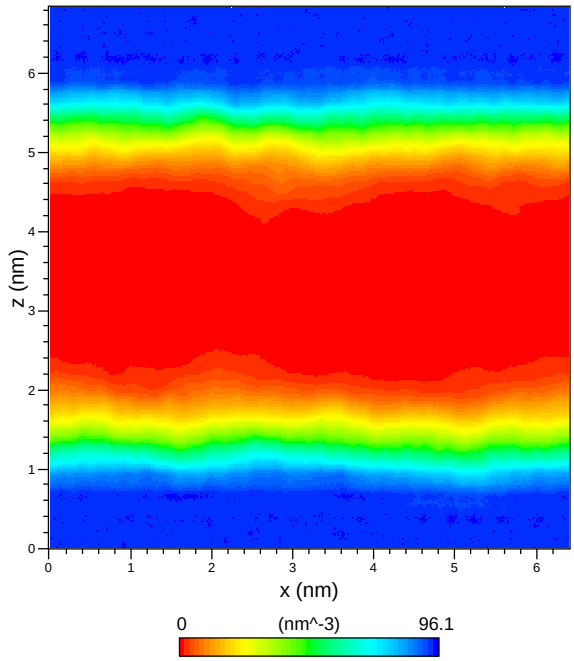

Figure 8.8: Two dimensional density map of DPPC-water interface in XZ-plane.

and O16 in Figure 8.6b has contribution from both intramolecular and intermolecular distances between them. That is at the head group region of DPPC bilayer N and O16 of same molecule and also of the neighboring molecules come close to each other. As a result of which O16 not only sees the solvation sphere of N of same DPPC molecule, but also, the solvation sphere of N of neighboring DPPC molecules. This fact also contributes to the higher RDF peak of O16 with water H than P=O with water H in Figure 8.6a. This results in larger solvation shell for O16.

A two dimensional density map of DPPC and water (Figure 8.8) shows that the distribution of water is continuous at the interface region from the 40 ns simulation. This continuous environment of water indicates the mobile nature of the water molecules even deeper in the interface. Bending of the head group towards inside the bilayer is further proved by plotting the angle between O7-N bond vector and

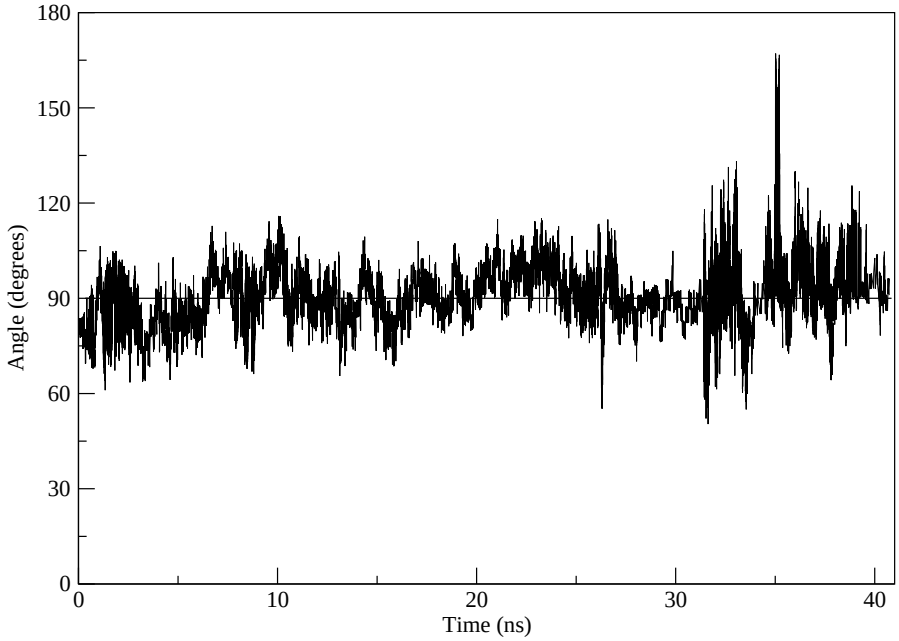

Figure 8.9: Angle between O7-N vector and z-axis of the box with time (90° angle is shown by a horizontal line).

z-axis with time (Figure 8.9). When the angle is 90°, i.e. vector is perpendicular to the z-axis, it is parallel to the interface. Also angle greater than 90° means the vector and hence the NMe_3 group is inside the bilayer. In Figure 8.9 we observe that the concerned angle is greater than 90° (shown by a straight line) for a considerable amount of time. This is also a very firm proof of bending of NMe_3 group inside the bilayer.

In Figure 8.10, distribution of the common water molecules between the solvation shell of NMe_3 and O16 has been depicted. The distribution is made using a small part of the trajectory (25 ns to 30 ns) and was normalized with respect to number of frames in that time. From each frame number of common water molecules between

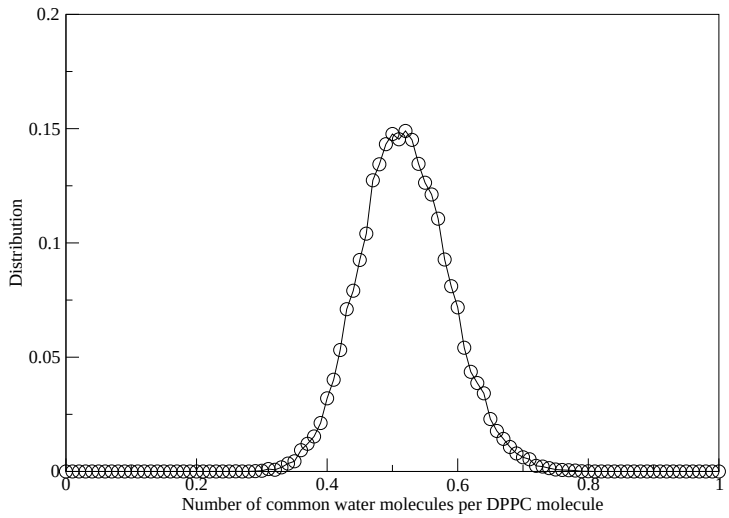

Figure 8.10: Distribution of the number of common water molecules between the solvation shells of N and O16.

the two solvation shells were counted and divided by the total number of DPPC i.e. 128 in the system. Then the distribution of this number of common water molecules per DPPC was plotted. The plot shows one broad peak at 0.5, which proves the presence of 0.5 common water molecules between the solvation shell of NMe_3 and O16 molecules. The plot acts as a proof of our postulate for mechanism of penetration of water molecules into the bilayer from bulk. In addition to the water insertion deep into the bilayer we have also observed the bridging H-bonded water molecules between O16 and non-ester oxygen attached to the phosphorus atom. These water molecules simultaneously form H-bond to both O16 and P=O. The average number of such H-bonds in each frame is 15.6. Thus out of 128 DPPC molecules present in the system around 16 DPPC molecules are involved in such H-bonding. To calculate this number we counted the number of water molecules appearing within H-bonding distance (0.28 nm observed from Figure 8.6a) of O16 and P=O for each DPPC molecule

in each frame. From this we counted the number of water molecules common to both O16 and P=O and divided it by number of frames. The number appears to be low with respect to total number of DPPC molecules present in the system.

It has been mentioned in the text that various experimental studies have shown that water has different H-bonding environment around the head group of lipid bilayer. Mean square displacement (MSD) of different water molecules, present initially in different regions, as a function of time has been checked. For this plot we first recorded the water molecule present near carbonyl group (C=O), P=O and in bulk separately. Then we tracked these water molecules in its Z-direction for 500 ps of the trajectory and plotted MSD in Z-direction, XY-plane and XYZ-directions separately, for those who stayed in their initial region with respect to Z-axis (i.e., the axis along interface)for more that 200 ps. Finally, we have reported a mean MSD plot out of these various MSDs plotted for the movement of water in XY-plane and all XYZ-directions in Figure 8.11. In the two plots, namely, average MSD of water in XY-plane (Figure 8.11a) and in all XYZ-directions (Figure 8.11b) a clear distinction between the three regions is visible. This indicates different environments of water and its confinement near the head group region and also after entering the bilayer. The values of diffusion constants calculated from MSD are reported in Table 8.1. Dynamics and entropy of such water molecules have been studied recently by Debnath et.al. [175] which supports our finding.

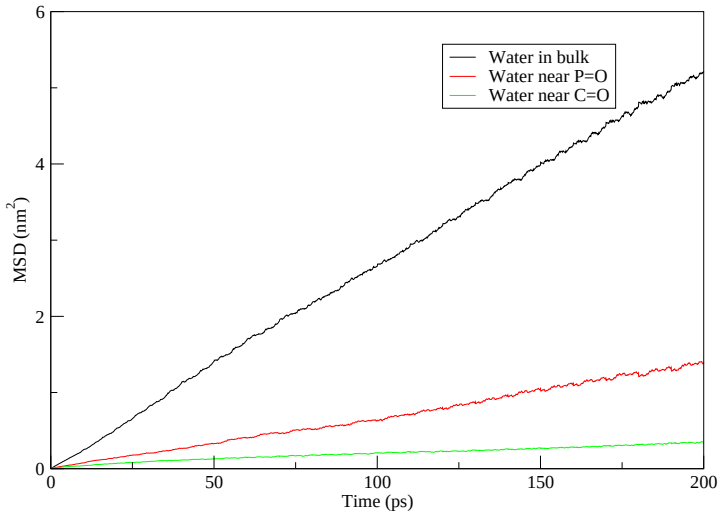

(a)

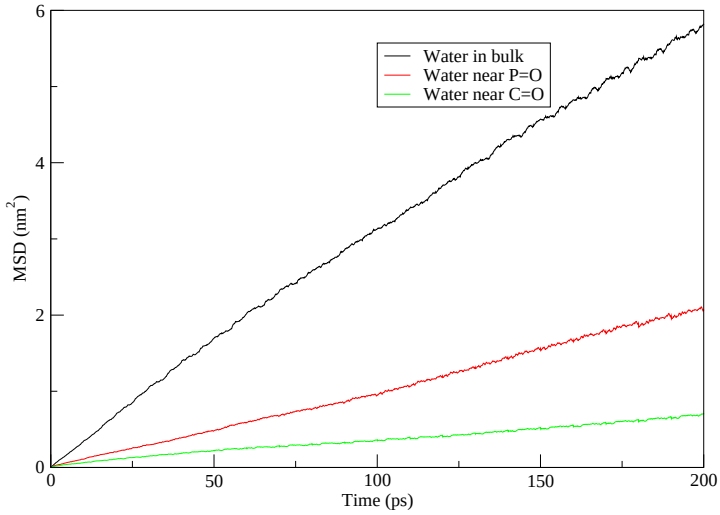

(b)

Figure 8.11: (a) MSD plot for water molecules in all regions along XY-plane. (b) MSD plot for water molecules in all regions along all XYZ-directions.

Table 8.1: Diffusion constants from average MSD plot for movement of water in XY-plane only and all XYZ-directions.

Region	**XYZ-directions(cm^2/sec)**	**XY-plane (cm^2/sec)**
C=O	$0.672 \pm 0.117 \times 10^{-5}$	$0.294 \pm 0.056 \times 10^{-5}$
P=O	$1.706 \pm 0.201 \times 10^{-5}$	$1.346 \pm 0.169 \times 10^{-5}$
Bulk	$4.703 \pm 0.590 \times 10^{-5}$	$8.977 \pm 0.599 \times 10^{-5}$

8.4 Conclusion

Molecular dynamics simulation for 40 ns was performed using GROMOS96 53a6 force field parameters but with modified topology as suggested by Kukol [149] on DPPC-water bilayer system. The simulations provided area per lipid value for DPPC in 3% error range from experimental values. Better match to the experimental area per lipid leads to the penetration of water molecules deep into the bilayer giving us the scope to unveil the mechanism of water insertion into the bilayer. We have observed from our study that the NMe_3 group at the head group of DPPC moves inside and outside of the bilayer. Density plots shows that water is distributed in a continuous fashion at the bilayer-water interface and water penetrates deep into the bilayer upto the starting of the hydrophobic tail of DPPC molecules. Water keeps moving from the bilayer-water interface region to bulk water and vice-versa. Due to this it might be possible that during the process of insertion of the head group, water molecules clustered around NMe_3 group enter into the deep interfacial region. Taking this as a postulate we propose, that as a result of bending, NMe_3 group acts as water carrier, and pump in and out water molecules in the interfacial region of the bilayer. The mechanism is shown in the cartoon (Figure 8.12) which is drawn from a snapshot taken from the simulation. The cartoon depicts the mechanism how the head group

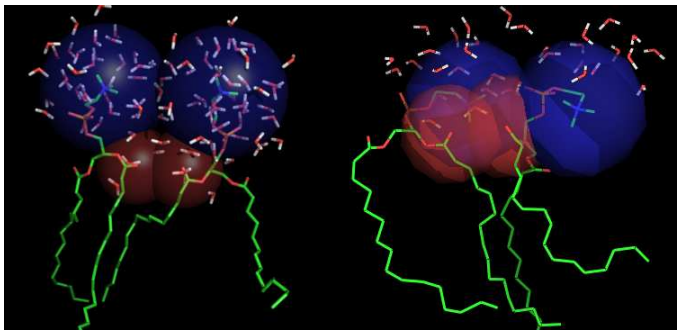

Figure 8.12: Cartoon depicting the overlap of the solvation shells of NMe_3 and O16. Blue and red spheres represent the solvation shells of N and O16 respectively.

bends inside the bilayer interface and overlaps with the solvation shell of carbonyl oxygen (O16). NMe_3 group bends inside the bilayer with water molecules solvating it. At the inside conformation of NMe_3 group solvation shells of NMe_3 and O16 merge. There is a possibility of exchange of water molecules inside the bilayer-water interface with the solvation shell of head group atoms, i.e., water molecules clustering around NMe_3 group get hydrogen bonded to O16 or O9 and O10. This exchange is possible because around NMe_3 group, water molecules are clustered outside the methyl groups and hence in addition to the attraction with N due to its positive charge, there exists a hydrophobic mismatch with the methyl groups. Whereas, when the water molecules approach near to O16 or O9 or O10 it sees only bare oxygen and involve in H-bonding with it. This exchange is not necessarily between solvation shells of NMe_3 and O16 of same molecule, but exchange between neighbouring molecules is also possible. Complex motion of proteins or lipids is strongly affected by the amount of solvent interacting with them. Our mechanism may help to verify how much water is interacting during its entry into the bilayer mediated by head group. Hydration at protein lipid interface is required for enzymatic activity, therefore, effect of water on the enzymatic activity might be dependent on the amount of water present at the

interface, which can be verified with our mechanism. In addition to the mechanism proposed, observation of bridging H-bonding water molecules points to the various H-bonding environment in the head group region of DPPC. This study also opens a scope to investigate the dynamics of such bridging H-bonds using the same force field as used in this work. Sharp peaks in the RDF plots of O16 with water H and also P=O with water H, points to the fact that some ordered structure of water might be present in the continuous distribution of water at the interface. Further studies in this direction are required to study the possibility and nature of the ordering of the water molecules present at the interface.

The MSD plots for water molecules present in the different regions near lipid bilayers (Figure 8.11a) clearly shows distinctions in the water dynamics. Similarly, for model atomistic protrusions (chapter 5) different ordering and dynamics of water molecules are observed in the different regions near protrusion-water interface. It proves that the model protrusions depicted in chapter 5 are good representation of lipid bilayer-water syatem discussed in the present chapter. Effect of hydrophobicity/hydrophilicity in biologically inspired systems are further explored in chapter 9 with self-assembly of sophorolipids in water.

[4]The results and figures are adapted from the publication P. R. Pandey and S. Roy, Head group mediated water insertion in DPPC bilayer, The Journal of Physical Chemistry B, 2011, 115, 3155-3163.

Chapter 9

Self-Assembly Simulations of Sophorolipids in Water

9.1 Introduction

Extending the study on model atomistic protrusions (chapter 5 under part A), DPPC bilayer-water interface is studied in chapter 8 which is closer to real system. To further elucidate the effect of hydrophobicity/hydrophilicity in biologically inspired systems, in the present chapter self-assembly of sophorolipid are studied in water. Sophorolipids are structurally different from phospholipids. Phospholipids contain one hydrophilic head group and two hydrophobic tails. Sophorolipids contain two hydrophilic groups at the end of one long hydrophobic tail.

Self-assembly of a chemical moiety in water depends upon the ratio of hydrophobic and hydrophilic groups present in its structure, and also on the amount of water present in the system [4]. Amphiphilic molecules, containing both hydrophobic and hydrophilic groups, can self assemble into variety of structures in water. Block

copolymers self-assemble into different structures depending upon the length of the hydrophobic and hydrophilic blocks, and also upon amount of solvent [176]. Lipids can self-assemble in water as bilayers or micelles depending upon the lipid-water ratio. They can also form reverse micelles in presence of hydrophobic solvent [5]. In organisms, proteins self-assemble into variety of functional structures pointing the hydrophobic groups away from water [6–8]. These structures are important for the protein functioning. Surfactants also self-assemble in water depending upon their concentration in water, and also upon their shape [4]. In all these examples inter- and intramolecular interaction between the self-assembling molecules, and interactions of these molecules with water guide the self assembly process. These interactions can have several components - van der waals, electrostatic, entropic etc. Individual components of interparticle interactions and forces are reviewed by Bishop et al [177].

Modelling and simulations have been proved to be useful tools to elucidate mechanism of self assembly, and understand the structural details of the self-assembled configuration. Wang et al have studied the mechanism and dynamics of self-assembly of dendritic multiarm copolymers using dissipative particle dynamics simulations [178]. They have observed that the dendritic multiarm copolymers first self-assemble into small micelles followed by aggregation of these smaller micelles into large multimolecular micelles. Cai et al have used computer simulations as guide to synthesize supramolecular hierarchical nanostructure of polypeptide based block copolymers and homopolymers [179]. Lee et al have studied the cylindrical nanofibers self assembled from peptide amphiphiles using atomistic MD simulations [180]. Energetic and entropic contributions to the self-assembly process of peptide amphiphiles were further studied using steered molecular dynamics simulations [181]. Shinoda et al have used coarse-grained MD simulations to study the phase behaviour of different self-

assembled structures from Poly(ethylene glycol) attached lipids and zwitterionic lipids [182]. A perspective into the sumulations of self-assembly of different molecules has been provided by Fiorin et al [183].

In the present chapter of the thesis self-assembly of oleic acid sophorolipid (OASL) and linolenic acid sophorolipid (LNSL) are discussed in water using MD simulations. Sophorolipids, due to the presence of two hydrophilic groups at the end of long hydrophobic tail, are also called bolaamphiphiles. These biosurfactants can be obtained by yeast mediated biochemical transformations [184–186]. As the synthesis of sophorolipids involves biochemical steps, these molecules are environmentally less hazardous. As a result sophorolipids have attracted many home care and skin care indistries [187, 188]. They have also been reported to show anti-cancer activities [189]. Self-assembly of OASL in water has been reported by many researchers in the literature. Zhou et al first reported that sophorolipids can form supramolecular self-assembled structure and proved the effect of pH on their self-assembly [190]. Baccile et al have reported the variation of self-assembled structure of OASL depending upon pH [191]. Also, they have correlated the effect of pH on self-assembly to the degree of ionisation ionisation of -COOH group for a range of pH [100]. In addition to the self-assembly OASL (one cis double bond), Dhasaiyan et al have also reported the self assembly of elaidic acid (one trans double bond) and stearic acid (no double bond) [99]. Further, self-assembly of LNSL (3 cis double bond) in water are also reported by Dhasaiyan et al using experimental and simulation studies [192].

Structurally, OASL and LNSL differ with respect to the number of double bonds present in their hydrophobic tail - 1 cis in OASL, and 3 cis in LNSL (Figure 6.3). Both the molecules were considered in their neutral form. That is the -COOH group at the terminal remains as -COOH in the simulations. It corresponds to an acidic pH regime

experimentally. Experimentally, OASL is reported to be self-assembling as ribbons at pH ≈ 2 [99, 190]. Dhasaiyan et al have reported formation of vesicle like structures for LNSL from experiments and MD simulations [192]. In the present chapter we have elucidated structural details of the self assembled structures of LNSL and OASL using MD simulations . Though the self-assembled morphology is known experimentally, structural insight into the self assembled structures is lacking. In the present chapter, using MD simulations, we have elucidated the structural details of the self assembled structure of OASL and LNSL in water. In case of OASL, molecules stack on top of each other. For LNSL, vesicle like structure was observed from simulations with bilayer like arrangement of LNSL molecules. Each leaflet of the vesicle like structure is constructed of bilayer like arrangement of LNSL molecules [192]. Thus, in addition to self-assembly simulations, simulations were performed with pre-assembled bilayers of LNSL to understand the stability of bilayer morphology. DPPC molecules contain hydrophilic choline head group and two hydrophobic tails (chapter 8). Sophorolipid molecules, on the other hand, two hydrophilid head groups (sophorose and -COOH) at the end of hydrophobic tail. In chapter 8, lamellar morphology of DPPC bilayer in water is discussed. In the present chapter, LNSL molecules are observed to self-assemble into vesicle like structure with each leaflet of vesicle formed by LNSL bilayer.

9.2 Comutational Details

9.2.1 Self-assembly simulations

In chapter 2, computational methods is discussed in general. However, the details of simulations specific to the present chapter are as follows. Quantum chemical geome-

try optimization for single molecule of LNSL and OASL to find the stable conformers was performed using Gaussian 09 [193] with B3LYP exchange correlation functional and 6-311G basis set. Using the obtained optimized structure of LNSL and OASL self-assembly simulations were carried out by randomly arranging water solvated sophorolipids (LNSL or OASL) in a simulation box (Figure 9.1). 256 molecules of LNSL or OASL in three times by weight water were used for the simulation studies. This is in relevence to experimental studies on self-assembly of OASL and LNSL in water [99, 192]. Simulations were performed for 700 ns with GROMOS96 53a6 force field and SPC water15c model using GROMACS-4.5.5 package [43]. All the bonded and non-bonded potential parameters for sophorose group were taken from GROMOS force field proposed for hexapyranose based carbohydrates. And parameters for rest of the alkyl chain were taken from GROMOS96-53a6 force field, with dihedrals near the multiple double bonds for LNSL from Bacher et als work. All bonds were constrained and time-step of 2 fs was used. Isothermal isobaric (NPT) ensemble was used to perform the self assembly simulations. Pressure was kept constant at 1 bar using Berendsen barostat [38]. Isotropic pressure coupling and periodic boundary conditions were used. Self-assembly simulations were performed at 350 K to speed up the self assembly process. V-rescale thermostat [35] was used to keep the temperature fixed. Reaction field electrostatics [22] with ϵ_{rf} equal to 80 was used outside the cut off region. For both Coulombic and Lennard-Jones (LJ) interactions cut off distance of 1.2 nm was used.

9.2.2 Simulations of pre-assembled bilayers of LNSL

The simulations of pre-assembled bilayer were performed taking 128 molecules of LNSL (64 in each monolayer), and three times by weight water (Figure 9.6a). Water LNSL interface was created along y-axis. In one case the head group (sophorose part) of the LNSL face the water molecules and in the other the tail (-COOH group) face water (Figure 9.6a). Electrostatic interactions were treated using particle mesh Ewald (PME) method with real space cut off of 1.2 nm. Temperature was kept constant at 300 K using v-rescale thermostat. Semi-isotropic pressure coupling was applied using Berendsen barostat with separate coupling to xy- and z-directions. All the other conditions were same as the self assembly simulations.

9.3 Results and Discussion

Starting from random configuration of sophorolipids (OASL and LNSL) in water self-assembly simulations were performed. The initial random configuration and the self assembled structure are shown in Figure 9.1 for LNSL and OASL. LNSL self-assembles into a vesicle like structure. OASL, on the other hand forms an aggregate. Acidic OASL is known to be self-assembling as twisted or helical ribbons of micrometer length scale [99, 190]. Though such length scale is difficuilt to achieve in MD simulations, studying structural level interactions can be useful. In the present chapter, self-assembly simulation of LNSL reported by Dhasaiyan et al [192] is compared with self-assembly behaviour of OASL in water. Primary emphasis of the present chapter is to understand the arrangement and interactions of the sophorolipids (OASL and LNSL) in the self-assembled structure.

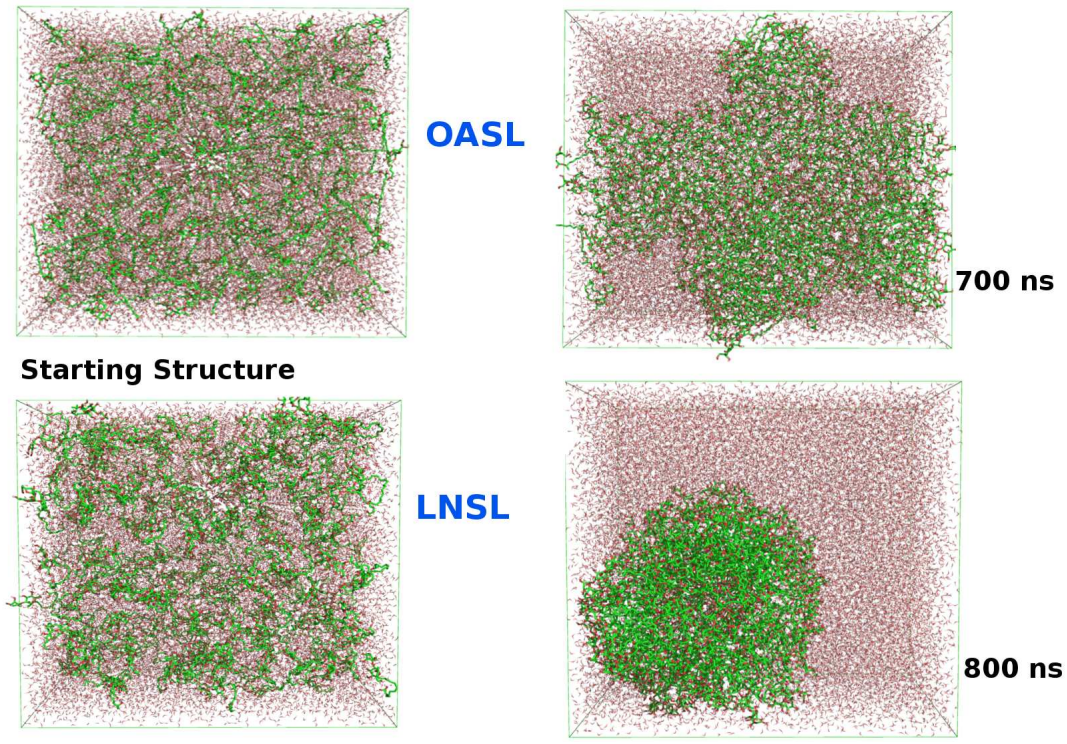

Figure 9.1: Snapshots of starting structure and self-assembled structure of OASL and LNSL. Structures of OASL (1 cis double bond in tail), and LNSL (3 cis double bonds in tail) are provided in Figure 6.3 (Chapter 6). differ in the

9.3.1 Structural arrangement: Hydrogen bonding

Intermolecular radial distribution function (RDF) between oxygens (O) and hydrogens (H) at the head and tail of the sophorolipid molecules are depicted in Figure 9.2 averaged over last 20 ns of the trajectory. The sophorose group is referred to as the *head* and -COOH group as *tail*. All the RDFs between O and H show a sharp first peak at the similar position (minima at $\sim$ 0.25 nm). This is representative of H-bonding among the corresponding groups. Integration of the peak gives number of H-bonds. Thus higher the peak height larger is the H-bond count. Peak height is heighest for tail-tail RDF, followed by tail-head, and finally head-head for both

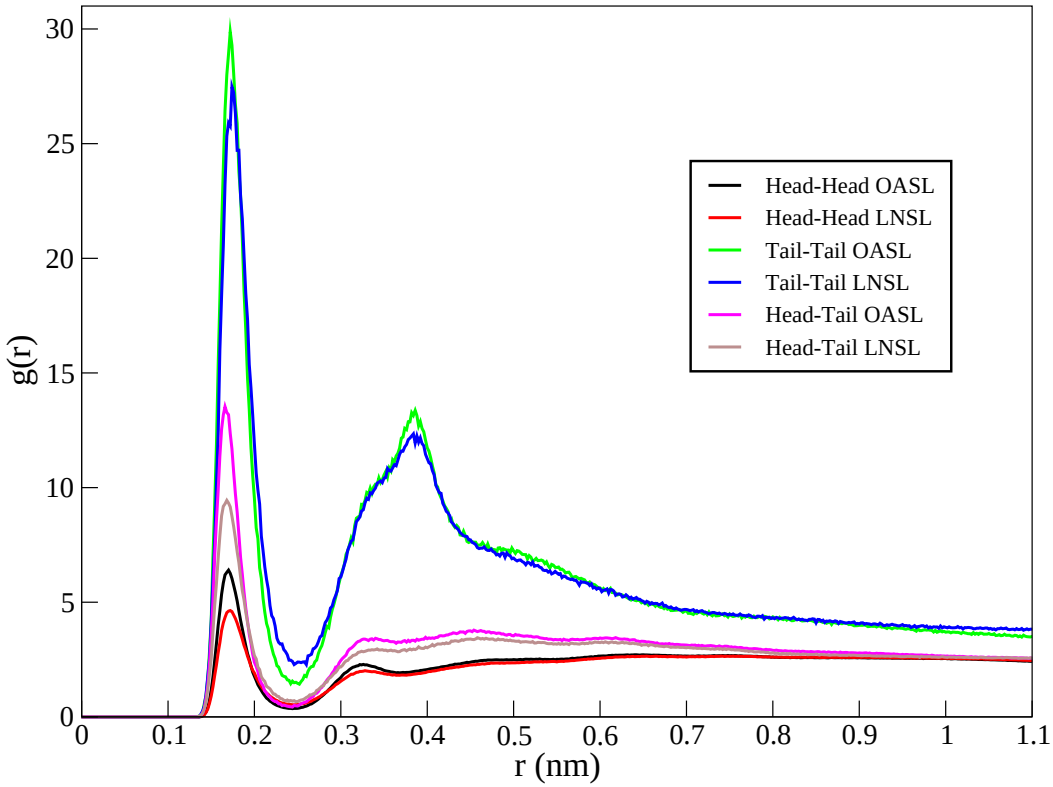

Figure 9.2: RDF between different O and H present in sophorose head group and -COOH tail.

OASL and LNSL. Further, peak heights of OASL RDFs are higher than LNSL in all the cases.

It is evident from the intermolecular RDFs among the different groups that, H-bonding exists between head group and tail group O and H. The number of H-bonds will be useful to understand which H-bond is predominant in the present system. Thus we have plotted count of different intermolecular H-bonds as a function of time in Figure 9.3. To compute different H-bondings we first calculated the distance between O and H present in the head or tail groups. If this distance was below 0.25 nm (corresponding to the first minima of RDFs), donor-hydrogen-acceptor angle was calculated. If this angle was more than 140°, H-bonding was considered. Number of

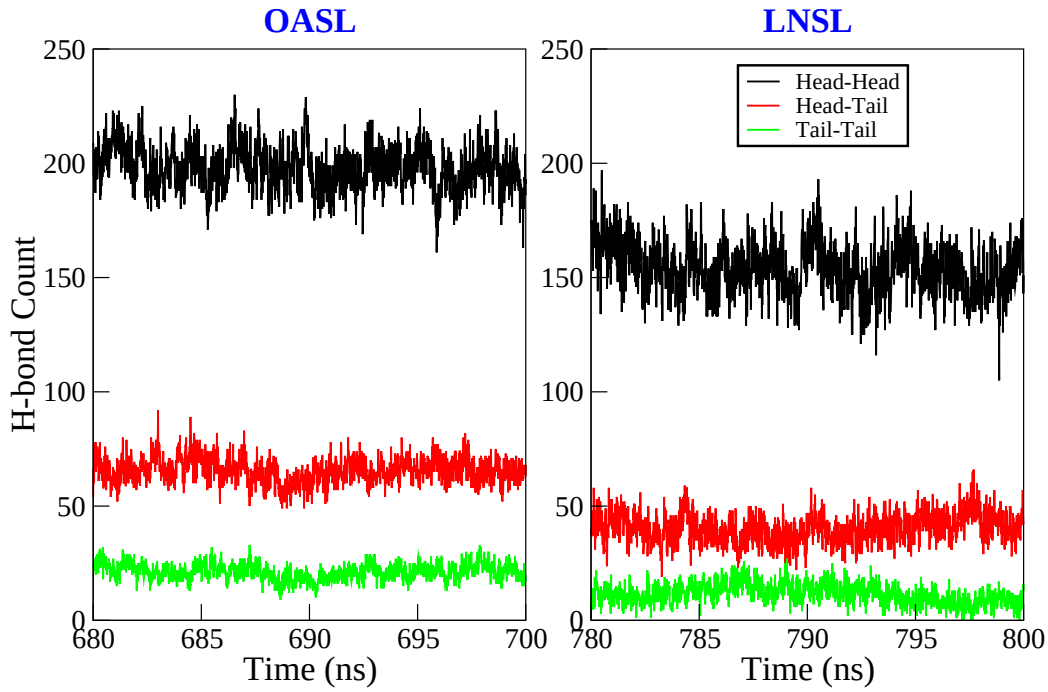

Figure 9.3: Count of head-head, head-tail, and tail-tail H-bonds.

H-bonds were counted in this manner in each frame of the last 20 ns of the trajectories and are plotted as a function of time in Figure 9.3. It is clear from the plot that, H-bond count follows the order head-head >head-tail >tail-tail for both OASL and LNSL. Higher number of O present in the sophorose group accounts for more possible number of sites for H-bonding. It has been reported in the literature that the sophorose head group and -COOH group present in the tail of OASL interact via H-bonding interaction [190].

Further, the -COOH groups present in the tail are capable of forming H-bonded dimer structures. Thus using the above criteria of H-bonding, number of molecules forming H-bonded dimers were counted in each frame of the trajectory and are plotted as a function of time in Figure 9.4. The count is similar for both OASL and LNSL.

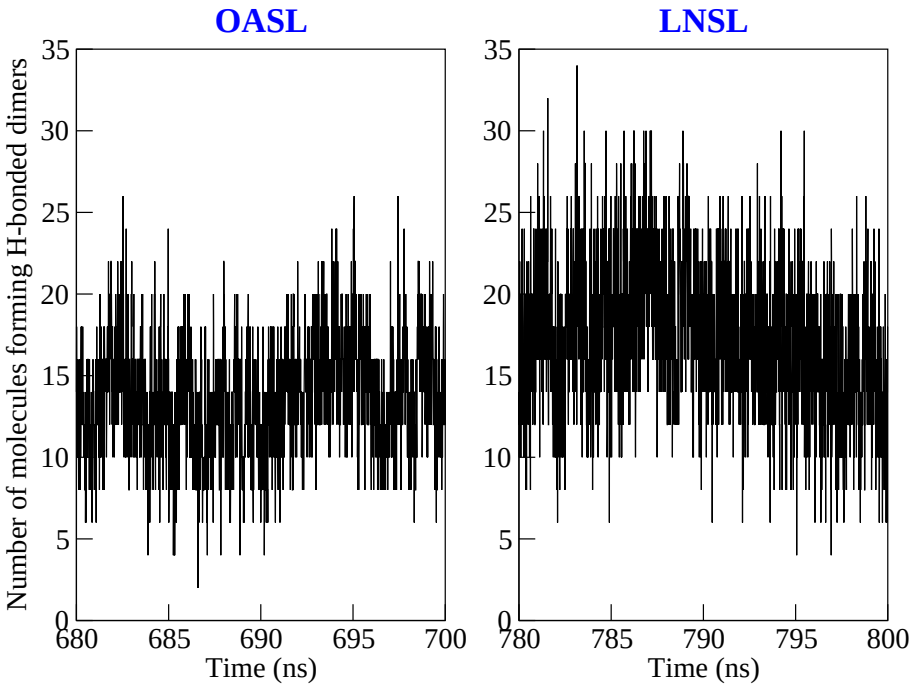

Figure 9.4: Count of H-bonded dimers of tail -COOH group.

This accounts for higher peak height in the RDF plots among tail O and H. Existence of dimeric structures in all the frames increases the probability of finding the tail O and H near each other.

9.3.2 Bilayer-like arrangements of Sophorolipids

Calculation of number of H-bonds suggests that the count of head-head H-bonding is higher than head-tail and tail-tail Figure 9.3. Such head-head H-bonding is possible either in head-on or sideways orientation of the soophorolipid molecules. Head-on approach of sophorolipid molecules will give rise to a bilayer like arrangement with sophorose group pointing towards each other. Such bilayer like arrangement is also possible with head-on approach of head-tail and tail-tail. Thus we have plotted the

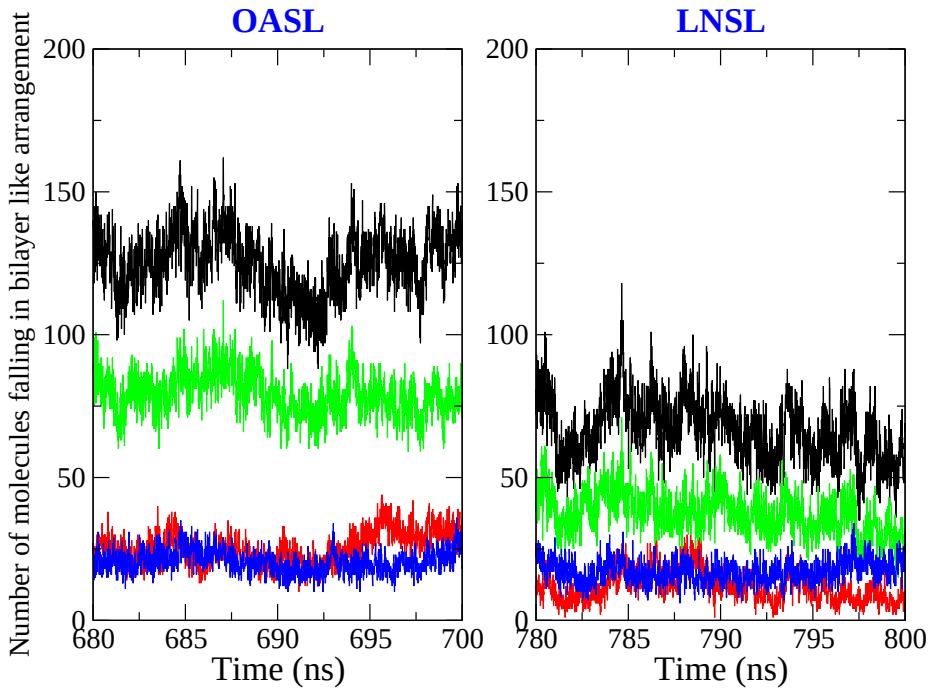

Figure 9.5: Number of molecules forming bilayer like arrangements.

total number of molecules falling into bilayer like arrangements and its individual components, i.e., head-head, head-tail, tail-tail. To calculate this, first the neighbouring LNSL chains were identified from the head-head distance between head O (oxygen between two six membered rings), tail-tail distance between tail C (carbon on COOH group), and head-tail between head O and tail C. Among these neighbouring LNSL chains distance between tail of one molecule and head of the other molecule was computed. Pair for which this distance exceeded 0.3 nm was considered to be in bilayer arrangement. Total number of such molecules and individual contributions were plotted in each frame of last 20 ns of the trajectory in Figure 9.5. Total number of molecules falling in bilayer like arrangement is higher for OASL than LNSL. Further, for both the cases, among the molecules forming bilayer like arranegment the number

of molecules assebled in head-head fashion is higher than any other arrangement. It also indicates head-head arrangements are more favorable than tail-tail arrangement. However, the tail-head and tail-tail arrangements are also probable.

Further, to compare the stability of head-head and tail-tail arrangements and to re-confirm the probability of higher head-head arrangement in bilayer like arrangement, two separate simulations were carried out with 128 LNSL molecules pre-assembled in bilayer like arrangement Figure 9.6a with water on both sides of the bilayer. In one case, the head groups of one monolayer were placed closed to head groups of other monolayer (tail-head-head-tail arrangement), while in the other arrangement tails were near each other (head-tail-tail-head arrangement). After 45 ns of simulation more disruption were observed in the bilayer forced to be in head-tail-tail-head fashion as compared to those observed in tail-head-head-tail arrangement. Also the number of water molecules penetrating the bilayer structure was found to be more for head-tail-tail-head arrangement Figure 9.6b. This further proves the higher stability of tail-head-head-tail alignment.

9.3.3 Conformations of individual molecules in the self-assembled structure

Distribution of intramolecular head - tail distance is plotted in Figure 9.7 to understand the probable conformation of individual molecules in the self-assembled structure for both simulated self-assembled structure Figure 9.1 and the pre-assembled bilayer systems Figure 9.6a. Intramolecular distance for each molecule was calculated in each frame of last 10 ns of the trajectory and converted into histogram. Distributions were plotted from the histogram normalizing over number of frames in

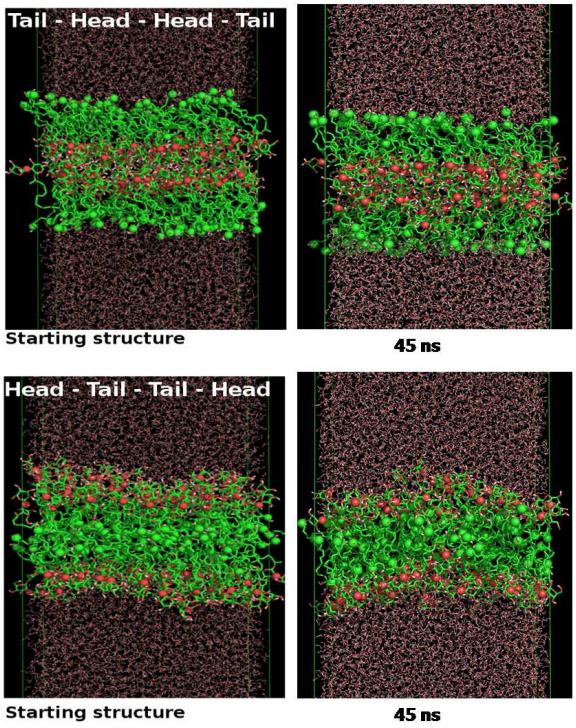

(a)

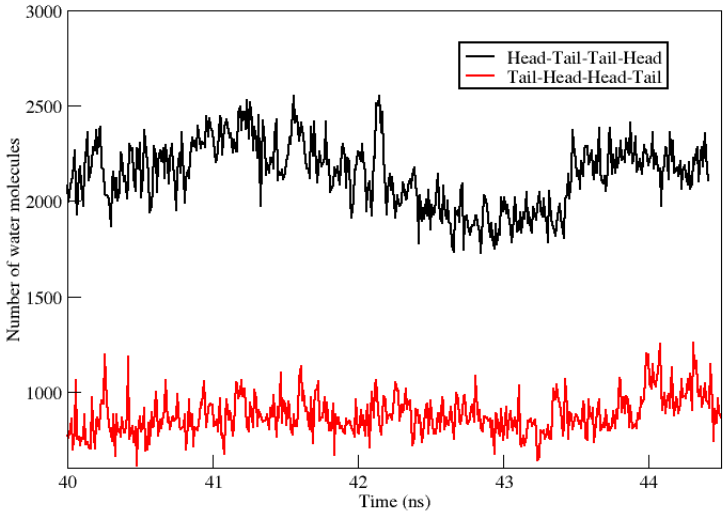

(b)

Figure 9.6: (a) Snapshots for pre-assembled bilayer in tail-head-head-tail, and head-tail-tail-head arrangements (red spheres indicate head group O atom, and green sphere indicates tail C atom), (b) number of water molecules penetrating the bilayer structure as a function of time.

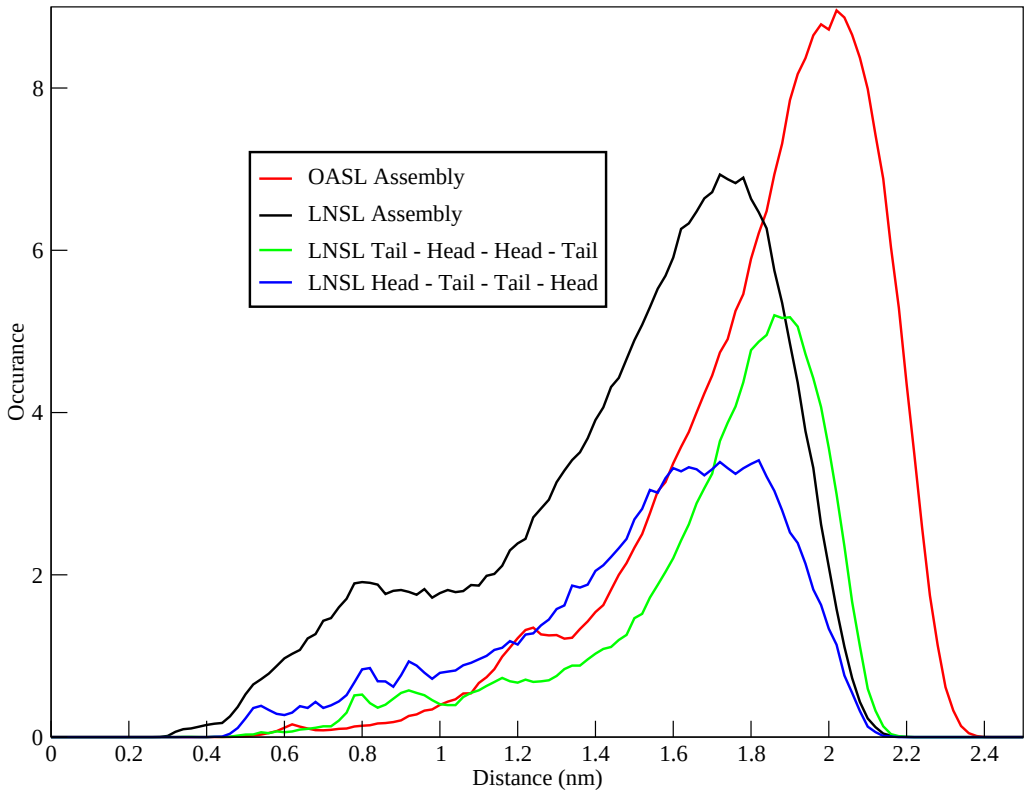

Figure 9.7: Distribution of intramolecular distance between head and tail of sophorolipids.

the last 10 ns of the trajectory. A small hump near 0.9 nm and a broad peak near 1.7 nm can be observed for all the cases of LNSL, whereas these shift to near 1.2 nm and 2 nm respectively for OASL Figure 9.7. This indicates the presence of two conformations of both OASL and LNSL in the self-assembled structures. In the lower distance conformation, the aliphatic chains are bent and the tail COOH group point towards sophorose head group. In contrast, the higher distance conformation the aliphatic chain remains elongated. But the head-tail distance differ on moving from OASL to LNSL. Distances are higher for both lower and higher distance conformations in OASL as compared to LNSL.

9.3.4 Water trapped inside vesicle like structure

Strarting from a random arrangement in water the LNSL molecules self-assemble into vesicle like structure Figure 9.1. During self-assembly water molecules get entrapped inside the vesicle like structure. This is because in the self assembled state, each leaflet of the vesicle like structure consists of bilayer like arrangements (head-head, head-tail, and tail-tail) of the LNSL molecules. As a result, hydrophilic groups point towards the inner core of the vesicle like structure and water molecules get entrapped during self assembly. Count of these entrapped water molecules in each frame of last 10 ns of the trajectory is plotted as a function of time in Figure 9.8a. To calculate this the simulation box was first divided into 20 slabs along z-axis. In each slab, minimum and maximum of x and y components of the carbon atom joining the sophorose head group and hydrophobic tail was calculated. Finally, water molecules falling within the computed range of maximum and minimum of x and y in a slab of z were considered as entrapped within the vesicle like structure. Using these criteria, a snapshot, extracted from real time trajectory, showing the water molecules entrapped inside the vesicle like structure is depicted in Figure 9.8b.

9.4 Conclusion

Long time MD simulations are performed to understand the self-assembly of LNSL and OASL in water. Starting from random arrangement in water OASL self-assembled into aggregate after 700 ns of simulation, and LNSL into vesicle like structure after 800 ns. Head and tail are found to interact via H-bonded interactions for both LNSL and OASL. For both OASL and LNSL, bilayer like arrangement of the sophorolipid molecules are observed. Further, the tail -COOH are found to form H-bonded dimer

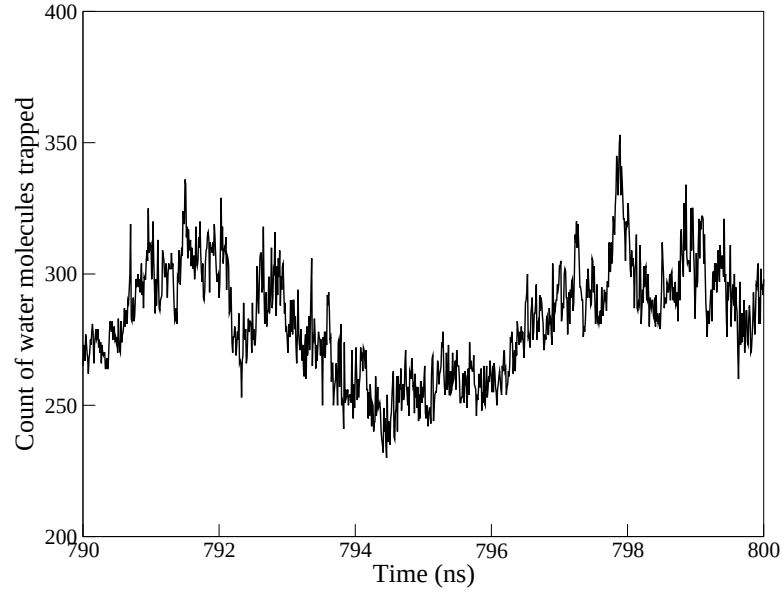

(a)

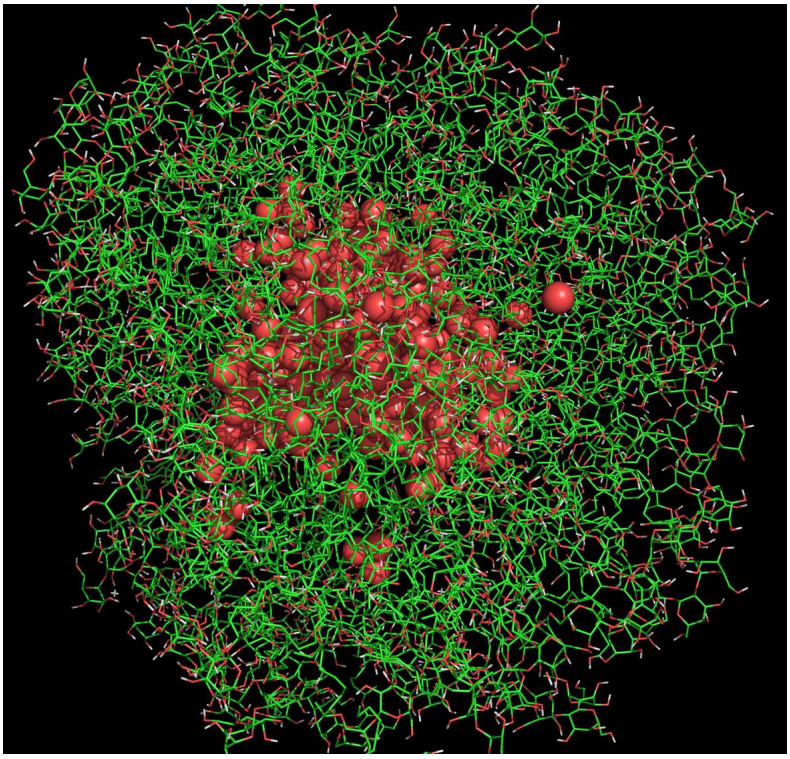

(b)

Figure 9.8: (a) Count of water molecules trapped inside the self-assembled vesicle like structure of LNSL. (b) Snapshot showing trapped water molecules (red spheres). H of water are not shown for clarity.

in both the systems. In the self- assembled structure, two conformations of the individual molecules are detected for both OASL and LNSL. However, the distance between head and tail is higher in OASL as compared to LNSL.

Further, H-bonding lifetime for the different kinds of H-bonds can be computed to understand the structural properties. Also, local arrangements of individual molecules with respect to other molecules can be computed. For LNSL self-assembled structure, we have computed the number of water molecules entrapped inside the vesicle like structure. Structure and dynamics of these trapped water molecules can further be calculated. In the present chapter we have presented simulations of 1:3 weight ratio of sophorolipid to water. Further 1:1, and 1:2 weight ratios can also be studied.

Sophorolipids differ structurally from phospholipids (DPPC, discussed in chapter 8) in number of hydrophilic head groups and construction of hydrophobic tail. However, sophorolipids satisfies the focuss of part B of the present thesis, that is, to envisage biologically inspired systems varying in degree of hydrophilic/hydrophobic groups present (see chapter 6). On moving from DPPC to sophorolipids degree of both hydrophilicity (one hydrophilic head group in DPPC to two in sophorolipids), and hydrophobicity (two hydrophobic tails in DPPC to one in sphorolipids) vary. Hence, the distinctions in structural arrangements observed.

[5]The results and figures for LNSL are adapted from the publication P. Dhasaiyan, P. R. Pandey, N. Visaveliya, S. Roy, and B. L. V. Prasad, Vesicle structures from bola-amphiphilic bio-surfactants: Experimental and MD simulation studies on the effect of unsaturation on the sophorolipid self-assemblies, Chemistry - A European Journal, 2014, 20, 6246-6250.

Chapter 10

Conclusion

In this thesis we have presented the mechanism and energetics of wetting and dewetting of model surfaces, and structure and dynamics of biologically inspired systems using molecular dynamics simulations. The chapters in the present thesis are organised such that starting from model systems, we move closer to real systems. However, in all the systems under consideration, interface with water is common. Acoordingly, the thesis is divided into two parts - model surfaces and interfaces, and biologically inspired systems.

In part A, resesearch is carried out on wetting and dewetting of model hydrophilic surfaces, and structure and dynamics of water near model atomistic protrusions. Starting with an introduction to wettability of surfaces and structuring of water in confinements (chapter 3), model hydrophilic surfaces and atomistic protrusions are discussed in chapters 4 and 5 respectively.

Mechanism and energetics of wetting and dewetting of model rough hydrophilic surface are elucidated in chapter 4. The model surfaces are designed such that hydrophilic square pillar arrays are mounted on top of flat hydrophilic surface. Series

of surfaces are studied by varying the surface roughness. Hydrophilicity of the surfaces are defined and varied depending upon Lennard-Jones interaction parameter between water and surface. A correlation between roughness and energetics of wetting/dewetting has been established. In the present thesis (chapter 4), only the energetic contribution to the wetting behaviour has been elucidated. The entropic contribution to the wetting and dewetting behaviour can further be envisaged. Also, topology of the surface can further be varied by changing the square morphology to other structures keeping the roughness constant. This will enable us to understand and compare the enegetic and entropic contribution to the wetting behaviour.

In chapter 5 under part A, research is focussed on structure and dynamics of water molecules near model atomistic protrusions at a range of temperatures and pressures. The atomistic protrusions are modelled such that they consist of hydrophobic and hydrophilic blocks, and interface with water is created with the hydrophilic region. This model is structurally motivated from lipid bilayer-water system. Hydrophilicity/hydrophobicity of the particles constituting the protrusions are defined with respect to their Lennard-Jones interaction with water. Temperature is varied from 290 K to 200 K, and at each temperature pressure is varied from 1 bar to 200 bar to understand their effect on the structure and dynamics of water molecules near the protrusions. Defining distinct regions at the protrusions-water interface shows differences in the ordering and retension properties of water molecules. The hydrophobicity and hydrophilicity of the particles constituting the protrusions can further be varied to achieve desirable ordering and retension properties of water. Also studying mixtures of fluids near the protrusions can help in designing molecular sieves. Althogh, we have moved upto 200 K, no ice formation is observed in the system. Thus, ice nucleation and growth can further be studied near these atomistic protrusions. How-

ever, nucleation and growth of ice involves an energy barrier to be crossed. Also, in the present model system the different Lennard-Jones particles may favour or hinder the ice nucleation.

In part B, we have moved closer to real systems keeping the interface with water, and research is focussed on biologically inspired systems. Starting with a short introduction to the importance of hydrophobicity and hydrophilicity in biological systems (chapter 6), unwinding mechanism of model α-helical homopolymeric peptides in water, mechanism of water insertion into DPPC bilayer, and self-assembly of sophorolipids in water are explored in chapters 7, 8, and 9 respectively.

Mechanism of unwinding of α-helical homopolymeric peptides differing in their side-chain hydrophobicity and terminal groups are investigated in water in chapter 7. Role of water in the unwinding mechanism and energetics of unwinding are elucidated. Such study on model peptides can help developing predictive models to understand secondary structures of proteins. Although in the present thesis, research is carried out on homopolymeric peptides, the study can further be extended to block copolymeric peptides. This will help to understand whether the insights gained from the homopolymeric peptides are translated to block copolymeric peptides or not.

Extending the study on model atomistic protrusions (chapter 5) close to real systems, mechanism of water insertion into the phospholipid bilayer-water interface is studied in chapter 8. Interplay of two dihedrals at the choline head group of DPPC mediated the insertion of water upto the starting point of the hydrophobic region region at DPPC bilayer-water interface. Dynamics of water at different regions near the interface are also explored. In connection with the atomistic protrusions, distinction in water dynamics is observed at the DPPC bilayer-water interface.

Importance of hydrophobicity and hydrophilicity in biological systems are further

explored by studying self-assembly of oleic acid and linolenic acid sophorolipids in water in chapter 9. On moving from DPPC to sophorolipids degree of both hydrophilicity (one hydrophilic head group in DPPC to two in sophorolipids), and hydrophobicity (two hydrophobic tails in DPPC to one in sphorolipids) vary. Oleic acid and linolenic acid sophorolipids differ in the number of double bonds present in the hydrophobic tail. In this thesis, self-assebly of oleic acid and linolenic acid sophorolipids are studied with 1:3 weight ratio in water. This is in relevence to the experimental reports [99, 192]. There remains further scope to investigate the self-assembly behaviour at other weight ratios.

Bibliography

[1] M. Praprotnik, L. D. Site, and K. Kremer, "Multiscale simulation of soft matter: From scale bridging to adaptive resolution," *Annual Review of Physical Chemistry*, vol. 59, no. 1, pp. 545–571, 2008. PMID: 18062769.

[2] `http://www1.lsbu.ac.uk/water`.

[3] D. Bonn, J. Eggers, J. Indekeu, J. Meunier, and E. Rolley, "Wetting and spreading," *Rev. Mod. Phys.*, vol. 81, pp. 739–805, May 2009.

[4] J. N. Israelachvili, *Intermolecular and Surface Forces*. Academic Press, London, 1985.

[5] C. M. Carvalho and J. M. Cabral, "Reverse micelles as reaction media for lipases," *Biochimie*, vol. 82, no. 11, pp. 1063 – 1085, 2000. Lipase 2000.

[6] F. Chiti and C. M. Dobson, "Protein misfolding, functional amyloid, and human disease," *Annual Review of Biochemistry*, vol. 75, no. 1, pp. 333–366, 2006. PMID: 16756495.

[7] D. M. Fowler, A. V. Koulov, C. Alory-Jost, M. S. Marks, W. E. Balch, and J. W. Kelly, "Functional amyloid formation within mammalian tissue," *PLoS Biol*, vol. 4, p. e6, 11 2005.

[8] N. D. Hammer, X. Wang, B. A. McGuffie, and M. R. Chapman, "Amyloids: Friend or foe?," *J. Alzheimer's Dis*, vol. 13, 2008.

[9] M. D. Collins, G. Hummer, M. L. Quillin, B. W. Matthews, and S. M. Gruner, "Cooperative water filling of a nonpolar protein cavity observed by high-pressure crystallography and simulation," *PNAS*, vol. 102, no. 46, pp. 16668–16671, 2005.

[10] M. D. Collins, M. L. Quillin, G. Hummer, B. W. Matthews, and S. M. Gruner, "Structural rigidity of a large cavity-containing protein revealed by high-pressure crystallography," *J. Mol. Biol.*, vol. 367, no. 3, pp. 752 – 763, 2007.

[11] C. K. Choudhury and S. Roy, "Structural and dynamical properties of polyethylenimine in explicit water at different protonation states: a molecular dynamics study," *Soft Matter*, vol. 9, pp. 2269–2281, 2013.

[12] C. K. Choudhury, A. Kumar, and S. Roy, "Characterization of conformation and interaction of gene delivery vector polyethylenimine with phospholipid bilayer at different protonation state," *Biomacromolecules*, vol. 14, no. 10, pp. 3759–3768, 2013.

[13] S. Pahari, C. K. Choudhury, P. R. Pandey, M. More, A. Venkatnathan, and S. Roy, "Molecular dynamics simulation of phosphoric acid doped monomer of polybenzimidazole: A potential component polymer electrolyte membrane of fuel cell," *The Journal of Physical Chemistry B*, vol. 116, no. 24, pp. 7357–7366, 2012.

[14] S. Pahari and S. Roy, "Evidence and characterization of dynamic heterogeneity in binary mixtures of phosphoric acid and benzimidazole," *The Journal of Chemical Physics*, vol. 139, no. 15, pp. –, 2013.

[15] S. Chakraborty and S. Roy, "Structural, dynamical, and thermodynamical properties of carbon nanotube polycarbonate composites: A molecular dynamics study," *The Journal of Physical Chemistry B*, vol. 116, no. 10, pp. 3083–3091, 2012.

[16] S. Chakraborty, C. K. Choudhury, and S. Roy, "Morphology and dynamics of carbon nanotube in polycarbonate carbon nanotube composite from dissipative particle dynamics simulation," *Macromolecules*, vol. 46, no. 9, pp. 3631–3638, 2013.

[17] V. S. Baghel, R. Kumar, and S. Roy, "Heat transfer calculations for decomposition of structure i methane hydrates by molecular dynamics simulation," *The Journal of Physical Chemistry C*, vol. 117, no. 23, pp. 12172–12182, 2013.

[18] W. Barthlott and C. Neinhuis, "Purity of the sacred lotus, or escape from contamination in biological surfaces," *Planta*, vol. 202, no. 1, pp. 1–8, 1997.

[19] A. W. Gtz, M. J. Williamson, D. Xu, D. Poole, S. Le Grand, and R. C. Walker, "Routine microsecond molecular dynamics simulations with amber on gpus. 1. generalized born," *Journal of Chemical Theory and Computation*, vol. 8, no. 5, pp. 1542–1555, 2012.

[20] R. Salomon-Ferrer, A. W. Gtz, D. Poole, S. Le Grand, and R. C. Walker, "Routine microsecond molecular dynamics simulations with amber on gpus. 2.

explicit solvent particle mesh ewald," *Journal of Chemical Theory and Computation*, vol. 9, no. 9, pp. 3878–3888, 2013.

[21] M. G. Saunders and G. A. Voth, "Coarse-graining methods for computational biology," *Annual Review of Biophysics*, vol. 42, no. 1, pp. 73–93, 2013. PMID: 23451897.

[22] M. P. Allen and D. J. Tildesley, *Computer Simulation of Liquids*. Clarendon Press, Oxford, 1987.

[23] W. L. Jorgensen, D. S. Maxwell, and J. Tirado-Rives, "Development and testing of the opls all-atom force field on conformational energetics and properties of organic liquids," *Journal of the American Chemical Society*, vol. 118, no. 45, pp. 11225–11236, 1996.

[24] G. A. Kaminski, R. A. Friesner, J. Tirado-Rives, and W. L. Jorgensen, "Evaluation and reparametrization of the opls-aa force field for proteins via comparison with accurate quantum chemical calculations on peptides," *The Journal of Physical Chemistry B*, vol. 105, no. 28, pp. 6474–6487, 2001.

[25] Y. Duan, C. Wu, S. Chowdhury, M. C. Lee, G. Xiong, W. Zhang, R. Yang, P. Cieplak, R. Luo, T. Lee, J. Caldwell, J. Wang, and P. Kollman *J. Comput. Chem.*, vol. 24, pp. 1999 – 2012, 2003.

[26] B. R. Brooks, C. L. Brooks, III, A. D. Mackerell, Jr., L. Nilsson, R. J. Petrella, B. Roux, Y. Won, G. Archontis, C. Bartels, S. Boresch, A. Caflisch, L. Caves, Q. Cui, A. R. Dinner, M. Feig, S. Fischer, J. Gao, M. Hodoscek, W. Im, K. Kuczera, T. Lazaridis, J. Ma, V. Ovchinnikov, E. Paci, R. W. Pastor, C. B. Post,

J. Z. Pu, M. Schaefer, B. Tidor, R. M. Venable, H. L. Woodcock, X. Wu, W. Yang, D. M. York, and M. Karplus, "CHARMM: The Biomolecular Simulation Program," *Journal of Computational Chemistry*, vol. 30, pp. 1545–1614, JUL 30 2009.

[27] B. Brooks, R. Bruccoleri, D. Olafson, D. States, S. Swaminathan, and M. Karplus, "Charmm: A program for macromolecular energy, minimization, and dynamics calculations," *Journal of Computational Chemistry*, vol. 4, pp. 187–217, 1983.

[28] A. MacKerel Jr., C. Brooks III, L. Nilsson, B. Roux, Y. Won, and M. Karplus, *CHARMM: The Energy Function and Its Parameterization with an Overview of the Program*, vol. 1 of *The Encyclopedia of Computational Chemistry*, pp. 271–277. John Wiley & Sons: Chichester, 1998.

[29] C. Oostenbrink, A. Villa, A. E. Mark, and W. F. Van Gunsteren, "A biomolecular force field based on the free enthalpy of hydration and solvation: The gromos force-field parameter sets 53a5 and 53a6," *Journal of Computational Chemistry*, vol. 25, no. 13, pp. 1656–1676, 2004.

[30] R. Hockney, S. Goel, and J. Eastwood, "Quiet high-resolution computer models of a plasma," *Journal of Computational Physics*, vol. 14, no. 2, pp. 148 – 158, 1974.

[31] B. Hess, H. Bekker, H. J. C. Berendsen, and J. G. E. M. Fraaije, "Lincs: A linear constraint solver for molecular simulations," *Journal of Computational Chemistry*, vol. 18, no. 12, pp. 1463–1472, 1997.

[32] J.-P. Ryckaert, G. Ciccotti, and H. J. Berendsen, "Numerical integration of the cartesian equations of motion of a system with constraints: molecular dynamics of n-alkanes," *Journal of Computational Physics*, vol. 23, no. 3, pp. 327 – 341, 1977.

[33] D. van der Spoel and P. J. van Maaren, "The origin of layer structure artifacts in simulations of liquid water," *Journal of Chemical Theory and Computation*, vol. 2, no. 1, pp. 1–11, 2006.

[34] D. Frenkel and B. Smit, *Understanding Molecular Simulation, Second Edition: From Algorithms to Applications (Computational Science).* Academic Press, 2 ed., Nov. 2001.

[35] G. Bussi, D. Donadio, and M. Parrinello, "Canonical sampling through velocity rescaling," *The Journal of Chemical Physics.*, vol. 126, no. 1, p. 014101, 2007.

[36] S. Nos, "A unified formulation of the constant temperature molecular dynamics methods," *The Journal of Chemical Physics*, vol. 81, no. 1, 1984.

[37] W. G. Hoover, "Canonical dynamics: Equilibrium phase-space distributions," *Phys. Rev. A*, vol. 31, pp. 1695–1697, Mar 1985.

[38] H. J. C. Berendsen, J. P. M. Postma, W. F. van Gunsteren, A. Dinola, and J. R. Haak *The Journal of Chemical Physics.*, vol. 81(8), pp. 3684 – 3690, 1984.

[39] M. Parrinello and A. Rahman, "Polymorphic transitions in single crystals: A new molecular dynamics method," *Journal of Applied Physics*, vol. 52, no. 12, pp. 7182–7190, 1981.

[40] S. Nos and M. Klein, "Constant pressure molecular dynamics for molecular systems," *Molecular Physics*, vol. 50, no. 5, pp. 1055–1076, 1983.

[41] D. Van Der Spoel, E. Lindahl, B. Hess, G. Groenhof, A. E. Mark, and H. J. C. Berendsen, "Gromacs: Fast, flexible, and free," *Journal of Computational Chemistry*, vol. 26, no. 16, pp. 1701–1718, 2005.

[42] D. Van Der Spoel, E. Lindahl, B. Hess, G. Groenhof, A. E. Mark, and H. J. C. Berendsen *J. Comput. Chem.*, vol. 26, pp. 1701 – 1718, 2005.

[43] S. Pronk, S. Pll, R. Schulz, P. Larsson, P. Bjelkmar, R. Apostolov, M. R. Shirts, J. C. Smith, P. M. Kasson, D. van der Spoel, B. Hess, and E. Lindahl, "Gromacs 4.5: a high-throughput and highly parallel open source molecular simulation toolkit," *Bioinformatics*, vol. 29, no. 7, pp. 845–854, 2013.

[44] A. Shahraz, A. Borhan, and K. A. Fichthorn, "Wetting on physically patterned solid surfaces: The relevance of molecular dynamics simulations to macroscopic systems," *Langmuir*, vol. 29, no. 37, pp. 11632–11639, 2013.

[45] G. McHale, N. J. Shirtcliffe, S. Aqil, C. C. Perry, and M. I. Newton, "Topography driven spreading," *Phys. Rev. Lett.*, vol. 93, p. 036102, Jul 2004.

[46] A. Marmur, "The lotus effect: superhydrophobicity and metastability," *Langmuir*, vol. 20, no. 9, pp. 3517–3519, 2004. PMID: 15875376.

[47] M. E. Abdelsalam, P. N. Bartlett, T. Kelf, and J. Baumberg, "Wetting of regularly structured gold surfaces," *Langmuir*, vol. 21, no. 5, pp. 1753–1757, 2005.

[48] Q. Yuan and Y.-P. Zhao, "Multiscale dynamic wetting of a droplet on a lyophilic pillar-arrayed surface," *J. Fluid. Mech.*, vol. 716, pp. 171–188, 2 2013.

[49] Q. Yuan and Y.-P. Zhao, "Wetting on flexible hydrophilic pillar-arrays," *Sci. Rep.*, vol. 3, p. 1944.

[50] W. Wang, "Lyophilization and development of solid protein pharmaceuticals," *Int. J. Pharm.*, vol. 203, no. 12, pp. 1 – 60, 2000.

[51] A. L. DeVries, "Antifreeze peptides and glycopeptides in cold-water fishes," *Annu. Rev. Physiol.*, vol. 45, no. 1, pp. 245–260, 1983.

[52] A. R. Parker and C. R. Lawrence, "Water capture by a desert beetle," *Nature*, vol. 414, pp. 33–34, 2001.

[53] C. Neinhuis and W. Barthlott, "Characterization and distribution of water-repellent, self-cleaning plant surfaces," *Annals of Botany*, vol. 79, no. 6, pp. 667–677, 1997.

[54] C. Yang, U. Tartaglino, and B. N. J. Persson, "Influence of surface roughness on superhydrophobicity," *Phys. Rev. Lett.*, vol. 97, p. 116103, Sep 2006.

[55] H. Kim, J. K. Saha, and J. Jang, "Drying transition of water confined between hydrophobic pillars," *J. Phys. Chem. C*, vol. 116, no. 36, pp. 19233–19239, 2012.

[56] K. Koch and W. Barthlott, "Superhydrophobic and superhydrophilic plant surfaces: an inspiration for biomimetic materials," *Philosophical Transactions of the Royal Society A: Mathematical, Physical and Engineering Sciences*, vol. 367, no. 1893, pp. 1487–1509, 2009.

[57] J. Drelich, E. Chibowski, D. D. Meng, and K. Terpilowski, "Hydrophilic and superhydrophilic surfaces and materials," *Soft Matter*, vol. 7, pp. 9804–9828, 2011.

[58] X. Feng and L. Jiang, "Design and creation of superwetting/antiwetting surfaces," *Advanced Materials*, vol. 18, no. 23, pp. 3063–3078, 2006.

[59] W. L. Jorgensen, J. Chandrasekhar, J. D. Madura, R. W. Impey, and M. L. Klein, "Comparison of simple potential functions for simulating liquid water," *The Journal of Chemical Physics.*, vol. 79, no. 2, pp. 926–935, 1983.

[60] J. C. Rasaiah, S. Garde, and G. Hummer, "Water in nonpolar confinement: From nanotubes to proteins and beyond," *Annu. Rev. Phys. Chem.*, vol. 59, no. 1, pp. 713–740, 2008.

[61] R. Mancinelli, "The effect of confinement on water structure," *J. Phys.: Condens. Matter*, vol. 22, no. 40, p. 404213, 2010.

[62] D. Takaiwa, I. Hatano, K. Koga, and H. Tanaka, "Phase diagram of water in carbon nanotubes," *PNAS*, vol. 105, no. 1, pp. 39–43, 2008.

[63] S. Vaitheeswaran, H. Yin, J. C. Rasaiah, and G. Hummer, "Water clusters in nonpolar cavities," *PNAS*, vol. 101, no. 49, pp. 17002–17005, 2004.

[64] S. Vaitheeswaran, J. C. Rasaiah, and G. Hummer, "Electric field and temperature effects on water in the narrow nonpolar pores of carbon nanotubes," *The Journal of Chemical Physics.*, vol. 121, no. 16, pp. 7955–7965, 2004.

[65] Y. Leng and P. T. Cummings, "Fluidity of hydration layers nanoconfined between mica surfaces," *Phys. Rev. Lett.*, vol. 94, p. 026101, Jan 2005.

[66] K. Koga and H. Tanaka, "Phase diagram of water between hydrophobic surfaces," *The Journal of Chemical Physics.*, vol. 122, no. 10, p. 104711, 2005.

[67] J. C. Johnston, N. Kastelowitz, and V. Molinero, "Liquid to quasicrystal transition in bilayer water," *The Journal of Chemical Physics.*, vol. 133, no. 15, p. 154516, 2010.

[68] S. Khan and J. K. Singh, "Wetting transition of nanodroplets of water on textured surfaces: a molecular dynamics study," *Molecular Simulation*, vol. 0, no. 0, pp. 1–11, 2013.

[69] H. Kumar, B. Mukherjee, S.-T. Lin, C. Dasgupta, A. K. Sood, and P. K. Maiti, "Thermodynamics of water entry in hydrophobic channels of carbon nanotubes," *The Journal of Chemical Physics.*, vol. 134, no. 12, p. 124105, 2011.

[70] T. G. Lombardo, N. Giovambattista, and P. G. Debenedetti, "Structural and mechanical properties of glassy water in nanoscale confinement," *Faraday Discuss.*, vol. 141, pp. 359–376, 2009.

[71] B. A. Bauer, S. Ou, S. Patel, and K. Siva, "Dynamics and energetics of hydrophobically confined water," *Phys. Rev. E*, vol. 85, p. 051506, May 2012.

[72] P. R. Pandey and S. Roy, "Is it possible to change wettability of hydrophilic surface by changing its roughness?," *J. Phys. Chem. Lett.*, vol. 4, no. 21, pp. 3692–3697, 2013.

[73] H. J. C. Berendsen, J. R. Grigera, and T. P. Straatsma, "The missing term in effective pair potentials," *J. Phys. Chem.*, vol. 91, no. 24, pp. 6269–6271, 1987.

[74] D. Frenkel and B. Smit, *Understanding Molecular Simulation: From Algorithms to Applications*. Orlando, FL, USA: Academic Press, Inc., 2nd ed., 2002.

[75] F. MullerPlathe, S. Pal, H. Weiss, and H. Keller, "Tutorial: Can nanostructuring improve the properties of hydrophobic surfaces?," *Soft Materials*, vol. 3, no. 1, pp. 21–43, 2005.

[76] S. Pal, H. Weiss, H. Keller, and F. Muller-Plathe, "The hydrophobicity of nanostructured alkane and perfluoro alkane surfaces: A comparison by molecular dynamics simulation," *Phys. Chem. Chem. Phys.*, vol. 7, pp. 3191–3196, 2005.

[77] F. Leroy and F. Mller-Plathe, "Can continuum thermodynamics characterize wenzel wetting states of water at the nanometer scale?," *Journal of Chemical Theory and Computation*, vol. 8, no. 10, pp. 3724–3732, 2012.

[78] J. R. Errington and P. G. Debenedetti, "Relationship between structural order and the anomalies of liquid water," *Nature*, vol. 409, pp. 318–321, 2001.

[79] N. Giovambattista, P. J. Rossky, and P. G. Debenedetti, "Effect of temperature on the structure and phase behavior of water confined by hydrophobic, hydrophilic, and heterogeneous surfaces," *The Journal of Physical Chemistry B*, vol. 113, no. 42, pp. 13723–13734, 2009.

[80] A. Debnath, B. Mukherjee, K. G. Ayappa, P. K. Maiti, and S.-T. Lin, "Entropy and dynamics of water in hydration layers of a bilayer," *The Journal of Chemical Physics.*, vol. 133, no. 17, p. 174704, 2010.

[81] R. W. Impey, P. A. Madden, and I. R. McDonald, "Hydration and mobility of ions in solution," *J. Phys. Chem.*, vol. 87, no. 25, pp. 5071–5083, 1983.

[82] R. G. Fernandez, J. L. F. Abascal, and C. Vega, "The melting point of ice i[sub h] for common water models calculated from direct coexistence of the solid-liquid interface," *The Journal of Chemical Physics.*, vol. 124, no. 14, p. 144506, 2006.

[83] E. B. Moore, E. de la Llave, K. Welke, D. A. Scherlis, and V. Molinero, "Freezing, melting and structure of ice in a hydrophilic nanopore," *Phys. Chem. Chem. Phys.*, vol. 12, pp. 4124–4134, 2010.

[84] E. B. Moore and V. Molinero, "Structural transformation in supercooled water controls the crystallization rate of ice," *Nature*, vol. 479, pp. 506–508, 2011.

[85] S. J. Singer and G. L. Nicolson, "The fluid mosaic model of the structure of cell membranes," *Science*, vol. 175, no. 4023, pp. 720–731, 1972.

[86] L. G. Presta and G. D. Rose *Science*, vol. 240, p. 1632, 1988.

[87] S. Padmanabhan, S. Marqusee, T. Ridgeway, T. M. Laue, and R. L. Baldwin *Nature*, vol. 344, p. 268, 1990.

[88] A. Chakrabartty, T. Kortemme, and R. L. Baldwin *Protein Science*, vol. 3, p. 843, 1994.

[89] A. Chakrabartty and R. L. Baldwin *Adv. Protein. Chem.*, vol. 46, pp. 141 – 176, 1995.

[90] X. Daura, K. Gademann, B. Jaun, D. Seebach, W. F. van Gunsteren, and A. E. Mark *Angew. Chem. Int. Ed.*, vol. 38, p. 236, 1999.

[91] F. M. DiCapua, S. Swaminathan, and D. L. Beveridge *Journal of the American Chemical Society*, vol. 112, p. 6768, 1990.

[92] F. M. DiCapua, S. Swaminathan, and D. L. Beveridge *Journal of the American Chemical Society*, vol. 113, p. 6145, 1991.

[93] H. Hauser, I. Pascher, R. Pearson, and S. Sundell, "Preferred conformation and molecular packing of phosphatidylethanolamine and phosphatidylcholine," *Biochimica et Biophysica Acta (BBA) - Reviews on Biomembranes*, vol. 650, no. 1, pp. 21 – 51, 1981.

[94] H. Hauser, W. Guyer, I. Pascher, P. Skrabal, and S. Sundell, "Polar group conformation of phosphatidylcholine. effect of solvent and aggregation," *Biochemistry*, vol. 19, no. 2, pp. 366–373, 1980.

[95] H. Hauser, W. Guyer, I. Pascher, P. Skrabal, and S. Sundell, "Polar group conformation of phosphatidylcholine. effect of solvent and aggregation," *Biochemistry*, vol. 19, no. 2, pp. 366–373, 1980.

[96] M. Hong, K. Schmidt-Rohr, and H. Zimmermann, "Conformational constraints on the headgroup and sn-2 chain of bilayer dmpc from nmr dipolar couplings," *Biochemistry*, vol. 35, no. 25, pp. 8335–8341, 1996.

[97] K. S. Bruzik and J. S. Harwood, "Conformational study of phospholipids in crystalline state and hydrated bilayers by 13c and 31p cp-mas nmr," *Journal of the American Chemical Society*, vol. 119, no. 28, pp. 6629–6637, 1997.

[98] F. Aussenac, M. Laguerre, J.-M. Schmitter, and E. J. Dufourc, "Detailed structure and dynamics of bicelle phospholipids using selectively deuterated and perdeuterated labels. 2h nmr and molecular mechanics study," *Langmuir*, vol. 19, no. 25, pp. 10468–10479, 2003.

[99] P. Dhasaiyan, A. Banerjee, N. Visaveliya, and B. L. V. Prasad, "Influence of the sophorolipid molecular geometry on their self-assembled structures," *Chemistry An Asian Journal*, vol. 8, no. 2, pp. 369–372, 2013.

[100] N. Baccile, F. Babonneau, J. Jestin, G. Pehau-Arnaudet, and I. Van Bogaert, "Unusual, ph-induced, self-assembly of sophorolipid biosurfactants," *ACS Nano*, vol. 6, no. 6, pp. 4763–4776, 2012.

[101] L. Pauling, R. B. Corey, and H. R. Branson *Proc. Natl. Acad. Sci. U.S.A*, vol. 37, pp. 205 – 211, 1951.

[102] W. Maison, E. Arce, P. Renold, R. J. Kennedy, and D. S. Kemp, "Optimal n-caps for n-terminal helical templates: effects of changes in h-bonding efficiency and charge," *Journal of the American Chemical Society*, vol. 123, no. 42, pp. 10245–10254, 2001.

[103] R. J. Kennedy, S. M. Walker, and D. S. Kemp, "Energetic characterization of short helical polyalanine peptides in water: analysis of 13co chemical shift data," *Journal of the American Chemical Society*, vol. 127, no. 48, pp. 16961–16968, 2005.

[104] G. E. Job, R. J. Kennedy, B. Heitmann, J. S. Miller, S. M. Walker, and D. S. Kemp, "Temperature- and length-dependent energetics of formation for polyalanine helices in water: assignment of wala(n,t) and temperature-dependent cd ellipticity standards," *Journal of the American Chemical Society*, vol. 128, no. 25, pp. 8227–8233, 2006.

[105] B. Zagrovic, G. Jayachandran, I. S. Millett, S. Doniach, and V. S. Pande, "How large is an -helix? studies of the radii of gyration of helical peptides by small-

angle x-ray scattering and molecular dynamics," *J. Mol. Biol.*, vol. 353, no. 2, pp. 232 – 241, 2005.

[106] A. A. Podtelezhnikov and D. L. Wild, "Exhaustive metropolis monte carlo sampling and analysis of polyalanine conformations adopted under the influence of hydrogen bonds," *Proteins: Struct., Funct., Bioinf.*, vol. 61, no. 1, pp. 94–104, 2005.

[107] F. P. Agostini, D. D. O. Soares-Pinto, M. A. Moret, C. Osthoff, and P. G. Pascutti, "Generalized simulated annealing applied to protein folding studies," *J. Comput. Chem.*, vol. 27, no. 11, pp. 1142–1155, 2006.

[108] D. Diana, B. Ziaco, G. Scarabelli, C. Pedone, G. Colombo, L. D'Andrea, and R. Fattorusso *Chem. Eur. J.*, vol. 16, pp. 5400 – 5407, 2010.

[109] E. K. Asciutto, A. V. Mikhonin, S. A. Asher, and J. D. Madura, "Computational and experimental determination of the -helix unfolding reaction coordinate," *Biochemistry*, vol. 47, no. 7, pp. 2046–2050, 2008.

[110] E. J. Sorin and V. S. Pande, "Exploring the helix-coil transition via all-atom equilibrium ensemble simulations," *Biophys. J.*, vol. 88, no. 4, pp. 2472 – 2493, 2005.

[111] A. E. Garcia and K. Y. Sanbonmatsu, "-helical stabilization by side chain shielding of backbone hydrogen bonds," *Proc. Natl. Acad. Sci. U.S.A*, vol. 99, no. 5, pp. 2782–2787, 2002.

[112] H. Nymeyer and A. E. Garcia, "Simulation of the folding equilibrium of -helical peptides: A comparison of the generalized born approximation with explicit solvent," *Proc. Natl. Acad. Sci. U.S.A*, vol. 100, no. 24, pp. 13934–13939, 2003.

[113] A. E. and Garcia, "Characterization of non-alpha helical conformations in ala peptides," *Polymer*, vol. 45, no. 2, pp. 669 – 676, 2004.

[114] C. Brooks and D. A. Case, "Simulations of peptide conformational dynamics and thermodynamics," *Chem. Rev.*, vol. 93, no. 7, pp. 2487–2502, 1993.

[115] P. R. Pandey and S. Roy, "Headgroup mediated water insertion into the dppc bilayer: A molecular dynamics study," *The Journal of Physical Chemistry B*, vol. 115, no. 12, pp. 3155–3163, 2011.

[116] C. Nick Pace and J. Martin Scholtz *Biophys. J.*, vol. 75, pp. 422 – 427, 1998.

[117] F. M. DiCapua, S. Swaminathan, and D. L. Beveridge *Journal of the American Chemical Society*, vol. 112, pp. 6768 – 6771, 1990.

[118] F. M. DiCapua, S. Swaminathan, and D. L. Beveridge *Journal of the American Chemical Society*, vol. 113, pp. 6145 – 6155, 1991.

[119] R. L. Baldwin, "Early days of protein hydrogen exchange: 19541972," *Proteins: Struct., Funct., Bioinf.*, vol. 79, no. 7, pp. 2021–2026, 2011.

[120] R. L. Baldwin, "In search of the energetic role of peptide hydrogen bonds," *J. Biol. Chem.*, vol. 278, no. 20, pp. 17581–17588, 2003.

[121] D. Van Der Spoel, E. Lindahl, B. Hess, and G. Groenhof *J. Comput. Chem.*, vol. 26, p. 1701, 2005.

[122] B. Hess, C. Kutzner, D. van der Spoel, and E. Lindahl *J. Chem. Theory Comput.*, vol. 4, pp. 435 – 447, 2008.

[123] G. A. Kaminski, R. A. Friesner, J. Tirado-Rives, and W. L. Jorgensen *The Journal of Physical Chemistry B*, vol. 105, pp. 6474 – 6487, 2001.

[124] W. L. Jorgensen, J. Chandrasekhar, J. D. Madura, R. W. Impey, and M. L. Klein *The Journal of Chemical Physics.*, vol. 79, pp. 926 – 935, 1983.

[125] M. Patra, M. Karttunen, M. T. Hyvonen, E. Falck, P. Lindqvist, and I. Vattulainen *Biophys. J.*, vol. 84(6), pp. 3636 – 3645, 2003.

[126] W. Li, M. Qin, Z. Tie, and W. Wang, "Effects of solvents on the intrinsic propensity of peptide backbone conformations," *Phys. Rev. E*, vol. 84, pp. 041933–1 – 041933–9, Oct 2011.

[127] P. Doruker and I. Bahar, "Role of water on unfolding kinetics of helical peptides studied by molecular dynamics simulations," *Biophys. J.*, vol. 72, pp. 2445 – 2456, 1997.

[128] F. Avbelj, P. Luo, and R. L. Baldwin, "Energetics of the interaction between water and the helical peptide group and its role in determining helix propensities," *Proc. Natl. Acad. Sci. U.S.A*, vol. 97, no. 20, pp. 10786–10791, 2000.

[129] R. L. and Baldwin, "Relation between peptide backbone solvation and the energetics of peptide hydrogen bonds," *Biophys. Chem.*, vol. 101-102, no. 0, pp. 203 – 210, 2002.

[130] V. A. Couch, N. Cheng, K. Nambiar, and W. Fink, "Structural characterization of -helices of implicitly solvated poly-alanine," *The Journal of Physical Chemistry B*, vol. 110, no. 7, pp. 3410–3419, 2006.

[131] S. K. Lakkaraju and W. Hwang *Phys. Rev. Lett.*, vol. 102, pp. 118102–1 – 118102–4, 2009.

[132] S. Choe and S. X. Sun *The Journal of Chemical Physics.*, vol. 122, pp. 244912–1 – 244912–9, 2005.

[133] P. L. Yeagle and R. B. Martin, "Hydrogen-bonding of the ester carbonyls in phosphatidylcholine bilayers," *Biochemical and Biophysical Research Communications*, vol. 69, no. 3, pp. 775 – 780, 1976.

[134] C. F. Schmidt, Y. Barenholz, C. Huang, and T. E. Thompson, "Phosphatidylcholine carbon-13-labeled carbonyls as a probe of bilayer structure," *Biochemistry*, vol. 16, no. 18, pp. 3948–3954, 1977.

[135] J. Pope and B. Cornell, "A pulsed {NMR} study of lipids, bound water and sodium ions in macroscopically-oriented lecithin/water lyotropic liquid crystal model membrane systems," *Chemistry and Physics of Lipids*, vol. 24, no. 1, pp. 27 – 43, 1979.

[136] J. M. Smaby, A. Hermetter, P. C. Schmid, F. Paltauf, and H. L. Brockman, "Packing of ether and ester phospholipids in monolayers. evidence for hydrogen-bonded water at the sn-1 acyl group of phosphatidylcholines," *Biochemistry*, vol. 22, no. 25, pp. 5808–5813, 1983.

[137] Z. Zhou, B. G. Sayer, D. W. Hughes, R. E. Stark, and R. M. Epand, "Studies of phospholipid hydration by high-resolution magic-angle spinning nuclear magnetic resonance," *Biophysical Journal*, vol. 76, no. 1, pp. 387 – 399, 1999.

[138] J. Fitter, R. E. Lechner, and N. A. Dencher, "Interactions of hydration water and biological membranes studied by neutron scattering," *The Journal of Physical Chemistry B*, vol. 103, no. 38, pp. 8036–8050, 1999.

[139] C. P. Sotomayor, L. F. Aguilar, F. J. Cuevas, M. K. Helms, and D. M. Jameson, "Modulation of pig kidney na+/k+-atpase activity by cholesterol: role of hydration," *Biochemistry*, vol. 39, no. 35, pp. 10928–10935, 2000.

[140] B. Poolman, J. J. Spitzer, and J. M. Wood, "Bacterial osmosensing: roles of membrane structure and electrostatics in lipidprotein and proteinprotein interactions," *Biochimica et Biophysica Acta (BBA) - Biomembranes*, vol. 1666, no. 12, pp. 88 – 104, 2004. Lipid-Protein Interactions.

[141] V. V. Volkov, D. J. Palmer, and R. Righini, "Heterogeneity of water at the phospholipid membrane interface," *The Journal of Physical Chemistry B*, vol. 111, no. 6, pp. 1377–1383, 2007.

[142] F. Zhou and K. Schulten, "Molecular dynamics study of a membrane-water interface," *The Journal of Physical Chemistry*, vol. 99, no. 7, pp. 2194–2207, 1995.

[143] Y. Takaoka, M. Pasenkiewicz-Gierula, H. Miyagawa, K. Kitamura, Y. Tamura, and A. Kusumi, "Molecular dynamics generation of nonarbitrary membrane models reveals lipid orientational correlations," *Biophysical Journal*, vol. 79, no. 6, pp. 3118 – 3138, 2000.

[144] M. Pasenkiewicz-Gierula, Y. Takaoka, H. Miyagawa, K. Kitamura, and A. Kusumi, "Charge pairing of headgroups in phosphatidylcholine membranes: A molecular dynamics simulation study," *Biophysical Journal*, vol. 76, no. 3, pp. 1228 – 1240, 1999.

[145] C. F. Lopez, S. O. Nielsen, M. L. Klein, and P. B. Moore, "Hydrogen bonding structure and dynamics of water at the dimyristoylphosphatidylcholine lipid bilayer surface from a molecular dynamics simulation," *The Journal of Physical Chemistry B*, vol. 108, no. 21, pp. 6603–6610, 2004.

[146] K. V. Damodaran and K. M. Merz, "Head group-water interactions in lipid bilayers: a comparison between dmpc- and dlpe-based lipid bilayers," *Langmuir*, vol. 9, no. 5, pp. 1179–1183, 1993.

[147] K. V. Damodaran, K. M. Merz, and B. P. Gaber, "Structure and dynamics of the dilauroylphosphatidylethanolamine lipid bilayer," *Biochemistry*, vol. 31, no. 33, pp. 7656–7664, 1992.

[148] A. A. Polyansky, P. E. Volynsky, D. E. Nolde, A. S. Arseniev, and R. G. Efremov, "Role of lipid charge in organization of water/lipid bilayer interface: insights via computer simulations," *The Journal of Physical Chemistry B*, vol. 109, no. 31, pp. 15052–15059, 2005. PMID: 16852905.

[149] A. Kukol, "Lipid models for united-atom molecular dynamics simulations of proteins," *Journal of Chemical Theory and Computation*, vol. 5, no. 3, pp. 615–626, 2009.

[150] J. F. Nagle and S. Tristram-Nagle, "Lipid bilayer structure," *Current Opinion in Structural Biology*, vol. 10, no. 4, pp. 474 – 480, 2000.

[151] N. Kuerka, S. Tristram-Nagle, and J. F. Nagle, "Closer look at structure of fully hydrated fluid phase {DPPC} bilayers," *Biophysical Journal*, vol. 90, no. 11, pp. L83 – L85, 2006.

[152] S. Chiu, M. Clark, V. Balaji, S. Subramaniam, H. Scott, and E. Jakobsson, "Incorporation of surface tension into molecular dynamics simulation of an interface: a fluid phase lipid bilayer membrane," *Biophysical Journal*, vol. 69, no. 4, pp. 1230 – 1245, 1995.

[153] I. Chandrasekhar, M. Kastenholz, R. Lins, C. Oostenbrink, L. Schuler, D. Tieleman, and W. Gunsteren, "A consistent potential energy parameter set for lipids: dipalmitoylphosphatidylcholine as a benchmark of the gromos96 45a3 force field," *European Biophysics Journal*, vol. 32, no. 1, pp. 67–77, 2003.

[154] M. Pasenkiewicz-Gierula, Y. Takaoka, H. Miyagawa, K. Kitamura, and A. Kusumi, "Hydrogen bonding of water to phosphatidylcholine in the membrane as studied by a molecular dynamics simulation: location, geometry, and lipidlipid bridging via hydrogen-bonded water," *The Journal of Physical Chemistry A*, vol. 101, no. 20, pp. 3677–3691, 1997.

[155] K. Murzyn, W. Zhao, M. Karttunen, M. Kurdziel, and T. Rg, "Dynamics of water at membrane surfaces: Effect of headgroup structure," *Biointerphases*, vol. 1, no. 3, 2006.

[156] W. Zhao, T. Rg, A. A. Gurtovenko, I. Vattulainen, and M. Karttunen, "Atomic-scale structure and electrostatics of anionic palmitoyloleoylphosphatidylglycerol lipid bilayers with na+ counterions," *Biophysical Journal*, vol. 92, no. 4, pp. 1114 – 1124, 2007.

[157] M. Sovago, E. Vartiainen, and M. Bonn, "Observation of buried water molecules in phospholipid membranes by surface sum-frequency generation spectroscopy," *The Journal of Chemical Physics*, vol. 131, no. 16, pp. –, 2009.

[158] I. Chandrasekhar, D. Bakowies, A. Glttli, P. Hnenberger, C. Pereira, and W. F. van Gunsteren, "Molecular dynamics simulation of lipid bilayers with gromos96: Application of surface tension," *Molecular Simulation*, vol. 31, no. 8, pp. 543–548, 2005.

[159] A. J. Beevers and A. Kukol, "Systematic molecular dynamics searching in a lipid bilayer: Application to the glycophorin a and oncogenic erbb-2 transmembrane domains," *Journal of Molecular Graphics and Modelling*, vol. 25, no. 2, pp. 226 – 233, 2006.

[160] X. Liu, Y. Xu, H. Li, X. Wang, H. Jiang, and F. J. Barrantes, "Mechanics of channel gating of the nicotinic acetylcholine receptor," *PLoS Comput Biol*, vol. 4, p. e19, 01 2008.

[161] J. M. Cuthbertson, P. J. Bond, and M. S. P. Sansom, "Transmembrane helix-helix interactions: comparative simulations of the glycophorin a dimer," *Biochemistry*, vol. 45, no. 48, pp. 14298–14310, 2006. PMID: 17128969.

[162] O. Bakouche, D. Gerlier, J. Letoffe, and P. Claudy, "Phase separation of miscible phospholipids by sonication of bilayer vesicles," *Biophysical Journal*, vol. 50, no. 1, pp. 1 – 4, 1986.

[163] J. J. Lpez Cascales, T. F. Otero, A. J. Fernndez Romero, and L. Camacho, "Phase transition of a dppc bilayer induced by an external surface pressure:

from bilayer to monolayer behavior. a molecular dynamics simulation study," *Langmuir*, vol. 22, no. 13, pp. 5818–5824, 2006. PMID: 16768513.

[164] K. Lum, D. Chandler, and J. D. Weeks, "Hydrophobicity at small and large length scales," *The Journal of Physical Chemistry B*, vol. 103, no. 22, pp. 4570–4577, 1999.

[165] D. Chandler, "Hydrophobicity: Two faces of water," *Nature*, vol. 417, p. 491, 2002.

[166] R. Godawat, S. N. Jamadagni, and S. Garde, "Characterizing hydrophobicity of interfaces by using cavity formation, solute binding, and water correlations," *Proceedings of the National Academy of Sciences*, vol. 106, no. 36, pp. 15119–15124, 2009.

[167] S. Krishnamurty, M. Stefanov, T. Mineva, S. Bgu, J. M. Devoisselle, A. Goursot, R. Zhu, and D. R. Salahub, "Density functional theory-based conformational analysis of a phospholipid molecule (dimyristoyl phosphatidylcholine)," *The Journal of Physical Chemistry B*, vol. 112, no. 42, pp. 13433–13442, 2008.

[168] H. Hauser, I. Pascher, R. Pearson, and S. Sundell, "Preferred conformation and molecular packing of phosphatidylethanolamine and phosphatidylcholine," *Biochimica et Biophysica Acta (BBA) - Reviews on Biomembranes*, vol. 650, no. 1, pp. 21 – 51, 1981.

[169] H. Hauser, I. Pascher, and S. Sundell, "Preferred conformation and dynamics of the glycerol backbone in phospholipids. an nmr and x-ray single-crystal analysis," *Biochemistry*, vol. 27, no. 26, pp. 9166–9174, 1988.

[170] M. Hong, K. Schmidt-Rohr, and H. Zimmermann, "Conformational constraints on the headgroup and sn-2 chain of bilayer dmpc from nmr dipolar couplings," *Biochemistry*, vol. 35, no. 25, pp. 8335–8341, 1996.

[171] K. S. Bruzik and J. S. Harwood, "Conformational study of phospholipids in crystalline state and hydrated bilayers by 13c and 31p cp-mas nmr," *Journal of the American Chemical Society*, vol. 119, no. 28, pp. 6629–6637, 1997.

[172] F. Aussenac, M. Laguerre, J.-M. Schmitter, and E. J. Dufourc, "Detailed structure and dynamics of bicelle phospholipids using selectively deuterated and perdeuterated labels. 2h nmr and molecular mechanics study," *Langmuir*, vol. 19, no. 25, pp. 10468–10479, 2003.

[173] S. Leekumjorn and A. K. Sum, "Molecular simulation study of structural and dynamic properties of mixed dppc/dppe bilayers," *Biophysical Journal*, vol. 90, no. 11, pp. 3951 – 3965, 2006.

[174] W. Hbner and A. Blume, "Interactions at the lipidwater interface," *Chemistry and Physics of Lipids*, vol. 96, no. 12, pp. 99 – 123, 1998.

[175] A. Debnath, B. Mukherjee, K. G. Ayappa, P. K. Maiti, and S.-T. Lin, "Entropy and dynamics of water in hydration layers of a bilayer," *The Journal of Chemical Physics*, vol. 133, no. 17, pp. –, 2010.

[176] C. Park, J. Yoon, and E. L. Thomas, "Enabling nanotechnology with self assembled block copolymer patterns," *Polymer*, vol. 44, no. 22, pp. 6725 – 6760, 2003.

[177] K. J. M. Bishop, C. E. Wilmer, S. Soh, and B. A. Grzybowski, "Nanoscale forces and their uses in self-assembly," *Small*, vol. 5, no. 14, pp. 1600–1630, 2009.

[178] Y. Wang, B. Li, Y. Zhou, Z. Lu, and D. Yan, "Dissipative particle dynamics simulation study on the mechanisms of self-assembly of large multimolecular micelles from amphiphilic dendritic multiarm copolymers," *Soft Matter*, vol. 9, pp. 3293–3304, 2013.

[179] C. Cai, Y. Li, J. Lin, L. Wang, S. Lin, X.-S. Wang, and T. Jiang, "Simulation-assisted self-assembly of multicomponent polymers into hierarchical assemblies with varied morphologies," *Angewandte Chemie International Edition*, vol. 52, no. 30, pp. 7732–7736, 2013.

[180] O.-S. Lee, S. I. Stupp, and G. C. Schatz, "Atomistic molecular dynamics simulations of peptide amphiphile self-assembly into cylindrical nanofibers," *Journal of the American Chemical Society*, vol. 133, no. 10, pp. 3677–3683, 2011.

[181] T. Yu, O.-S. Lee, and G. C. Schatz, "Steered molecular dynamics studies of the potential of mean force for peptide amphiphile self-assembly into cylindrical nanofibers," *The Journal of Physical Chemistry A*, vol. 117, no. 32, pp. 7453–7460, 2013.

[182] W. Shinoda, D. E. Discher, M. L. Klein, and S. M. Loverde, "Probing the structure of pegylated-lipid assemblies by coarse-grained molecular dynamics," *Soft Matter*, vol. 9, pp. 11549–11556, 2013.

[183] G. Fiorin, M. Klein, R. DeVane, and W. Shinoda, "Computer simulation of self-assembling macromolecules," in *Hierarchical Macromolecular Structures: 60*

Years after the Staudinger Nobel Prize II (V. Percec, ed.), vol. 262 of *Advances in Polymer Science*, pp. 93–107, Springer International Publishing, 2013.

[184] J. Zhang, K. Saerens, I. Bogaert, and W. Soetaert, "Vegetable oil enhances sophorolipid production by rhodotorula bogoriensis," *Biotechnology Letters*, vol. 33, no. 12, pp. 2417–2423, 2011.

[185] P. A. J. Gorin, J. F. T. Spencer, and A. P. Tulloch, "Hydroxy fatty acid glycosides of sophorose from torulopsis magnoliae," *Canadian Journal of Chemistry*, vol. 39, no. 4, pp. 846–855, 1961.

[186] I. N. V. Bogaert, J. Zhang, and W. Soetaert, "Microbial synthesis of sophorolipids," *Process Biochemistry*, vol. 46, no. 4, pp. 821 – 833, 2011.

[187] I. Van Bogaert, K. Saerens, C. De Muynck, D. Develter, W. Soetaert, and E. Vandamme, "Microbial production and application of sophorolipids," *Applied Microbiology and Biotechnology*, vol. 76, no. 1, pp. 23–34, 2007.

[188] A. M. Shete, G. Wadhawa, I. M. Banat, and B. A. Chopade *J. Sci. Ind. Res.*, vol. 65, pp. 91–115, 2006.

[189] S. L. Fu, S. R. Wallner, W. B. Bowne, M. D. Hagler, M. E. Zenilman, R. Gross, and M. H. Bluth, "Sophorolipids and their derivatives are lethal against human pancreatic cancer cells," *Journal of Surgical Research*, vol. 148, no. 1, pp. 77 – 82, 2008.

[190] S. Zhou, C. Xu, J. Wang, W. Gao, R. Akhverdiyeva, V. Shah, and R. Gross, "Supramolecular assemblies of a naturally derived sophorolipid," *Langmuir*, vol. 20, no. 19, pp. 7926–7932, 2004. PMID: 15350054.

[191] N. Baccile, N. Nassif, L. Malfatti, I. N. A. Van Bogaert, W. Soetaert, G. Pehau-Arnaudet, and F. Babonneau, "Sophorolipids: a yeast-derived glycolipid as greener structure directing agents for self-assembled nanomaterials," *Green Chem.*, vol. 12, pp. 1564–1567, 2010.

[192] P. Dhasaiyan, P. R. Pandey, N. Visaveliya, S. Roy, and B. Prasad, "Vesicle structures from bola-amphiphilic bio-surfactants: Experimental and md simulation studies on the effect of unsaturation on the sophorolipid self-assemblies," *Chemistry A European Journal*, vol. in press, 2014.

[193] M. J. Frisch, G. W. Trucks, H. B. Schlegel, G. E. Scuseria, M. A. Robb, J. R. Cheeseman, G. Scalmani, V. Barone, B. Mennucci, G. A. Petersson, H. Nakatsuji, M. Caricato, X. Li, H. P. Hratchian, A. F. Izmaylov, J. Bloino, G. Zheng, J. L. Sonnenberg, M. Hada, M. Ehara, K. Toyota, R. Fukuda, J. Hasegawa, M. Ishida, T. Nakajima, Y. Honda, O. Kitao, H. Nakai, T. Vreven, J. A. Montgomery, Jr., J. E. Peralta, F. Ogliaro, M. Bearpark, J. J. Heyd, E. Brothers, K. N. Kudin, V. N. Staroverov, R. Kobayashi, J. Normand, K. Raghavachari, A. Rendell, J. C. Burant, S. S. Iyengar, J. Tomasi, M. Cossi, N. Rega, J. M. Millam, M. Klene, J. E. Knox, J. B. Cross, V. Bakken, C. Adamo, J. Jaramillo, R. Gomperts, R. E. Stratmann, O. Yazyev, A. J. Austin, R. Cammi, C. Pomelli, J. W. Ochterski, R. L. Martin, K. Morokuma, V. G. Zakrzewski, G. A. Voth, P. Salvador, J. J. Dannenberg, S. Dapprich, A. D. Daniels, . Farkas, J. B. Foresman, J. V. Ortiz, J. Cioslowski, and D. J. Fox, "Gaussian 09 Revision D.01." Gaussian Inc. Wallingford CT 2009.

Publications

1. **P. R. Pandey** and S. Roy, Head group mediated water insertion in DPPC bilayer, The Journal of Physical Chemistry B, 2011, 115, 31553163.

2. **P. R. Pandey** and S. Roy, Early stages of unwinding of zwitterionic alpha-helical homopolymeric peptides, Chemical Physics Letters, 2011, 514, 330335.

3. **P. R. Pandey** and S. Roy, Distinctions in early stage unwinding mechanisms of zwitterionic, capped, and neutral forms of different -Helical homopolymeric peptides, The Journal of Physical Chemistry B, 2012, 116, 47314740.

4. S. Pahari, C.K. Choudhury, **P. R. Pandey**, M. More, A. Venkatnathan, and S. Roy, Molecular Dynamics Simulation of Phosphoric Acid Doped Monomer of Polybenzimidazole: A Potential Component of Polymer Electrolyte Membrane of fuel cell, The Journal of Physical Chemistry B, 2012, 116 (24), 7357-7366.

5. **P. R. Pandey** and S. Roy, Is it Possible to Change Wettability of Hydrophilic Surface by Changing its Roughness?, The Journal of Physical Chemistry Letters, 2013, 4(21), 3692-3697.

6. P. Dhasaiyan, **P. R. Pandey**, N. Visaveliya, S. Roy, and B. L. V. Prasad, Vesicle structures from bola-amphiphilic bio-surfactants: Experimental and MD simulation studies on the effect of unsaturation on the sophorolipid self-assemblies, Chemistry - A European Journal, 2014, 20, 6246-6250.

7. **P. R. Pandey** and S. Roy, Model Atomistic Protrusions Favouring Ordering and Retention of Water, Physical Chemistry Chemical Physics, 2014, 16, 15856-15865.

Erratum